PHD

A study on the optimisation of electrochemical impedance spectroscopy biosensors

Formisano, Nello

Award date:
2016

Awarding institution:
University of Bath

A study on the optimisation of electrochemical impedance spectroscopy biosensors

Nello Formisano

A thesis submitted for the degree of Doctor of Philosophy

University of Bath

Department of Electronic and Electrical Engineering

October 2015

Table of contents

Acknowledgements

I would like to thank all of my family, friends and colleagues. I am very grateful to Prof. Janice Limson and Prof. Sabine Flitsch to have allowed me to work in their research groups at Rhodes University (South Africa) and at The University of Manchester, respectively. Special thanks are given to Maisem Laabei, Mel Heeran, James Tyson and Siva Sivaraya for the great collaboration experiences. I would also like to thank my co-supervisor Prof. John Taylor for his precious guidance. I must also acknowledge my examiners for reading this thesis and for the valuable indication that I'm going to receive.

I can say that all the people that I have met in the last 3 years have really contributed to my personal and professional growth in some way. In particular, I feel very lucky to have met:

My supervisor, Dr. Pedro Estrela, not only for allowing me to undertake this fundamental journey but also for guiding me with his invaluable wisdom and trying to keep always my motivation high.

My friends Nikhil Bhalla and Pawan Jolly for the never-ending inspiration and for supporting me in the good and bad moments, literally pushing me when I needed some help. There are not enough words to say how grateful I am towards them.

My best British friends Ed Regan, Phillip Robinson ad Jon Storey, for the great time spent together as well as for the precious proofreading, and Marco Ponziani for not making me miss Italy as well as for the trips and the Carbonaras we had together.

All the friends and colleagues: Shrey Pathak, Anna Miodek, Zhugen Yang, Pavel Zhourasky, Ben Metcalfe, Jules Hammond, Caleb Wong, Federico Brivio, Susana Liébana Girona and Vibha Tamboli and all the other members in the 2E 2.24, for both experiments and the good moments shared together.

I also need to thank all of my football teammates for the kicks and the good time.

A very special thank goes to Mirella Di Lorenzo that simply has always been there throughout these years. I could not imagine my staying in Bath without her.

My last and most special gratitude is for my family that I felt even closer than ever despite the distance. I thank all of them for their endless love.

List of Publications

- **Formisano, N.**, Tyson, J. A., Jolly, Miodek, A., Pascu, S. I., & Estrela, P. (2015). Label-free impedimetric sensor for detection of PC-3 cells using BBN (7-13) as a recognition element. In preparation.
- **Formisano, N.**, Bhalla, N., Heeran, M., Martinez, J. R., Sarkar, A., Laabei, M., Jolly, P., Bowen, C. R., Taylor, J. T., Flitsch, S. L., & Estrela, P. (2015). Inexpensive and fast pathogenic bacteria screening using field-effect transistors. Submitted.
- Hammond, J. L., **Formisano, N.**, Estrela, P., Carrara, S., & Tkac, J. (2015). Electrochemical biosensors and nanobiosensors. *Essays in Biochemistry*, Portland Press, in press.
- Bhalla, N., Jolly, P., **Formisano, N.**, & Estrela, P. (2015). Introduction to biosensors. *Essays in Biochemistry*, Portland Press, in press..
- **Formisano, N.**, Jolly, P., Bhalla, N., Cromhout, M., Flanagan, S. P., Fogel, R., Limson, J. L., & Estrela, P. (2015). Optimisation of an electrochemical impedance spectroscopy aptasensor by exploiting quartz crystal microbalance with dissipation signals. *Sensors and Actuators B: Chemical*, 220, 369-375.
- Bhalla, N., **Formisano, N.**, Miodek, A., Jain, A., Di Lorenzo, M., Pula, G., & Estrela, P. (2015). Plasmonic ruler on field-effect devices for kinase drug discovery applications. *Biosensors and Bioelectronics*, 71, 121-128.
- **Formisano, N.**, Bhalla, N., Wong, L. C., Di Lorenzo, M., Pula, G., & Estrela, P. (2015). Multimodal electrochemical and nanoplasmonic biosensors using ferrocene crowned nanoparticles for kinase drug discovery applications. *Electrochemistry Communications*, 57, 70-73.
- Jolly, P., **Formisano, N.**, Tkáč, J., Kasák, P., Frost, C. G., & Estrela, P. (2015). Label-free impedimetric aptasensor with antifouling surface chemistry: A prostate specific antigen case study. *Sensors and Actuators B: Chemical*, 209, 306-312.
- Jolly, P., **Formisano, N.**, & Estrela, P. (2015). DNA aptamer-based detection of prostate cancer. *Chemical Papers*, 69(1), 77-89.
- Bettazzi, F., Hamid-Asl, E., Esposito, C. L., Quintavalle, C., **Formisano, N.**, Laschi, S., Catuogno, S., Iaboni, M., Marrazza, G., Mascini, M., Cerchia, L., De Franciscis, V., Condorelli, G., & Palchetti, I. (2013). Electrochemical

detection of miRNA-222 by use of a magnetic bead-based bioassay. *Analytical and Bioanalytical Chemistry*, 405(2-3), 1025-1034.

Abstract

Electrochemical impedance spectroscopy (EIS) has been one of the most intensively studied electrochemical techniques for biosensing in recent decades. However, despite its great potential, real applications of EIS sensors still remain not as widely spread as other techniques because there are many factors that govern impedimetric signals. In particular, features such as the probe coverage density on the sensor surface, as well as the target size, charge and conformation, can assume significant importance.

The aim of this study was to analyse both the limitations and the potential solutions for maximizing the EIS signals in certain possible systems which are characterised by having different types of target to detect. In order to reproduce different conditions, four types of molecular targets have been taken in consideration. These provided example systems where the approach for the development of an EIS sensor varied considerably. In the first system the importance of the surface conditions of an aptasensor for prostate specific antigen (PSA) using Faradaic processes was reported. It was demonstrated that the effect of the target binding combined with the relative surface charge modification can diminish the EIS signals. In the second system, a strategy for improving the sensitivity and selectivity of the assay for drug discovery applications was demonstrated. This was obtained by adopting ferrocene-crowned gold nanoparticles that specifically bind to the molecular targets and induced a transition from non-Faradaic to Faradaic processes. In the last two example systems, particular attention has also been given to non-Faradaic processes which are the least exploited in EIS systems although the technique can be simpler to implement compared to Faradaic EIS. Moreover, with non-Faradaic processes more effective results can be achieved under some specific conditions, such as exploiting the size and charge of molecular targets.

On such premises, the current work wants to serve as a reference for overcoming the limitations met in several EIS systems and hopefully contribute as a support for enhancing the fields of applications of EIS sensors.

Nomenclature

A	Area
c	Concentration
C	Capacitance
d	Distance
D	(a) Dissipation
	(b) Diffusion constant
D_O	Diffusion coefficient
e	Electron charge
E	Electrode potential
$E^{0'}$	Formal potential
E_K	Kinetic energy
f	Frequency
F	Faraday constant
f_0	Fundamental frequency of the quartz crystal
i	Current
I	Ionic strength
J	Flux
k	Rate constant
k_B	Boltzmann constant
K_d	Dissociation constant
L	Inductance
n	Number of electrons transferred
N_A	Avogadro number
O	Oxidised form of redox coupe (O,R)
Q	Charge
R	Reduced form of redox coupe (O,R)
R_{ct}	Charge transfer resistance
S	Scan rate
t	Time
T	Temperature
V	Voltage
v_x	Hydrodynamic velocity
x	Direction
Y_o	Magnitude of the CPE admittance at $\omega = 1\ rad/s$
z	Ion valence

Z	Impedance
α	Anodic transfer coefficient
Γ	Amount of species adsorbed
ε_0	Permittivity of free space
ε_r	Relative permittivity
η	Overpotential
θ	Phase
κ	Debye inverse length
λ	Conductance
λ_D	Debye length
μ_q	Shear modulus of the quartz crystal
ρ	Charge density
ρ_q	Density of the quartz crystal
σ	Surface charge
Φ	Electrostatic potential
ω	Angular frequency

List of abbreviations

ADP	Adenosine diphosphate
AR	Androgen receptor
ATP	Adenosine triphosphate
ATP-S	Adenosine thiotriphosphate
AUT	11-amino-1-undecanethiol hydrochloride
BBN	Bombesin
CFU	Colony-forming unit
CMOS	Complementary metal–oxide–semiconductor
CPE	Constant phase element
CV	Cyclic voltammetry
DNA	Deoxyribonucleic acid
DPV	Differential pulse voltammetry
EDC	1-ethyl-3-(3-dimethylaminopropyl)carbodiimide
EDL	Electrochemical double layer
EIS	Electrochemical impedance spectroscopy
ELISA	Enzyme-linked immunosorbent assay
Fc	6-(ferrocenyl)hexanethiol
FRA	Frequency-response analyser

GNP	Gold nanoparticle
GRP	Gastrin-releasing peptide
HSA	Human serum albumin
IDE	Interdigitated electrodes
IHP	Inner Helmholtz plane
LOD	Limit of detection
LOQ	Limit of quantitation
LSPR	Localised surface plasmon resonance
MALDI-ToF	Matrix-assisted laser desorption ionisation-time of flight
MBP	Myelin basic protein
MCH	6-mercapto-1-hexanol
MOSFET	Metal–oxide–semiconductor field-effect transistor
MS	Mass spectrometry
MUA	Mercaptoundecanoic acid
Sulfo-NHS	Sulfo-N-Hydroxysulphosuccinimide
OCP	Open circuit potential
OHP	Outer Helmholtz plane
PBS	Phosphate buffer saline
PEG	Polyethylene-glycol
PKC- α	Protein kinase C alpha
PSA	Prostate specific antigen
QCM	Quartz crystal microbalance
QCM-D	Quartz crystal microbalance with dissipation mode
SAM	Self assembled monolayer
SEM	Scanning electron microscopy
SPR	Surface plasmon resonance
UPEC	Uropathogenic *Escherichia coli*

Chapter 1. Introduction

1.1 Motivation

Despite its potential and although it has been intensively studied for many decades, electrochemical impedance spectroscopy (EIS) still struggles to be affirmed as a credible technique for real biological sensing applications. Researchers have often been discouraged not only by the need to have certain knowledge about the electrochemical double layer and some electrical modelling skills but also the need to control the factors that can affect EIS signals: namely the self-assembled monolayer (SAM) formation, the probe distribution onto the sensor surface and the molecular conformation of the biofilms. Moreover, the type and the properties of a molecular target which require detection can greatly affect the choice of strategies to adopt in an EIS sensor, in order to gather a detectable signal. In particular, the size and charge of the ligand can assume significant importance. As a result, the surface immobilisation strategies and the choice of exploiting Faradaic or non-Faradaic processes can be crucial factors in EIS detection. In this context, the present work presents the analysis of several possible systems that can be explored with EIS, investigation and therefore studies of some of the limitations that can affect EIS signals and proposes possible solutions, or strategies, to improve the molecular detections.

Four different molecular targets have been taken in consideration in order to provide example systems where the approach for the development of an EIS sensor can vary

considerably. Apart from the optimisation of the EIS sensors proposed, some systems provided important findings and considerations. In one of the example systems, DNA aptamers were employed for prostate specific antigen (PSA) detection. Using quartz crystal microbalance with dissipation mode (QCM-D) it was found that the conditions that maximize the target binding could not guarantee the optimal conditions for the greatest EIS signal. In fact, the effect that the analyte binding has on the net charge modification of the sensor surface must be taken into account. In applications where oligonucleotides are employed, the negative charge of the nucleic acid could be enhanced in case of a complementary DNA hybridisation or, conversely, partially neutralised by the molecular targets as for the development of our aptasensor.

In other EIS systems, particular importance was given to non-Faradaic processes where either the size of the molecular target or its considerable charge (or the combined effect of both) could be exploited. Non-Faradaic processes rely on the changes of the electrochemical double layer upon molecular detections, the redistribution of the solvent molecules and of the ions at the interface between the sensor surface and the measurement solution. Although the study of such phenomena can be not particularly easy to face, if the systems are modelled with an appropriate equivalent electric circuit, important parameters such as the double layer capacitance of the system can be obtained - which is a powerful tool for measuring molecular interactions. Therefore, although non-Faradaic experiments are less exploited compared to Faradaic processes, they could provide greater impact for possible real applications as redox molecules are not needed in the electrochemical cell for the measurements.

Therefore, this dissertation can hopefully serve as a reference for a better understanding of several types of systems and in particular can provide useful research and indications as to how specific properties of some molecular targets can be exploited effectively to enhance the EIS detection in biological applications.

1.2 Outline

EIS is a powerful investigative tool that allows the modelling of a biological system with an equivalent electric circuit and, eventually, to extrapolate parameters such as the charge transfer resistance and the double layer capacitance from it. In order to pave the way on how to apply such properties to biological systems, a theoretical introduction of the phenomena occurring at the solid-liquid interface between the sensor and solution in the electrochemical cell where the experiments take place, must be introduced. This is discussed in Chapter 2 where both the description of the electrochemical double layer and the techniques used for the studies of this work are presented.

Although the basis of EIS is introduced in Chapter 2, in Chapter 3 more detailed aspects about this technique are given. Here, the distinction between Faradaic and non-Faradaic processes, as well as how an EIS experiment is prepared, are explained. In addition, references to other studies based on EIS can be found, with particular focus on the aspects that lead me to examine in depth several types of systems which will be introduced in the following chapters.

The outcome from each type of system will be summarised and discussed at the end of the relative chapter. The first example system is described in Chapter 4 where an aptasensor for PSA detection is reported. Here, aspects relevant to the probe surface immobilisation are faced. The optimisation of the probe immobilisation in this study is particularly important, as is also the case for other DNA sensors, in order to enhance the amount of target binding. However, DNA aptamer based sensors are characterised by slightly different mechanisms with respect to sensors based on DNA-DNA interactions. In fact, the interaction between the DNA aptamer and the target, which in our case is a protein, causes conformational changes of the probe as well as modifications of the net charge upon the recognition event. Therefore, the mass loading and the screening of the charge contribute in an opposite fashion towards the generation of the EIS signal in Faradaic experiments.

In Chapter 5, EIS is used for protein phosphorylation detection as a means for drug discovery applications. Phosphorylation of proteins is an important post-

transcriptional modification that can be responsible of several diseases. In this chapter furthermore, a strategy based on the use of signal probes for improving the sensitivity and the selectivity of the test is introduced. In particular, this approach is based on the transition from non-Faradaic to Faradaic processes using ferrocene-modified gold nanoparticles that allow the generation of Faradaic currents in a system that originally lacked redox molecules. The small sensitivity that was obtained by conventional EIS, where signal enhancers were not used, are significantly improved by carrying out thio-phosphorylation and adopting ferrocene-crowned gold nanoparticles that specifically attach to the thio-phosphorylated proteins. The detection could successfully be confirmed by performing differential pulse voltammetry on the same array of electrodes.

Bacteria and cancer cells detection (a preliminary study) have ultimately been investigated and reported in Chapter 6 to show how non-Faradaic processes could exploit the size and the charge of the target molecules. It is also shown that, in order to improve the sensitivity of the detection, special precaution must be taken in terms of ionic strength of the measurement and SAM employed. EIS detection of bacteria was also supported by measuring potential changes by MOSFETs.

Chapter 2. Principles and methods

2.1 Electrochemical biosensors

An electrochemical biosensor is a device capable of converting chemical information, arising from the binding of a biological molecule, into a quantifiable electrical signal. In such a process, when biological molecules interact specifically with a suitable bioreceptor, a change in physical or chemical parameters occurs, which can be detected and converted into an quantifiable signal by means of a transducer system (Cammann, 1977; Lowe *et al.*, 1990; Thévenot *et al.*, 2001).

An electrochemical biosensor usually involves an electrode surface that has been functionalised with a molecular recognition element. Binding of an analyte to this element results in an electrical change in either current transfer (amperometric), voltage (potentiometric and field effect devices), impedance (impedimetric) or conductivity (conductometric) across the electrode, which can be quantified (Rinken, 2013).

The general architecture defining an electrochemical biosensing system is presented in Figure 2.1 and involves:

- An interface architecture able to bind the analyte (usually by functionalising an electrode surface with a bioreceptor molecule) and also able to convert the recognition event into a detectable signal for further processing.
- A transducer system which gathers the signal and converts it into an electrical one ready for analysis.

- A signal processing system that can amplify and elaborate the electrical signal in order to generate an output which is correlated to the amount of analyte detected.

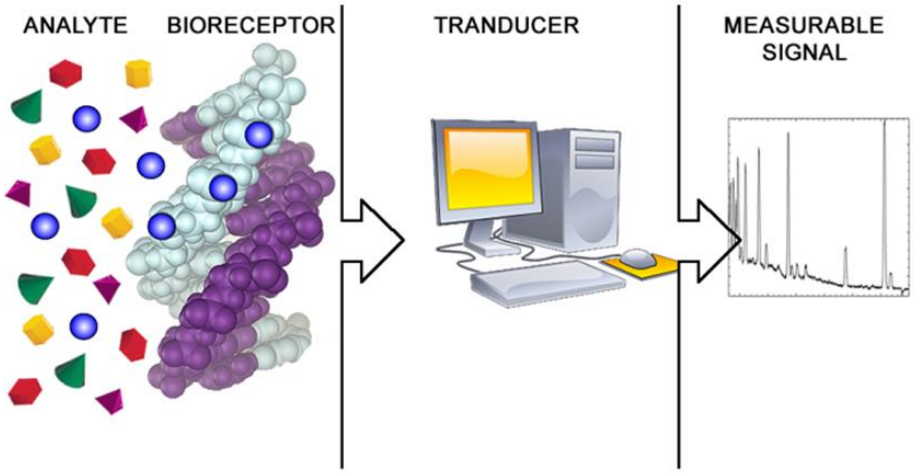

Figure 2.1 General biosensor architecture. The analyte to detect is recognised by a specific bioreceptor at the sensor interface. A transducer element converts the binding event into a quantifiable electrical signal for further elaboration. The signal is finally displayed. Reproduced from Rinken, (2013).

In order to specifically detect molecules of interest, the electrode surface is generally modified with a suitable bio-recognition layer that exploits a physical or chemical process. Extensive research has been focussed on investigating electrode modification techniques (Kasemo, 2002). Research is often directed towards finding the most suitable recognition element and optimizing the architecture interface in order to enhance the binding efficiency as well as the signal produced (Putzbach and Ronkainen, 2013).

2.2 Electrochemistry

2.2.1 Electrochemical principles

Electrochemistry allows us to correlate chemical reactions to electrical currents for the qualitative and quantitative determination of species in a solution or at the surface of an electrode. Electrochemical investigations usually take place at an electrode-electrolyte interface in an electrochemical cell. The electrolyte solution in which the

chemical reactions take place contains charged species such as ions that guarantee electron transfer at the interface with the electrodes used for the investigation. Typical measurements in electrochemistry are either potentiometric or potentiostatic. Potentiometric experiments involve the measurement of a voltage potential rather than a measurement of current. It is also referred to as static or zero-current measurement.

The simplest configuration for an electrochemical cell comprises of two electrodes for the electrochemical measurements which are the *working electrode* and the *counter electrode* (or *auxiliary electrode*). The working electrode is the actual biosensor interface where biological probes are placed to specifically bind target molecules. In such a configuration, the potential changes of the working electrode upon the analyte detection are measured with respect to the reference potential provided by the counter electrode, which completes the electrical circuit. In order to obtain an accurate measurement of the potential at the working electrode, the reference potential at the counter electrode must be kept ideally fixed. In electrochemical experiments often the detection or the behaviour of an analyte is monitored by perturbing the system i.e. taking the system away from its equilibrium state. This can be obtained by applying a potential or a current to the working electrode. If we consider a potentiostatic experiment, in order to apply a potential, a reference electrode that has a constant potential is required. At the same time, the response of the system upon the perturbation has to be measured by recording the flow of current across the working electrode and another electrode. In a two-electrode system both the perturbation and the current response would be applied and measured using the same pair of electrodes. However, when the current flows between the working and the counter electrodes, the potential of the latter can change, thereby it cannot be used as a reference any more. To overcome this limitation, the control of the potential and of the current can be split by using a further electrode in the electrochemical cell. A three-electrode set up is thus preferred where a *reference electrode* is introduced. In this case, voltage potentials are set between the working and reference electrodes and current flow is monitored through the counter electrode (see Figure 2.2 for a schematic diagram of a typical three-electrode set-up). Therefore, the reference electrode, which provides a reference

potential for the application of a perturbation, is not involved in the exchange of current between the working and the counter electrodes.

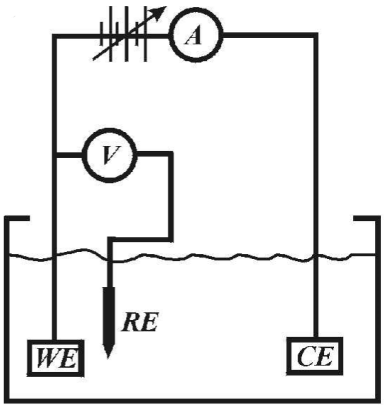

Figure 2.2 Electrochemical cell in a three-electrode set up. WE, RE and CE represent the working electrode, reference electrode and counter electrode, respectively. Voltage potentials are applied across the working and reference electrode and the electrical current passes through the working and counter electrode

The pair reference electrode/working electrodes constitute a system where the so called *half-cell potential* of the working electrode can be determined by accurately controlling the half-cell potential of the reference electrode. In electrochemical experiments the reference electrode is characterised by a certain known and stable voltage potential (its derivation can be found in the next section) and is ideally non-polarizable, namely the charge transfer should encounter ideally zero resistance to the flow of current. The accurate control over the half-cell potential of the reference electrode can be achieved by fabricating the reference electrode with saturated or buffered concentrations of compounds whose interaction generates well-known electrochemical reactions. A notable example is the standard hydrogen electrode (SHE) with all components at unity activity, which consists of a platinum wire dipped in an acidic solution where pure hydrogen gas is also bubbled through at the pressure of 1 bar (Figure 2.3).

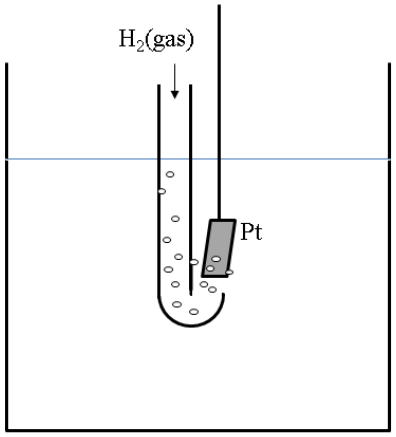

Figure 2.3 Standard hydrogen electrode (SHE)

The reaction at the platinum electrode is: $2H^+(aq) + 2e^- \rightarrow H_2(g)$. At 25 °C this reaction generates an absolute potential of 4.44 V. The SHE is also used as a means of comparison for other reference electrode systems. For instance, one of the most common reference electrodes used for electrochemical measurements is the silver-silver chloride electrode (Ag/AgCl/KCl, where the slashes indicate the separation between the media), which has a potential of 0.197 V against SHE.

The counter electrode typically consists of an inert metal, such as platinum, that does not involve any reaction but is responsible for carrying electrons whilst the reference electrode holds a known potential independently from the solution properties.

Electrochemical measurements in such a set up can be performed by means of an instrument called potentiostat that applies the desired potentials between the working electrode and reference electrode and is used to record the relative currents.

Before going more deeply into a typical set-up for electrochemical measurements, some accurate descriptions about what happens at the electrode interface must be given. The electrode-solution interface (Figure 2.4) is the place where chemical and electrical gradients can generate electrochemical interactions (Thévenot *et al.*, 2001). When two dissimilar phases come into contact, such as a solid electrode facing an aqueous solution interface, a re-distribution of the interfacial charges occurs. The net or excess charge (in the solid interface) and orientated solvent dipoles (in the

electrolyte solution) generate an interfacial electric field known as the '*electrified interface'*. The transport of current is governed by the diffusion laws in the ionic phase and by metal-conduction laws in the electrode phase. In the case of ideally polarizable electrodes, there is no transfer of charges across the interface. The following relation for ideally polarizable electrodes holds valid:

$$R_{ct} \rightarrow \infty \tag{2.1}$$

where R_{CT} is the charge transfer resistance. As a consequence, the current flowing in an ideally polarizable electrode is zero, therefore, the electrified interface can analytically be better described as a capacitor where the ions can approach or be repulsed from the interfacial region by means of potential changes.

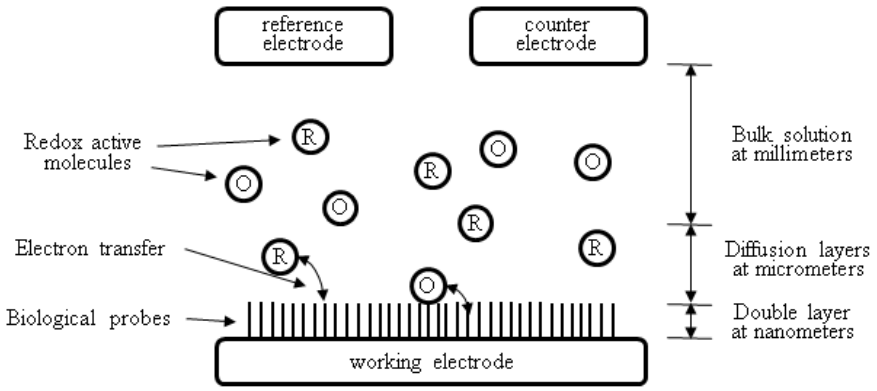

Figure 2.4 Illustration of an electrochemical cell where electrical and chemical gradients generate movements of species to and from the sensing surface (the electron and mass transfer processes will be explained in more detail in the following sections).

At the electrode interface, a condition of equilibrium in terms of charge must be satisfied. The excess of charge σ_M on the metal layer of the electrode, which is confined to a 1 Å thick layer, is compensated by the charge present in the solution (σ_S):

$$\sigma_M = -\sigma_S \tag{2.2}$$

The spatial distribution of charges at the electrified interface is called the electrochemical double layer (EDL). Multiple models of the EDL have been generated with the aim of accurately describing the reaction kinetics at the electrode interface.

In 1850, Helmholtz modelled the EDL with a parallel-plate capacitor where both the metal and the electrolyte have the same space charge distribution. In this model the excess of charges are distributed at the surface of the two interfaces. The opposite signs of the charges formed a double layer (Figure 2.5), which can be modelled as a capacitor. Such a capacitor has capacitance dependent on the thickness of the double layer, *d*, given by the molecular dimensions of the ions in the liquid phase in contact with the solid.

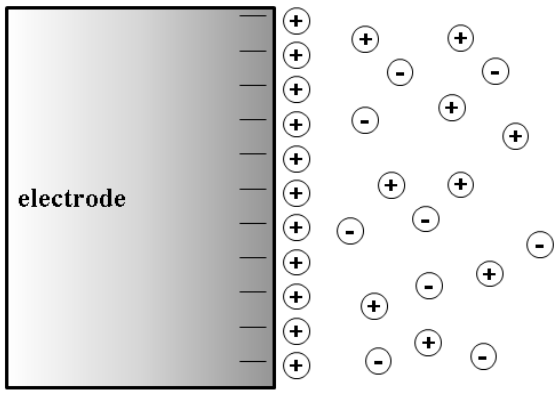

Figure 2.5 Electrochemical double layer model as described by Helmholtz.

The capacitance of the double layer described by Helmholtz can be derived as for a parallel-plate capacitor:

$$C_d = \frac{\varepsilon_r \varepsilon_0 A}{d} \tag{2.3}$$

where ε_r is the relative permittivity of the solvent, ε_0 is the permittivity of free space and A is the area of interest of the double layer. However, according to this model, the capacitance of the double layer would be constant. In practice the electrolyte composition in the thin Helmholtz region is considerably different from the composition in the bulk solution. Likewise, the term ε_r varies. A further limitation of the Helmholtz description is that the ions are modelled as point charges and their

distribution is regular at the interfaces and not dependent on the concentration or the electrode potential. In practice, the thermal motion creates an uneven distribution of ions at the electrolyte interfacial region. To overcome these limitations a 3-D model of the EDL was necessary.

The Gouy-Chapman model takes into account the random thermal motion as well as the electrostatically driven ionic concentration gradient between the interfacial region and bulk solution. In the Gouy-Chapman model the concept of a *diffuse layer* is introduced, where the excess charge density finds its maximum at the electrolyte interfacial region and decreases exponentially towards the bulk solution (Figure 2.6). Moreover, the diffuse layer becomes more compact as the ionic concentration is increased and as electrostatic forces decrease. Since the conductivity of the electrolyte solution is significantly lower than that of the metal, the diffuse layer at the liquid interface is around 1-10 nm longer than the layer of excess charge present at the metal interface (about 1 Å). A measure of the diffuse layer thickness is given by the *Debye length,* λ_D (11).

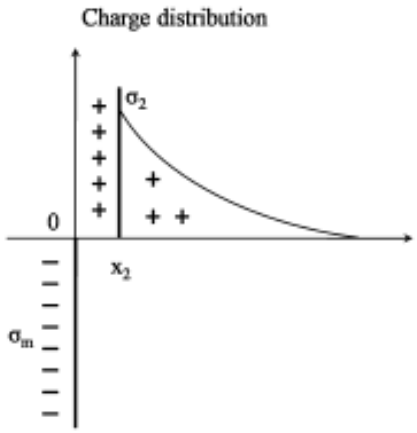

Figure 2.6 Space charge distribution in the Gouy-Chapman model of the electrochemical double. The charge distribution decreases exponentially within the diffuse layer (at a distance $x > x_2$ from the electrode surface). Reproduced from Bard and Faulkner (2001).

However, in the Gouy-Chapman model ions are considered as point charges. In practice, the solvated ions can only approach the metal surface to a distance equal to its solvated radius. A new model was proposed by Stern (1924) who combined the

features of Helmholtz and Gouy-Chapman models in order to describe the EDL with a more realistic behaviour (Figure 2.7).

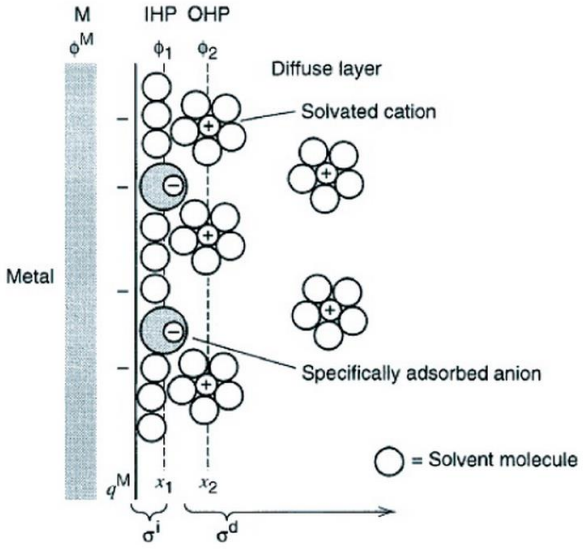

Figure 2.7 Stern model of the electrochemical double layer. Reproduced from Bard and Faulkner (2001).

In Stern's model, the region immediately next to the electrode produces a high electric field and presents a low relative permittivity ($\varepsilon_r \cong 6$) with a row of firmly held counter ions. This layer, also called the *inner layer*, consists of solvent molecules and specifically adsorbed ions. The region between the metal surface and the centres of the specifically adsorbed ions is known as the inner Helmholtz plane (IHP). Beyond this region there is an 'ionic cloud' where the ordering electrostatic forces and disordering thermal motions balance each other. Within the 'ionic cloud' the relative permittivity increases quickly with distance. Similarly, the electrical potential varies from the electrode surface to the bulk solution: within the OHP it decreases quasi-linearly and exponentially decreases within the diffuse layer - until the bulk of the solution when the electrical potential ideally reaches a value of 'zero' (Figure 2.8).

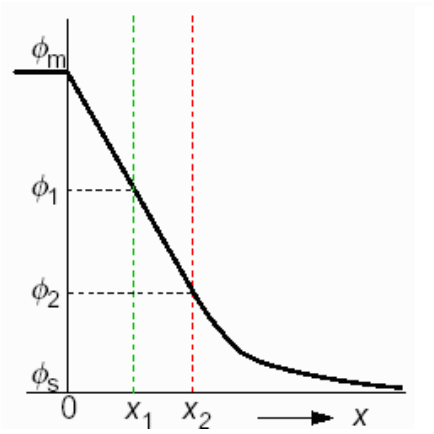

Figure 2.8 Electrical potential distribution in the normal direction to the electrode surface

The solvated ions beyond the IHP can approach the electrode surface only if they are within the so called outer Helmholtz plane (OHP). The OHP is given by the spatial distance between the electrode surface and the plane of centres of the solvated ions. Beyond the OHP there is the diffuse layer where the ions interact with the electrode surface only by means of electrostatic forces. When entering the IHP, the ions give away part of their solvation shell to specifically bind onto the electrode surface by chemical bonding. In the Stern model, the EDL can be represented by a series of capacitances: the first capacitance represents the region within the OHP which does not depend on the potential (Helmholtz capacitance) whereas the second capacitance represents the diffuse layer and depends on the potential:

$$\frac{1}{C_{EDL}} = \frac{1}{C_H} + \frac{1}{C_D} \tag{2.4}$$

where C_{EDL}, C_H, C_D are, respectively, the capacitance of the electrochemical double layer, the capacitance of the compact layer (within the OHP) and the capacitance of the diffuse layer. In a series of capacitances, the larger can be neglected if it is much bigger than the others, C_{EDL} will be mostly due to the diffuse layer capacitance in cases where the ion concentration of the solution is low.

In order to calculate the potential distribution in the EDL region and thus the capacitance of the EDL, one can use the Poisson equation which relates the charge density ρ to the electrostatic potential Φ:

$$\nabla^2 \Phi = -\frac{\rho}{\varepsilon_0 \varepsilon_r} \tag{2.5}$$

where ρ is given by:

$$\rho = \sum_j z_j e c_j \tag{2.6}$$

and z_j is the ion valence of species *j*, e is the fundamental charge and c_j is the concentration of the ionic species *j*. From the Boltzmann equation of statistical mechanics, the concentration c_j is given by:

$$c_j = c_j^b \exp\left(-\frac{z_j e \Phi(r)}{k_B T}\right) \tag{2.7}$$

where c_j^b refers to the bulk concentrations of the species *j*, k_B is the Boltzmann constant, *T* the temperature and $\Phi(r)$ the potential at a distance *r* from the electrode surface. By substitution, we can write the Poisson-Boltzmann equation (note that the operator LaPlacian, ∇^2, depends on the geometry of the system):

$$\nabla^2 \Phi = -\frac{1}{\varepsilon_0 \varepsilon_r} \sum_j z_j c_j^b \exp\left(-\frac{z_j e \Phi(r)}{k_B T}\right) \tag{2.8}$$

which, considering a system with a planar surface (*i.e.* $\nabla^2 \Phi \cong \kappa^2 \Phi$ is valid, where κ the inverse Debye length is introduced later on), for solutions where only one anionic and one cationic species are present (a *z*, *z* electrolyte) and assuming that the potentials at the surface of the electrode are not too large (Debye-Huckel approximation, where $ze\Phi \ll k_B T$), can be rewritten as:

$$\nabla^2 \Phi \cong -\frac{ezc^b}{\varepsilon_0 \varepsilon_r}\left(\exp\left(-\frac{ze\Phi}{k_B T}\right) - \exp\left(\frac{ze\Phi}{k_B T}\right)\right) =$$

$$= \frac{2ezc^b}{\varepsilon_0 \varepsilon_r} \sinh\left(\frac{ze\Phi}{k_B T}\right) \cong \frac{2ezc^b}{\varepsilon_0 \varepsilon_r} \frac{ze\Phi}{k_B T} \tag{2.9}$$

Grouping the terms together, it leads to the identity:

$$\frac{2(ze)^2 c^b}{\varepsilon_0 \varepsilon_r k_B T} \Phi = \kappa^2 \Phi \tag{2.10}$$

Therefore, the Debye inverse length κ and the surface charge density in the diffuse layer σ_D can be found:

$$\kappa = \left(\frac{2(ze)^2 c^b}{\varepsilon_0 \varepsilon_r k_B T}\right)^{\frac{1}{2}} = \lambda_D^{-1} \tag{2.11}$$

$$\sigma_D = -\varepsilon_0 \varepsilon_r \kappa \Phi_0 \tag{2.12}$$

where Φ_0 is the potential at the electrode interface. As σ_D and Φ_0 have opposite signs, this means that negative ions will be attracted in case of a positive Φ_0 and vice versa. It's important to remark that (2.11) and (2.12) are valid for a *z-z* electrolyte and for small potential applied to the metal surface.

If we want to consider a system with multivalent ions of concentration c_j and valence z_j, the ionic strength *I*, can be introduced:

$$I = \frac{1}{2}\sum_j c_j z_j^2 \tag{2.13}$$

(2.11) then becomes:

$$\kappa = \left(\frac{2N_A e^2 I}{\varepsilon_0 \varepsilon_r k_B T}\right)^{\frac{1}{2}} \tag{2.14}$$

where N_A is the Avogadro number.

Not assuming that small potentials are applied to the metal surface, we can use:

$$\sigma_D = -\frac{4zec^b}{\kappa}\sinh\left(\frac{ze\Phi}{2k_B T}\right) \tag{2.15}$$

and (2.11) in:

$$C_D = -\frac{d\sigma_D}{d\Phi_0} \tag{2.16}$$

We can develop the expression of the differential capacitance of the diffuse layer C_D:

$$C_D = \frac{2(ze)^2 c^b}{\kappa k_B T}\frac{d}{d\Phi_0}\left(\sinh\left(\frac{ze\Phi_0}{2k_B T}\right)\right) = \frac{2(ze)^2 c^b}{\kappa k_B T}\cosh\left(\frac{ze\Phi_0}{2k_B T}\right) =$$

$$= \varepsilon_0 \varepsilon_r \kappa \cosh\left(\frac{ze\Phi_0}{2k_B T}\right) \tag{2.17}$$

From which we can see that C_D is not a constant but depends on the potential. From (2.4), if we consider the OHP at distance x_2 from the electrode surface, we obtain:

$$\frac{1}{C_{EDL}} = \frac{1}{C_H} + \frac{1}{C_D} = \frac{x_2}{\varepsilon_0 \varepsilon_r} + \left(\varepsilon_0 \varepsilon_r \kappa \cosh\left(\frac{ze\Phi_0}{2k_B T}\right)\right)^{-1} \quad (2.18)$$

2.2.2 Reactions at the electrode interface

Electroactive species that undergo reduction and oxidation (redox) processes at the electrode interface are responsible of generating the so-called Faradaic currents. Faradaic currents involve transfer of charges across the electrified interface upon an electrochemical reaction. Non-Faradaic processes, instead, are not directly associated with electrochemical reactions but generate *background* currents deriving from movement of electroactive species, reorientation of solvent dipoles, adsorption and desorption events happening at the electrode-electrolyte interface. Non Faradaic currents can be measured by the amount of electric charges used at the electrode interface in order to balance the charge given by the ions at the electrolyte interfacial region. For this reason, non-Faradaic currents are also called capacitive currents as the phenomenon resembles the dynamics of a capacitor. In an electrochemical experiment both Faradaic and non-Faradaic processes can take place. However, in order to properly quantify the chemical reactions by means of Faradaic current measurements, this must be larger enough than the non-Faradaic currents (Faradaic current $\gg$ background current).

In this section we analyse the Faradaic processes and the kinetics of the reactions involved. In an electrochemical cell, the redox processes occur simultaneously and the total difference of these components gives the net current flowing into the cell. The process is accompanied by a transfer of electrons:

$$O + ne^- \Leftrightarrow R \quad (2.19)$$

where O and R are the oxidised and reduced forms of the electroactive species. The main aim of electrochemical experiments is to correlate the concentration of species in solution to the electrons transfer generated by redox reactions as in (2.19). The concentrations c'_O and c'_R of the oxidised and reduced species at the electrode surface and the potential of the electrode are correlated by the Nernst equation:

$$E = E^{0'} + \frac{RT}{nF}\ln\frac{c'_O}{c'_R} \tag{2.20}$$

where $E^{0'}$ is the formal potential of the redox species, R is the molar gas constant, n is the number of electrons transferred in the process and F is the Faraday constant. For potentials lower than $E^{0'}$, the process of reduction of the oxidised species is kinetically favourable. However, (2.20) is not of much help in experimental conditions as the concentrations at the surface are unknown. On the other hand, in conditions of equilibrium, namely where the concentration of the species in the bulk solution, c_O^b and c_R^b, are equal to the concentrations on the surface, (2.20) can be rewritten as:

$$E = E^{0'} + \frac{RT}{nF}\ln\frac{c_O^b}{c_R^b} \tag{2.21}$$

which shows the dependence of the electrode potential to the concentration of the species in the solution. The reduction and oxidation currents involved in the reaction follow Faraday's law (the currents are directly proportional to the amount of reduced or oxidised species) and are respectively:

$$i_R = -nFAk_R c'_O \tag{2.22}$$

$$i_O = nFAk_O c'_R \tag{2.23}$$

where k_R and k_O are the rate constants for the reduction and oxidation electron transfer, respectively and are exponentially related to the activation energy required for that specific reaction to occur. At the equilibrium, the values of current deriving from the oxidation and reduction processes are identical and equal to the value of exchange current i_0 which is the balanced Faradaic current at equilibrium when the net current is zero.

Assuming $c_O^b = c_R^b = c$, the exchange current is:

$$i_0 = nFAk^0 c \tag{2.24}$$

where k^0 is the standard rate constant for the reaction and A the electrode area. This current tells us how easy it is for electron transfer to happen in a certain system. For any reaction happening in an electrochemical cell, the current is both proportional to

the concentration of the species and to the potential applied. If one applies a small overpotential η (with respect to the equilibrium potential), the charge transfer resistance can be derived and is equal to:

$$R_{ct} = \frac{\eta}{i} = \frac{RT}{Fi_0} \tag{2.25}$$

If the concentration of the electroactive species in solution do not differ significantly from their value in proximity of the electrode surface and in case the movement of the species as well as the current generated are of small entity, mass transfer effects can be neglected. In such cases, the current is given by the Butler-Volmer equation:

$$i = i_0 \left[\exp\left(-\frac{\alpha nF\eta}{RT}\right) - \exp\left(\frac{(1-\alpha)nF\eta}{RT}\right)\right] \tag{2.26}$$

where α is the anodic transfer coefficient. For overpotentials $\eta > 118\,\frac{\mathrm{mV}}{n}$ (considering a value of $T = 298\,K$), the second exponential term can be neglected and (2.26) becomes:

$$i = i_0 \exp\left(-\frac{\alpha nF\eta}{RT}\right) \tag{2.27}$$

At equilibrium condition (net current equal to zero and surface concentrations equal to bulk concentrations) the Butler-Volmer equation becomes:

$$\frac{c_O^b}{c_R^b} = \exp\left(-\frac{nF}{RT}\left(E - E^{0'}\right)\right) \tag{2.28}$$

which is also an exponential form of the Nernst equation.

2.3 Electrochemical detection techniques

Electrochemical sensors can be categorised according to the type of measurement performed (Thévenot *et al.*, 2001): amperometric, potentiometric, conductometric, impedimetric, ion charge or field effect. In the next section an overview of the different techniques will be given, with particular focus on the techniques reported in this study and moreover with particular attention to electrochemical impedance spectroscopy.

2.3.1 Amperometric biosensors

In a cell containing electroactive species, amperometric measurements are carried out recording reduction/oxidation currents between the working electrode and the counter electrode when controlled potentials are applied at the working electrode with respect to the reference electrode (Thévenot *et al.*, 2001; Grieshaber *et al.*, 2008). Faradaic currents can be either directly generated by the redox activity of the analyte at the electrode interface or by the activity of an electroactive mediator which interacts with the biomolecule under investigation (Luppa *et al.*, 2001). Often the second approach is preferred. Amperometry is considered to be one of the most sensitive techniques in electrochemistry (Thévenot *et al.*, 2001, Luppa *et al.*, 2001).

Some texts report on a classification based on the nature of the potential applied for the electrochemical measurement: if the potential is kept constant between the reference and working electrodes, the technique is referred to as amperometry while if the potential is given with a specific wave shape and amplitude, the technique is referred to as voltammetry. Therefore, several types of voltammetry can be carried out by using diverse applied voltages profiles. However, voltammetry can be considered as an amperometric technique since both are based on the same working principles.

In voltammetry the experiments consist of recording the current upon applying an appropriate potential wave. The currents generated are the result of three different contributions. They arise from the capacitive currents, adsorption effects and Faradaic currents, respectively. The first two contributions give the so-called background current and do not give analytical information about the electrochemical reaction of interest. Currents of no analytical interest might also come from the oxidation and reduction of impurities present in solution. Faradaic currents of the analytical species, instead, provide qualitative and quantitative information about the processes happening in the electrochemical cell.

The capacitive currents generate at the electrochemical double layer as a result of the accumulation of charges at the interfacial region. Capacitive currents are sensitive to the variation of potential applied at the electrode surface following the law:

$$i_c = C_{EDL} \frac{dv}{dt} \tag{2.29}$$

where C_{EDL} is the capacitance of the electrochemical double layer and v is the potential applied to the electrode surface. This means that the faster the potential changes, the higher the capacitive current will be. In case of a linear potential applied at the electrode (as for the case of cyclic voltammetry), the derivative in (2.29) can be simplified to a differential and the term $\frac{dv}{dt}$ can be substituted by the scan rate (expressed in $V\ s^{-1}$).

Currents due to adsorption effects also depend on the rapidity with which the potential steps are applied and can be evaluated as follows (Bard and Faulkner, 1980):

$$i_a = \frac{(nF)^2 A\Gamma_a}{4RT}\frac{dv}{dt} \tag{2.30}$$

where Γ_a is the amount of species adsorbed per unit area on the electrode surface. The presence and the shape of the adsorption peaks provide information about the contamination and quality of the electrode.

In voltammetry, Faradaic currents have a linear proportionality with the concentration of the electroactive species in solution which makes the technique very interesting and useful for many applications. Both mass transfer and charge transfer affect the rate of the electrochemical reactions happening in the cell. The signal is gathered at the working electrode surface by means of two phenomena: mass transfer and electron transfer. The redox species can reach the electrode surface from the bulk solution by means of mass transportation. Once the redox species approach the electrode surface within the nanometre scale, electron transfer occurs at the electrode interface, inducing measurable potentials or currents (Figure 2.9). The kinetic rate of the reaction is proportional to the current measured and, based on the nature of the analyte and the analytical conditions, is controlled by the slowest process between the mass transport and the electron transport. For example, in the case where the mass transport of the species to/from the bulk is slower than the electron transfer, the current flow is limited by the mass transfer.

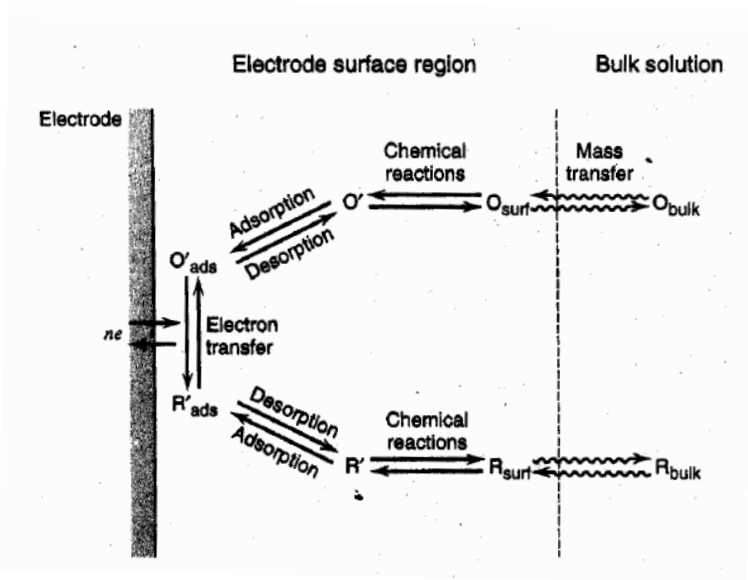

Figure 2.9 Mass and charge transfer processes occurring at an electrode interface. Mass transportation brings species from the bulk solution close to the electrode surface. Once the species are in the nanometric range distance they can exchange charges with the electrode surface. Reproduced from Bard and Faulkner (2001)

The mass transportation can be due to three phenomena: diffusion (where the transportation is driven by gradients of concentration), migration (where charged molecules are transferred by means of an electric field) and convection (induced by thermic motions). The Nernst-Planck equation describes the flux, J, of material that moves in an x direction, by joining the different contributions of the mass transportation:

$$J(x,t) = -D\frac{\partial c(x,t)}{\partial x} - \frac{zF}{RT}Dc(x,t)\frac{\partial \Phi(x,t)}{\partial x} + c(x,t)v_x(x,t) \qquad (2.31)$$

where D is the diffusion constant ($cm^2 s^{-1}$), c is the concentration (M), F is the Faraday constant (C), and v_x is the hydrodynamic velocity ($cm\, s^{-1}$). The measure unit of J is $mol\ cm^{-2} s^{-1}$.

Most of the electrochemical experiments are carried out in still environment with the concentration of salt added in solution much greater (e.g. 100 times higher) than the concentration of the electroactive species. These characteristics make the migration and convection effects negligible and mass transfer is predominantly driven by

diffusion, which in the Nernst-Planck equation is represented by the first term. The current can be thus derived:

$$i = -nFAJ = nFAD\frac{\partial c(x,t)}{\partial x} \tag{2.32}$$

which shows the dependence of the current from the variation of concentration at the electrode interface. Since for reversible systems the current can also be derived from the Nernst-Planck equation when the thermodynamic laws are respected, this means that the charge transfer must be fast enough to guarantee conditions of equilibrium at every moment.

Diffusion is mathematically described by Fick's second law:

$$\frac{\partial c(x,t)}{\partial t} = D\frac{\partial^2 c(x,t)}{\partial x^2} \tag{2.33}$$

valid for parallel planes in the direction of the diffusion. If one applies an overpotential large enough to cause a reactant *O* to reduce to *R* at the electrode interface, the concentration of *O* at the surface becomes instantaneously zero and the current generated can be related to the time of the reaction. Cottrell was the first to derive the amount of current generated through the values of diffusion and bulk concentration of the reactant:

$$i = \frac{nFAD_O^{\frac{1}{2}}c_O^b}{(\pi t)^{\frac{1}{2}}} \tag{2.34}$$

where D_O is the diffusion coefficient of the reactant.

2.3.1.1 Chronoamperometry and chronocoulometry

Chronoamperometry and chronocoulometry refer to the measurement of current or charge, respectively, upon applying sudden potential steps at a reversible system that causes the reduction or oxidation of an electroactive species present in solution (Steel *et al.*, 1998). Before the potential step is applied, the working electrode is kept at a fixed potential that does not cause any electrochemical reaction but simply creates a

double layer at the interface. The current or charge is plotted versus $t^{\frac{1}{2}}$ and the dependence follows the integrated Cottrell equation (Su *et al.*, 2004):

$$Q = 2nFAc_O^b \left(\frac{D_O t}{\pi}\right)^{\frac{1}{2}} + nFA\Gamma_O + Q_{DL} \tag{2.35}$$

Considering the use of a reactant *O*, Γ_O is its adsorbed coverage and Q_{DL} is the charge of the double layer. Chronocoulometry is for example used for DNA quantification i.e. for determining a DNA surface density coverage, usually in terms of molecules/cm^2. Electroactive markers such as $Ru(NH_3)_6^{3+}$ are used to counterbalance the monovalent ions of DNA which are negatively charged. Applying a sudden potential step the reduction of $Ru(NH_3)_6^{3+}$ takes place and a diffusion-limited current originates which can be derived from (2.35). The first term of the integrated Cottrell equation refers to the diffusion of the redox species from the solution, whereas the second and third terms take into account the reduction of the electro-active species *O* confined at the electrode surface and the capacitive charge of the double layer, respectively. Since the charge is, by definition, obtained integrating the current over the time, chronoamperometry and chronocoulometry are equivalent to each other. The total current is given by the sum of Faradaic and non-Faradaic contributions. In condition of low concentrations of electrochemical species in solution, the Faradaic currents are much smaller than the capacitive (non-Faradaic) currents. This affects the limit of detection as the analytical contribution comes from the Faradaic current. However, high electrochemical reactant concentrations raise the Faradaic current. Moreover, as a capacitive current decreases as $exp\left(-\frac{t}{RC}\right)$, low solution resistance makes the capacitive current decay much faster than Faradaic current. For this reason, the current is sampled after a certain delay time t_D that ensures a minor contribution of the capacitive current. In particular, the mean current measured, i_S, is given by the integration over a small window of time $t_{D+x} - t_D$ divided by the time window:

$$i_S = \frac{1}{t_{D+x} - t_D} \int_{t_D}^{t_{D+x}} i\,(t) dt \tag{2.36}$$

This principle of *current sampling* is important as it is also used in other voltammetric techniques in order to reduce the capacitive contribution to the measurements.

In case of DNA coverage quantification, measurements are taken twice: in presence and absence of $Ru(NH_3)_6^{3+}$ and they both are characterised by having approximatively equal double layer charge Q_{DL} terms. By using the double-step measurement, the difference of the intercepts at $t = 0$ of the two least square fits is used to derive the term $nFA\Gamma_O$ (Figure 2.10). This can give the estimation of the DNA surface density from the formula:

$$\Gamma_{DNA} = \Gamma_O N_A \left(\frac{z_R}{n_p}\right) \tag{2.37}$$

where Γ_{DNA} is the DNA surface density, N_A is the Avogadro's number, z_R is the charge of $Ru(NH_3)_6^{3+}$ and n_p is the number of phosphate groups on the DNA.

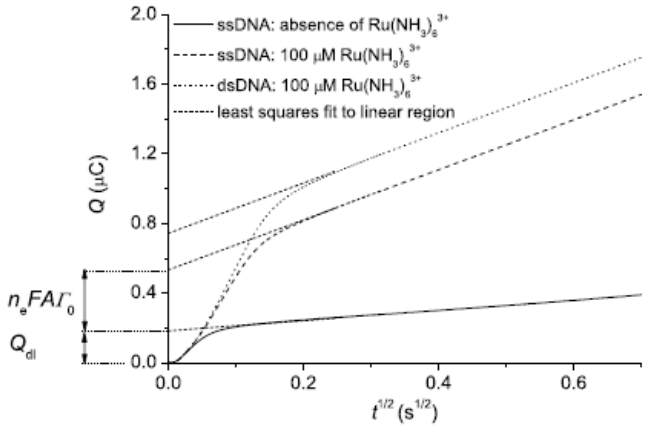

Figure 2.10 Example of Chronocoulometry plot obtained using $Ru(NH_3)_6^{3+}$ before and after complementary strand hybridised on a single strand DNA.

2.3.1.2 Cyclic voltammetry

Cyclic voltammetry (CV) is mostly used as a characterisation technique to investigate the kinetics of a reaction as well as to obtain qualitative information about electrochemical systems. The potential at the working electrode is swept back and forward linearly with time *vs.* the reference electrode and the current flowing is simultaneously recorded. If in the electrochemical cell are present molecules that can be oxidised or reduced in that specific potential window, the applied potential causes

reduction and oxidation currents (according to the direction of the scan) (Figure 2.11). Such molecules that can undergo redox reactions are called redox probes.

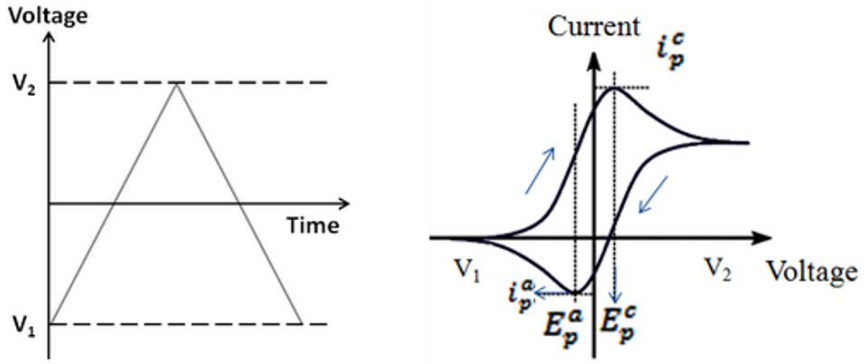

Figure 2.11 CV of the fully reversible redox reaction $Fe(CN)_6^{3-} + e^- \leftrightarrow Fe(CN)_6^{4-}$

Once the potential reaches an extent for which the working electrode goes from a condition of equilibrium to a condition where redox reactions are favourable, a sudden increase of current is recorded since the reduction and the oxidation of the molecular probes cause exchange of electrons with the electrode surface. After an initial peak, the generated Faradaic current decreases asymptotically with the diffusion layer (Figure 2.11). For a fully reversible system where only a redox species is present, the anodic or cathodic peak current can be described by the Randles-Sevčik law:

$$i_p = 0.4436An^{\frac{3}{2}}\left(\frac{F^3DS}{RT}\right)^{\frac{1}{2}}c \tag{2.38}$$

where D is the diffusion coefficient of the species reduced or oxidised, S is the scan rate and c is the bulk concentration of the electroactive species. The formula is valid for both reduction or oxidation reduction peaks and shows a direct proportionality of i_p with the concentration of the electroactive species and a square root proportionality with the scan rate. Therefore, if i_p *vs.* $S^{\frac{1}{2}}$ curve is linear, one can say that the reaction is controlled by diffusion.

As for voltammetric techniques, the Faradaic current is directly proportional to the electroactive species in solution. The scan rate must allow the necessary time for redox

reactions to occur. It also affects the measurement but with a square root law. However, since the capacitive current increases linearly with the scan rate, a reasonable low scan rate is usually employed for CV measurements (typically $<$ 100 mV s^{-1}).

CV can be used also for studies of reversibility of the electrochemical systems. In a fully reversible reaction the anodic peak current is equal to the cathodic peak current and the separation between the two peaks is given by:

$$\Delta E_p = E_{pa} - E_{pc} = \frac{59}{n} \text{ mV} \quad (2.39)$$

valid at 25 ºC, where E_{pa} and E_{pc} are the anodic and the cathodic peak potential, respectively. Drifting away from the reversible conditions, the separation between the peaks will increase as well as the value of anodic and cathodic currents will be different.

2.3.1.3 Differential pulse voltammetry

In order to achieve better sensitivity and to significantly reduce the capacitive currents, differential pulse voltammetry (DPV) was developed as an electrochemical tool (Bard and Faulkner, 1980). In DPV, the applied potential is given by superimposing a series of equally high pulses to a staircase waveform (Figure 2.12).

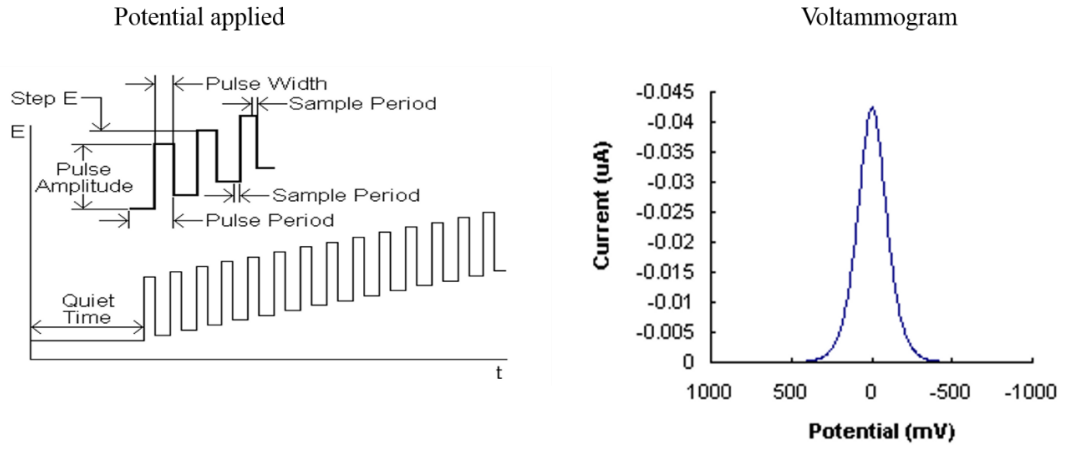

Figure 2.12 Example of voltage potential applied in DPV experiments (left side) and of voltammogram obtained where the differential current is plotted vs. the applied potential.

The current is then measured right before and at the end of the pulse. Since the capacitive current decreases exponentially with time and the Faradaic current decreases as $t^{-\frac{1}{2}}$, DPV is more immune to the background currents resulting in a more sensitive technique as compared to CV. Moreover, the pulses are of small amplitude (*ca.* 5 mV) so to further reduce the contribution of the capacitive currents. A typical voltammogram for DPV relates the differential currents versus the applied potential (Figure 2.12). The concentration of the analyte in solution is directly proportional to the height of the peak current.

2.3.2 Electrochemical Impedance Spectroscopy

By applying an a.c. rather than a d.c. signal to an electrochemical system, a richer series of information can be obtained for the system characterisation. Based on such principle, electrochemical impedance spectroscopy (EIS) can provide valuable qualitative and quantitative information about electrochemical reactions and the electrical double layer at the sensor interface (Janata, 2002; Orazem and Tribollet, 2011; Barsoukov and MacDonald, 2005; Bertt, 1993; Lasia, 2002).

In EIS the system is stimulated by applying a sinusoidal a.c. potential of small amplitude (typically 5-10 mV) that guarantees the electrochemical cell, which is a non-linear system, to work in a pseudo-steady state. The impedance signal is the alternative impedance obtained from dividing the applied potential by the current response and can also be derived from (2.25). In case of biosensing applications, the detection of an analyte by means of a sensing probe alters the electrochemical properties of the system and a change in impedance can be recorded (Scholz, 2009). In fact, information about electrochemical properties such as diffusion, ion transportation, electron transfer and modification of the double layer are included in the frequency-domain current response of the system. Although the impedance changes depend on many factors, EIS can give a deep insight and a fuller understanding of the electrochemical behaviour of the system at the sensor interfacial region.

A generic electrochemical cell can contain a number of ions in solution as well as electroactive species that produce an internal static field at the sensor surface. An analysis of the system using the small-potential signals would be complicated when such space-charge is present (MacDonald, 1992). For this reason, in EIS, it is important to create a condition of zero-charge at the working electrode interface. The condition of zero-charge is obtained by applying an external d.c. static potential at the working electrode versus the reference electrode.

It is important at this point to distinguish two main types of investigation that can be made with EIS. Using redox markers, Faradaic processes can be observed and the behaviour of the cell is more strictly related to the Faradaic currents. In such cases particular importance is given to the charge transfer resistance. For non-Faradaic processes, instead, redox markers are not exploited. The solution resistance and the charge redistribution of the ions in solution play a more important role in defining the impedance of the system. Therefore, the changes in the double layer capacitance and, sometimes, the phase shift associated with it, assume an important significance for the analysis of non-Faradaic processes.

When the extent of the internal static potential is known or defined quite well, such as in presence of redox couples in solution, the system can be analysed by applying a small a.c. signal superimposed to the formal d.c. potential of the redox couple. The d.c. signal ensures that the electrode is not polarised by the internal static field, while the small amplitude of the a.c. signal will ensure a pseudo-linear response (only changes in amplitude and phase are generated) for systems, such as electrochemical cells, that are not linear (Figure 2.13).

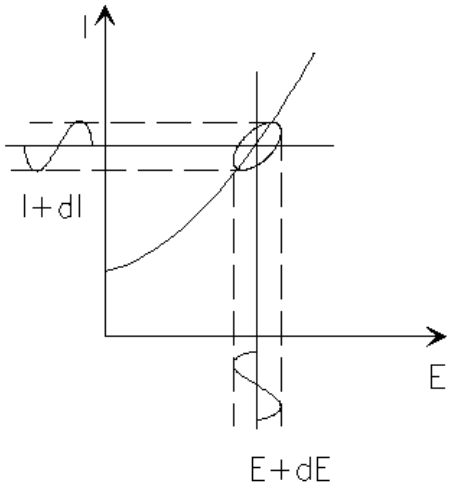

Figure 2.13 System quasi-linear response upon applying small imput signals.

Supposing the a.c. applied potential is of the type:

$$v(t) = V_p \sin(\omega t) \tag{2.40}$$

where $\omega = 2\pi f$ is the angular velocity, the current response will have the following form:

$$i(t) = I_p \sin(\omega t - \theta) \tag{2.41}$$

where θ is the phase shift due to the system response. The complex notation can be used to obtain, in an easier way, the impedance from (2.40) and (2.41):

$$Z = \frac{v(t)}{i(t)} = \frac{V_p exp(j\omega t)}{I_p exp(j\omega t - j\theta)} = |Z| exp(j\theta) \tag{2.42}$$

where $|Z| = \frac{V_p}{I_p}$ and $j \equiv (-1)^{\frac{1}{2}}$. Using the Euler relationships:

$$\sin t = \frac{e^{jt} - e^{-jt}}{2j} \tag{2.43}$$

$$\cos t = \frac{e^{jt} + e^{-jt}}{2} \tag{2.44}$$

$$e^{jt} = \cos t + j \sin t \tag{2.45}$$

(2.42) can be rewritten in terms of trigonometric functions:

$$Z = |Z|exp(j\theta) = |Z|(\cos\theta + j\sin\theta) = Z' + jZ'' \quad (2.46)$$

where Z' and Z'' are the real and imaginary part of the impedance, respectively. From (2.46) the complex impedance can be plotted in a complex plane as shown in Figure 2.14:

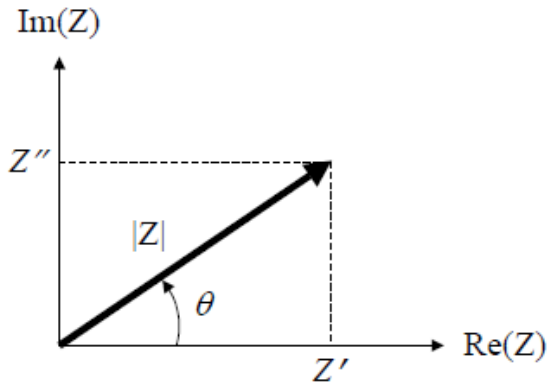

Figure 2.14 Impedance displayed in the complex plane. Reproduced from Barsoukov (2005).

The modulus of the impedance as well as the phase can thus also be derived from:

$$|Z| = \left(Z'^2 + Z''^2\right)^{\frac{1}{2}} \quad (2.47)$$

$$\theta = \tan^{-1}\frac{Z''}{Z'} \quad (2.48)$$

Since the response of a real system is frequency dependent, an EIS experiment probes the electrochemical cell in a range of frequencies, usually between 0.1 Hz to 100 kHz for biosensing applications. Such analysis is carried out by means of a frequency-response analyser (FRA) potentiostat. The ultimate goal of an EIS study is to fully characterize the frequency response of the system and be able to select, possibly, one single frequency for the implementation of a practical biosensor.

The real and imaginary impedance variation versus the frequency can be graphically analysed in the complex plane diagram (Figure 2.17). Other typical representations of the impedance data are the Bode diagrams where the modulus and phase of the impedance are plotted as a function of the frequency. The analysis of the Bode

diagrams can be particularly effective to extrapolate information at very low or very high frequencies.

The power of EIS lies on the possibility of modelling the electrochemical cell with electric components, thus, with an equivalent circuit. An equivalent circuit provides an electrical model of the electrode/electrolyte interface. It is by means of least square minimisation fitting that one can obtain the values of the electrical components associated with the electrochemical circuit. Building a model which makes use of common and well known electric elements allows us to explain the physical-chemical properties of the sensor interface. In a typical electrical circuit, the impedance is given by a combination of resistive, capacitive and inductive contributions. However, the first two components are dominant in electrochemical systems. The impedance of a purely resistive circuit is characterised by having a current response in phase with the potential applied, i.e. $\theta = 0$. For an inductance L and a capacitance C instead the current response has +90º and -90º, respectively. Inductive and capacitive responses can be mathematically described with the following equations:

$$i_C(t) = C\frac{dv(t)}{dt} \tag{2.49}$$

$$v_L(t) = L\frac{di(t)}{dt} \tag{2.50}$$

(2.49) and (2.50) can be transformed as follows for use in the complex domain:

$$I_C = j\omega CV \tag{2.51}$$

$$V_L = j\omega LI \tag{2.52}$$

from which:

$$Z_C = \frac{V}{I_C} = \frac{1}{j\omega C} = -j\frac{1}{\omega C} \tag{2.53}$$

$$Z_L = \frac{V}{I_L} = j\omega L \tag{2.54}$$

For many electrochemical systems, the most common employed equivalent circuit is the Randles equivalent circuit (Figure 2.15). In the Randles equivalent circuit R_s describes the solution resistance, R_{ct} is the charge transfer resistance and C_{DL} the

double layer capacitance. Modelling the electrochemical system with the Randles equivalent circuit can help in understanding the theory behind the phenomena occurring in the cell when some techniques are used for investigation. As shown in Figure 2.15, the total current, i, is given by the sum of the faradaic component i_F and the capacitive component i_C.

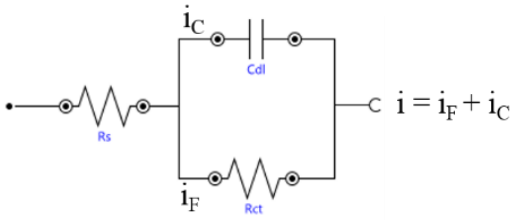

Figure 2.15 Randles equivalent circuit.

However, the capacitor in the Randles equivalent circuit does not fully describe the real behaviour of the electrochemical cells. Although still contradictory in literature (Bisquert *et al.*, 1998; Oraazem and Tribollet, 2008; Orazem and Tribollet, 2006), several studies (Brug *et al.*, 1984; Hirschorn *et al.*, 2010) have shown that the distributed nature of the electrochemical double layer is better represented with the electrical pseudo-element called constant phase element (CPE). The CPE, which will be described in more details in the next section, has impedance:

$$Z_{CPE} = Y_0^*(j\omega)^{-\alpha} \tag{2.55}$$

where Y_o is the magnitude of the admittance at $\omega = 1$ and α, a constant of numerical value between 0 and 1, takes into account the non-homogeneity of the layer and the roughness of the surface. The Randles equivalent circuit where the capacitor has been substituted by a CPE, is shown in Figure 2.16.

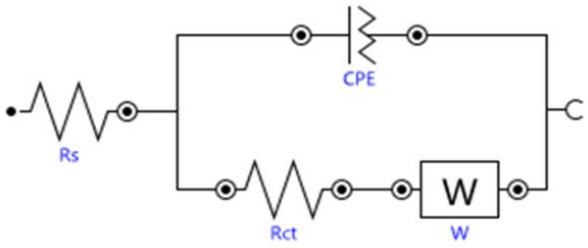

Figure 2.16 Modified Randles equivalent circuit. R_s is the solution resistance, R_{ct} is the charge transfer resistance, CPE is the constant phase element and W is the Warburg element.

In Z_{CPE} both Y_o and α are independent from the frequency. The phase of the CPE can be derived from the formula:

$$\theta_{CPE} = 90° \, (-\alpha) \tag{2.56}$$

For $\alpha = 1$, Z_{CPE} becomes the impedance of a pure capacitor. The capacitance of the double layer can be estimated (Heijne *et al.*, 2013; Bisquert and Fabregat-Santiago, 2010; Hsu and Mansfeld, 2001) as:

$$C_{DL} = \frac{(Y_o R_{ct})^{\frac{1}{\alpha}}}{R_{ct}} \tag{2.57}$$

In real electrochemical experiments Faradaic currents are affected by diffusion processes. Diffusion processes can be modelled in an equivalent circuit by using a distributed element, in series with the charge transfer resistance, called Warburg element (Bard and Faulkner, 1980). The Warburg impedance, Z_W, depends on the concentration of the redox markers and, as for the CPE, is frequency-dependent. Since the Warburg element takes into account the mass transfer processes, it is more predominant at low frequencies. Its impedance is characterised by having equal real and imaginary part of value $\sigma\omega^{-\frac{1}{2}}$ and this results in a 45° line in the complex plane. This type of dependence on the frequency also suggests that the effect of the Warburg impedance at high frequencies is low; in fact, the diffusion processes struggle to follow rapid oscillations of the field. At very high frequencies, the capacitance effect becomes limited as well as the charge transfers at the interface. As a result, the total impedance

of the system at very high frequencies will be given predominantly by the solution resistance (Figure 2.17).

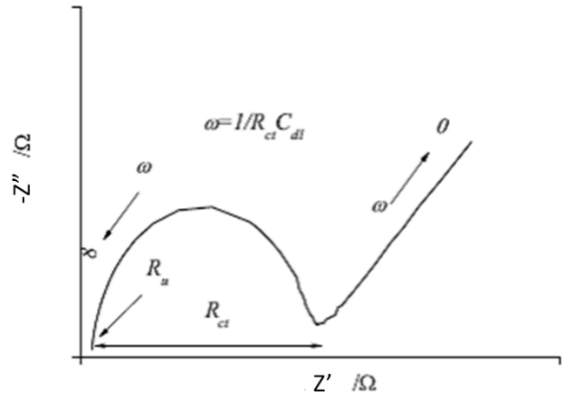

Figure 2.17 Example of complex plane diagram of an EIS measurement

2.3.3 Metal–oxide–semiconductor field-effect transistor

Metal–oxide–semiconductor field-effect transistors (MOSFETs) constitute an underpinning and ubiquitous technology of modern electronics. Alongside the development of MOSFETs, complementary metal–oxide–semiconductor (CMOS) technology has enabled fast and low-cost production of transistors enabling integration of thousands of MOSFETs in a few millimetre square at a very minor cost. Biologically-sensitive field-effect transistors (BioFETs) with extended gold gates have previously been used for the detection of DNA hybridisation (Estrela *et al.*, 2005) and proteins (Estrela *et al.*, 2010).

In a MOSFET device, electrical voltages applied to the terminal called *gate* can modulate the current flowing between the other two terminals called *source* and *drain*. MOSFETs are typically built using silicon as a semiconductor material. Silicon allows the modulation of its conductivity by doping (i.e. adding to) the substrate impurity atoms which can either provide an excess of electrons (n-channels) or holes (p-channels) as charge carriers. Therefore, n-channel or p-channel MOSFETs can be fabricated. In an n-channel MOSFET, for instance, the source and drain are silicon substrates with highly conducting n-channel regions within a p-type silicon substrate,

as shown in Figure 2.18, and the source terminal and the body of the device are grounded.

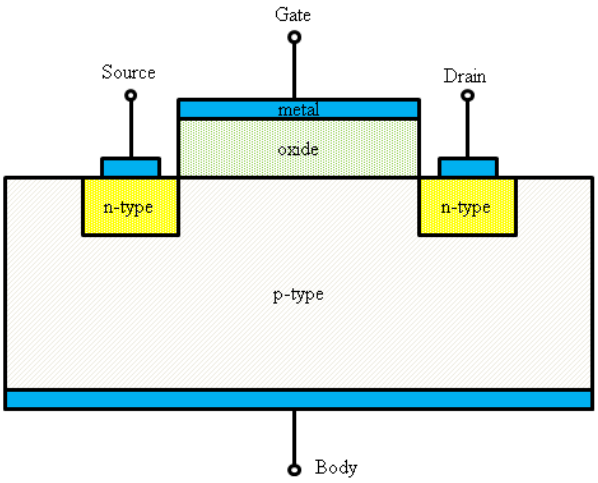

Figure 2.18 Schematic representation of an n-channel type MOSFET

At the interface between the n-types ant the p-type regions, a barrier prevents the flow of the charges between the different doped regions. However, such barrier can be altered by applying a voltage to the gate, which facilitate or further prevents the charge flow between the drain and the source. The minimum potential required to ensure a charge flow between the source and drain regions is called threshold voltage (V_{th}) of the device. In particular, when the potential applied across the gate and the source (V_{gs}) is larger than V_{th} (i.e. V_{gs}>V_{th}), a conducting channel is formed between the source and the drain since the electrons could now flow in this region. Additionally, if a voltage is applied between the drain to source (V_{ds}>0) the current (I_D) begins to flow through the induced channel at the semiconductor. This condition of the device is known as *turn-on* state where the electron-current (I_D) enters the drain and exits the source. Any changes across V_{gs} can modulate the conductivity of the channel and thereby alter I_D. This principle can be exploited by carrying out affinity reactions at the gate of the transistor where molecular probes with high specificity towards an analyte are immobilised. In this way, any changes in the potential generated by the

binding of target molecules onto the gate can alter the conductivity of the device, therefore the detection of the analyte can be achieved.

2.4 Other techniques

2.4.1 Quartz crystal microbalance with dissipation mode

In quartz crystal microbalance (QCM) the mass bound on a gold coated AT-cut quartz can be measured by use of the Sauerbrey equation. For thin, rigid films the Sauerbrey equation (2.58) states that the shift in the resonant frequency, Δf, of a piezoelectric sensor is directly proportional to the amount of mass bound on the sensor surface, Δm (O'Sullivan & Guilbault, 1999), through the relation:

$$\Delta m = \frac{C\Delta f}{n} = \frac{A\sqrt{\mu_q \rho_q}}{2nf_0^2}\Delta f \qquad (2.58)$$

where f_0 is the fundamental frequency of the quartz crystal (Hz), A the sensing area of the electrode (cm^2), μ_q and ρ_q are the shear modulus (2.947×10^{11} g/s^2 cm) and density (2.648 g/cm^3) of the quartz crystal, respectively and n is the overtone number (n = 1, 3, 5. etc). C = 17.7 ng/ Hz cm^2 is the mass sensitivity constant for the AT-cut 5 MHz quartz crystal used in this study.

However, for bound biomolecule layers, a percentage (as high as 95%) of water can be entrapped in the adsorbed film. When water is coupled to the biological layer, a soft and viscoelastic film can form and additional dampening of the quartz oscillator occurs causing an underestimation of the mass if only the Sauerbrey equation is used to model the system (Höök *et al.*, 2001). In fact, the dampening at the interface between the crystal and the liquid phase can be so high to not allow the sensing of the biological molecules entrapped in the water onto the sensor. By measuring both the frequency and dissipation factor of the quartz crystal, quartz crystal microbalance with dissipation mode (QCM-D) can overcome this limitation providing a more accurate estimation of the mass of the layer (Fogel & Limson, 2011). The dissipation factor measures the ratio between the lost energy and the stored energy from the system during one oscillation cycle. The compensation of the viscous energy losses is

achieved using the Voigt model (Voinova *et al.*, 1999; Dutta *et al.*, 2008; Höök *et al.*, 2001). The Voigt model can be implemented by using dedicated software and setting proper values of the film density of and fluid viscosity (typically 1050 kg/m^3 and 0.001 kg/m s, respectively, for protein layers). The corrections to the Sauerbrey model by means of the Voigt study are based on the following relations:

$$\Delta f = \frac{Im(\beta)}{2\pi d_q \rho_q} \tag{2.59}$$

$$\Delta D = \frac{Re(\beta)}{\pi n f_0 d_q \rho_q} \tag{2.60}$$

with

$$\beta = \frac{(2\pi n f_0 \eta \xi_1 - i\mu_q \xi_1)(1-\alpha e^{2\xi_1 d})}{2\pi f\,(1+\alpha\, e^{2\xi_1 d})} \tag{2.61}$$

$$\alpha = \frac{(2\pi f \eta \xi_1 - i\mu\xi_1 + 2\pi f \eta_l \xi_2)}{(2\pi f \eta \xi_1 - i\mu\xi_1 - 2\pi f \eta_l \xi_2)} \tag{2.62}$$

$$\xi_1 = \sqrt{-\frac{(2\pi f)^2 \rho}{\mu + i2\pi f \eta}} \tag{2.63}$$

$$\xi_2 = \sqrt{\frac{i2\pi f \rho_l}{\eta_l}} \tag{2.64}$$

where d_q and μ are the thickness and the shear modulus of the quartz crystal, ρ_l and η_l the bulk liquid density and viscosity, respectively, d the estimated thickness of the layer adsorbed on the electrode and η the shear viscosity.

2.4.2 Localised surface plasmon resonance

Localised surface plasmon resonance (LSPR) occurs when a beam of light shines on a metal with specific permittivity properties such as those having a negative real part and small positive imaginary part (Haynes *et al.*, 2003). The interaction between the photons and the material nanostructures causes collective oscillations (plasmons) of the locally confined valence electrons as shown in Figure 2.19 (Hammond *et al.*, 2014). In an LSPR experiment a beam of light is produced to generate the plasmons. The light reflected is then collected by the transducer. Hitting the metal with a photons

beam, the oscillation and a consequent absorption in the UV/visible range is registered. The LSPR measurement consists in registering the shift in the wavelength of the reflected light generated by the interaction with the surface plasmons. Nevertheless, not all the materials are able to produce plasmons and a consequent shift in wavelength. Amongst those that produce plasmons, the extent of wavelength shift is characteristic of the material involved.

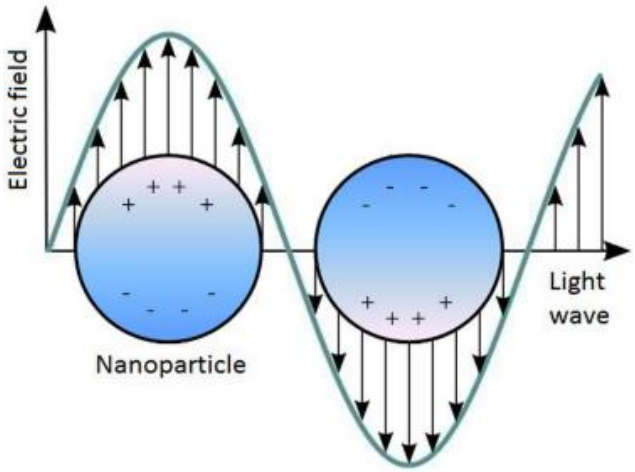

Figure 2.19 Schematic representation of the plasmons in LSPR experiments. The plasmons are generated when the valence electrons in the metal nanostructures collectively oscillate with the field produced by the incident light. Reproduced by Hammond et al. (2014).

The decay length of electromagnetic field associated with the surface plasmons is significantly insensitive to the measurement solution (Haes and Van Duyne, 2003) therefore, LSPR results in a better immunity from interferences with respect to other complex and expensive optical techniques such as surface plasmon resonance (SPR), commonly used for biosensing. This makes LSPR an interesting tool for biosensing applications.

2.4.3 Matrix-assisted laser desorption ionisation-time of flight

Matrix-assisted laser desorption ionisation-time of flight (MALDI-TOF) mass spectrometry exploits the *soft-ionisation* technique for molecules detection. In a

MALDI-ToF experiment, the analyte in a sample is immobilised on a metal plate and is covered by a low molecular weight matrix which provides protons for the ionisation. Then a UV laser beam (usually at frequencies in the UV range) shines on the dry mixture of sample and matrix in a small area, typically less than 0.1 mm radius. When the beam hits the matrix-spotted sample, the energy provided by the UV laser causes the sublimation and ionisation of the analyte resulting in the formation of a *cloud* of ions of different mass accordingly with the nature of the biological sample. The ionisation mostly affects the ribosomal protein which, in microbiology, can give the footprint of the bacteria. The ions of the *cloud* are then accelerated by a strong electrostatic field within a flight tube so that they can reach a detector called mass analyser (Figure 2.20). Here, since the ions are characterised by having certain mass-to-charge (*m/z*) ratios, the time for reaching the detector varies for different ions resulting in a profile of the *time of flight*. The kinetic energy associated with the ions that allows them to be accelerated is provided by the laser beam and is given by:

$$E_K = \frac{1}{2}mv^2 = zV \tag{2.65}$$

where m is the mass of the ion, v is its velocity, z is the charge and V is the potential applied that generates the acceleration. If we consider a certain distance d between the plate where the sample is immobilised and the detector, the time of flight t is given, using (2.65), by (Vékey, 1996; Drahos and Vékey, 2001):

$$t = \frac{d}{v} = d\left(\frac{m}{2zV}\right)^{\frac{1}{2}} \tag{2.66}$$

which demonstrate the correlation between the *m/z* ratio and the time of flight. However, since the distance d and the potential V do not change and for the MALDI TOF z is equal to 1, a direct correspondence between the mass m and the time of flight is achieved.

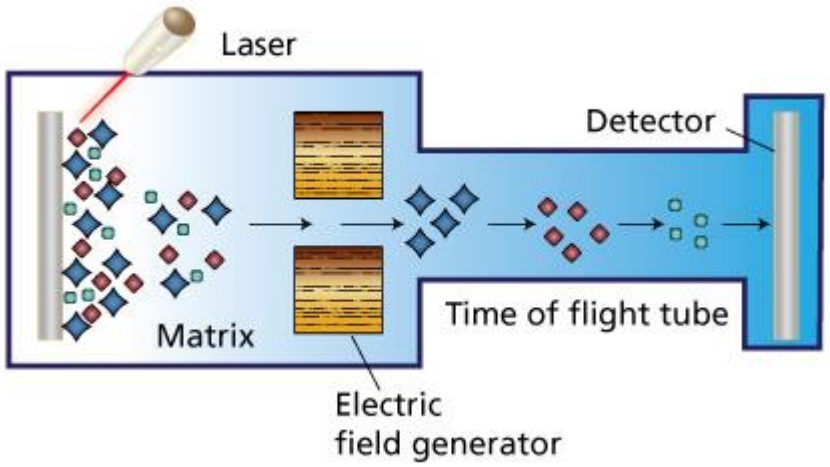

Figure 2.20 Working principle of a MALDI-ToF: a laser beam hits the metal plate where the matrix-spotted sample is immobilised. The ion cloud formed is accelerated through a flight tube and reaches a detector. The time required by different ions to reach the detector is proportional to their mass. In this way a spectrum for different compounds can be obtained. Reproduced from http://www.sigmaaldrich.com/technical-documents/articles/biology/custom-dna-oligos-qc-analysis-by-mass-spectrometry.html (August 2015)

The spectrum obtained is highly specific from sample to sample, therefore, once compared to a library by means of a software it can provide accurate information about the composition of the sample (Clark *et al.*, 2013).

2.5 Self assembled monolayer on gold surfaces

Gold is a common material used in biosensing because of its biocompatibility, ease of manipulation and stability in air and in many solution conditions. Self assembled monolayers (SAMs) made of alkanethiols are intensively used for applications where noble metal surfaces are exploited as sensing areas. Thiols can easily and strongly bind to gold through sulphur-gold bonds forming uniform and well-organised structures (Figure 2.21). The binding of alkanethiols on gold is a covalent, very fast and spontaneous reaction as it decreases the free energy of the gold (Bain *et al.*, 1989a; Bain *et al.*, 1989b; Bain and Whitesides, 1989; Finklea, 1996; Love *et al.*, 2005). In presence of gold, thiols react as follows:

$$RSH + Au \Leftrightarrow RS - Au + H^+ + e^- \quad (2.67)$$

Sulphur binds effectively to gold during the first few minutes of reaction but a uniform and well-organised lateral structure requires not less than 12-16 hours to form (Schreiber, 2000; Colin *et al.*, 1989). During the first minutes of the spontaneous assembly, the alkanethiols lie down on the gold surface (Camillone III., 1994). Later, a crystalline or semicrystalline structure forms due to the effect of the van der Waals forces between the hydrocarbon chains until these reach a tilt angle of about 30º (Love *et al.*, 2005.).

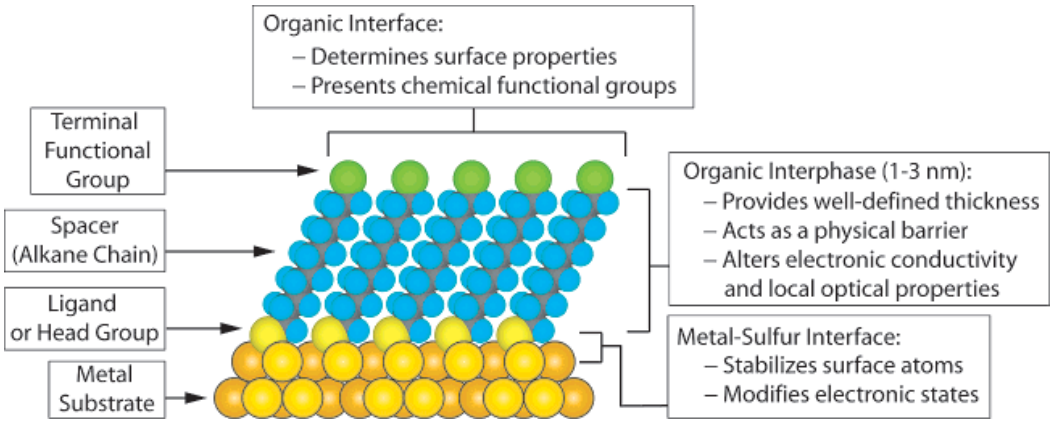

Figure 2.21 Illustration of SAM formation on a gold surface. Reproduced from Love et al. (2005)

The formation of a well-organised SAM strongly depends on the purity of the gold and presence of contaminants as well as on the roughness of the surface where the alkanethiols attach to. For this reason a careful cleaning of the gold surface is required before the SAM immobilisation. SAMs are usually formed by incubating the electrodes in an ethanolic solution (absolute ethanol > 99.9 %) in order to reduce gold oxides. The formation of oxidised layers on the gold surface, for instance due to the use of aqueous solutions for alkanethiols immobilisation, can lead to inhomogeneous and non-reproducible SAM structures (Ron and Rubinstein, 1994; Ron *et al.*, 1998).

The quality of the SAM organisation also depends on the length of the alkane chains (Finklea, 1996). Longer SAMs have been demonstrated to form in more organised structures and to increase the stability of the impedance values over time. It was shown that the distributed molecular interactions (in the normal direction with respect to the

electrode surface) between long adjacent alkane chains make the SAM structure more compact and with a reduced amount of defects (Finklea, 1996; Carrara *et al.*, 2009). SAM structures not only serve as a means to link molecular probes useful for the successive detection but also passivate the electrode surface and prevent non-specific adsorptions (Love *et al.*, 2005). In EIS the conduction currents through alkanethiols (Faradaic or leakage currents in non-Faradaic processes) are described in literature as a result of the so-called tunnelling effect. Here the resistance that contrasts the flow of current is described to be exponentially proportional to the thickness of the SAM length (Miller and Gratzel, 1991; Miller *et al.*, 1991; Finklea, 1996; Becka and Miller, 1992). For alkanethiols having a number of CH_2 groups smaller than 8 (SAM length < 1 nm), an easy permeation of electrolytes happens. For longer alkanethiols, instead, the tunnelling effect is greatly reduced and a better insulating layer can be formed (Schreiber, 2000). Nevertheless, SAMs with a number of alkane chain larger than 8 can be exploited for non-Faradaic measurements in order to achieve insulating SAMs.

Binding of alkanethiols is maximised on Au(111) surfaces reaching a maximum density of $4.64 \times 10^{14}\ molecules/cm^2$ (Love *et al.*, 2005.). Moreover, the nature of the terminal function group (see Figure 2.21) affects the properties of the SAM and the way it interacts with the biological molecules. For instance, a -COOH functional group is commonly used to covalently bind (through its activation as showed in the next Chapter) to the $–NH_2$ groups present on the protein surface. In addition, the use of polyethylene-glycol (PEG) terminated groups can be adopted as a good strategy to confer antifouling properties, i.e. to prevent non-specific interactions (Porter *et al.*, 1987). Whereas SAMs are characterised by a high number of carbon chains or long PEG groups at their extremities, this can result in very long structures which insulating effect can make very challenging for the impedance to be measured. In such cases, and depending on the probe layer that one has to fabricate, the Helmholtz plane could form too far from the electrode surface. As a result the impedance given by the SAM insulating layer – which has to be added to the impedance given by the molecular probe (for instance antibodies) - might mask the impedance signal deriving from the recognition events eventually happening.

From ellipsometry studies, the relation between the number of CH_2 chains (n) and the length of the SAM has been found equal to $0.56n + 4.6$ Å if n is comprised between 9 and 21 (Porter *et al.*, 1987) and the relative capacitance per unit area, C_{SAM}, is given by:

$$\frac{1}{C_{SAM}} = 0.055n + 0.1 \ \frac{cm^2}{\mu F} \tag{2.68}$$

Although in the next chapters basic strategies for improving several EIS systems will be introduced, an optimisation of all the factors is not performed. As a result not in all the example systems the choice of the best SAM has been performed. Nonetheless in Chapter 6 some considerations about the effect of the SAMs is reported. A good compromise between a short and a long SAM structure for Faradaic measurements is represented by mixed SAM made of mercaptoundecanoic acid (MUA) and 6-mercapto-1-hexanol (MCH) (Briand *et al.*, 2006; Jolly *et al.*, 2015; Chen *et al.*, 2014; Chou *et al.*, 2010). In Chapter 4, a DNA aptamer is used for antigen detection, using an initial ratio of aptamer-to-MCH of 1:9. However, it was shown to not be the optimal molar fraction in order to neither maximize the amount of antigen binding nor to obtain the highest EIS signal. Therefore in Chapter 4 the importance of the optimisation of the probe lateral density has been performed.

In other studies, reported in Chapter 6, for non-Faradaic measurements a longer SAM made of a mixture of $(CH_2)_{17}EG_6COOH$ and $(CH_2)_{17}EG_3OH$ (where EG represent the ethylene-glycol unit) has been employed for the detection of bacteria. Here the ionic strength of the measurement solution was changed from 162 mM to 1.62 mM. Such choice results in a better stability of the impedance values over time and guaranteed analyte detection by monitoring the capacitance changes.

2.6 EDC/sulfo-NHS coupling

In the studies presented in Chapter 5 and 6, molecular probes were attached to the linker chains of the SAM by means of 1-ethyl-3-(3-dimethylaminopropyl)carbodiimide/sulfo-N-Hydroxysulphosuccinimide (EDC/sulfo-NHS) chemistry (Hermanson, 2013). The carboxylate groups of the alkanethiols

termination were activated by EDC, whose activity forms highly reactive complexes towards the amine groups of the biological molecules usually present in solution. The complex that results from the activity of EDC is highly unstable in aqueous solutions and could undergo hydrolysis in a few seconds, partially leading to rapid re-formation of carboxylate groups. Yet this can be prevented by the action of sulfo-NHS that generates intermediate active ester functional groups which present better stability in water. In presence of the amino groups, the sulfo-NHS leaves place to a stable and strong amide coupling (Figure 2.22).

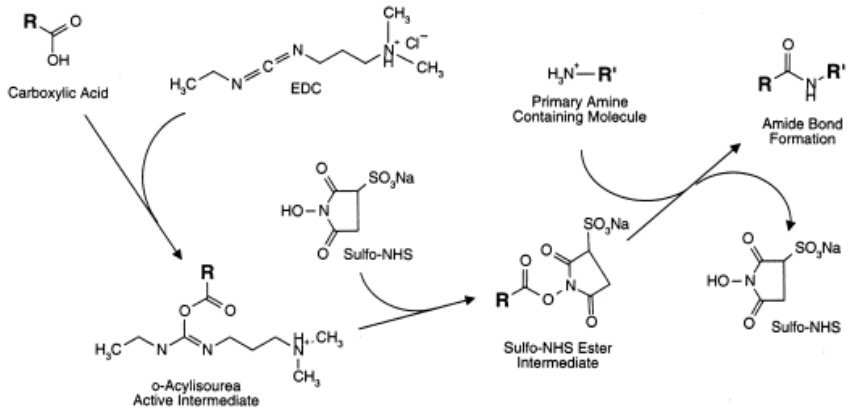

Figure 2.22 Principle of EDC/sulfo-NHS chemistry on COOH-terminated SAMs. Reproduced from (2013).

References

Bain, C. D., Biebuyck, H. A., & Whitesides, G. M. (1989). Comparison of self-assembled monolayers on gold: coadsorption of thiols and disulfides. *Langmuir*, 5(3), 723-727.

Bain, C. D., Evall, J., & Whitesides, G. M. (1989). Formation of monolayers by the coadsorption of thiols on gold: variation in the head group, tail group, and solvent. *Journal of the American Chemical Society*, 111(18), 7155-7164.

Bain, C. D., Troughton, E. B., Tao, Y. T., Evall, J., Whitesides, G. M., & Nuzzo, R. G. (1989). Formation of monolayer films by the spontaneous assembly of organic thiols from solution onto gold. *Journal of the American Chemical Society*, 111(1), 321-335.

Bain, C. D., & Whitesides, G. M. (1989). Formation of monolayers by the coadsorption of thiols on gold: variation in the length of the alkyl chain. *Journal of the American Chemical Society*, 111(18), 7164-7175.

Bard, A. J., & Faulkner, L. R. (2001). *Fundamentals and applications. Electrochemical Methods, 2nd ed.;* Wiley: New York.

Bard, A. J., & Faulkner, L. R. (1980). *Electrochemical methods: fundamentals and applications* (Vol. 2). Wiley: New York.

Barsoukov, E., & Macdonald, J. R. (Eds.). (2005*). Impedance spectroscopy: theory, experiment, and applications.* John Wiley & Sons.

Becka, A. M., & Miller, C. J. (1992). Electrochemistry at. omega.-hydroxy thiol coated electrodes. 3. Voltage independence of the electron tunneling barrier and measurements of redox kinetics at large overpotentials. *The Journal of Physical Chemistry*, 96(6), 2657-2668.

Bisquert, J., & Fabregat-Santiago, F. (2010). Impedance spectroscopy: a general introduction and application to dye-sensitized solar cells. *Dye-Sensitized Solar Cells*, 457, 1-98.

Bisquert, J., Garcia-Belmonte, G., Bueno, P., Longo, E., & Bulhoes, L. O. S. (1998). Impedance of constant phase element (CPE)-blocked diffusion in film electrodes. *Journal of Electroanalytical Chemistry*, 452(2), 229-234.

Brett, C. M., & Brett, A. M. O. (1993). *Electrochemistry: principles, methods, and applications (Vol. 4)*. Oxford: Oxford university press.

Briand, E., Salmain, M., Herry, J. M., Perrot, H., Compère, C., & Pradier, C. M. (2006). Building of an immunosensor: How can the composition and structure of the thiol attachment layer affect the immunosensor efficiency?. *Biosensors and Bioelectronics*, 22(3), 440-448.

Brug, G. J., Van Den Eeden, A. L. G., Sluyters-Rehbach, M., & Sluyters, J. H. (1984). The analysis of electrode impedances complicated by the presence of a constant phase element. *Journal of Electroanalytical Chemistry and Interfacial Electrochemistry*, 176(1), 275-295.

Camillone Iii, N., Eisenberger, P., Leung, T. Y. B., Schwartz, P., Scoles, G., Poirier, G. E., & Tarlov, M. J. (1994). New monolayer phases of n-alkane thiols self-assembled on Au (111): Preparation, surface characterisation, and imaging. *The Journal of Chemical Physics*, 101(12), 11031-11036.

Cammann, K. (1977). Bio-sensors based on ion-selective electrodes. *Fresenius' Zeitschrift für Analytische Chemie*, 287(1), 1-9.

Carrara, S., Bhalla, V., Stagni, C., Benini, L., Ferretti, A., Valle, F., Gallotta, A., Riccò, B. & Samorì, B. (2009). Label-free cancer markers detection by capacitance biochip. *Sensors and Actuators B: Chemical*, 136(1), 163-172.

Chen, H., Mei, Q., Jia, S., Koh, K., Wang, K., & Liu, X. (2014). High specific detection of osteopontin using a three-dimensional copolymer layer support based on electrochemical impedance spectroscopy. *Analyst*, 139(18), 4476-4481.

Chou, T. H., Chuang, C. Y., & Wu, C. M. (2010). Quantification of Interleukin-6 in cell culture medium using surface plasmon resonance biosensors. *Cytokine*, 51(1), 107-111.

Clark, A. E., Kaleta, E. J., Arora, A., & Wolk, D. M. (2013). Matrix-assisted laser desorption ionisation–time of flight mass spectrometry: a fundamental shift in the routine practice of clinical microbiology. *Clinical Microbiology Reviews*, 26(3), 547-603.

Drahos, L., & Vékey, K. (2001). MassKinetics: a theoretical model of mass spectra incorporating physical processes, reaction kinetics and mathematical descriptions. *Journal of Mass Spectrometry*, 36(3), 237-263.

Dutta, A. K., Nayak, A., & Belfort, G. (2008). Viscoelastic properties of adsorbed and cross-linked polypeptide and protein layers at a solid–liquid interface. *Journal of Colloid and Interface Science*, 324(1), 55-60.

Earp, R. L., & Dessy, R. E. (1998). Surface plasmon resonance, in *Commercial Biosensors.* Wiley: New York, 1(148), 99-164.

Earp, R. L., Dessy, R. E., & Ramsay, G. (1998). *Commercial Biosensors*. Wiley: New York, ch. 4.

Estrela, P., Stewart, A. G., Yan, F., & Migliorato, P. (2005). Field effect detection of biomolecular interactions. *Electrochimica Acta*, 50(25), 4995-5000.

Estrela, P., Paul, D., Song, Q., Stadler, L. K., Wang, L., Huq, E., Davis, J. J., Ferrigno, P. K., & Migliorato, P. (2010). Label-free sub-picomolar protein detection with field-effect transistors. *Analytical Chemistry*, 82(9), 3531-3536.

Finklea, H. O. (1996). Electrochemistry of organized monolayers of thiols and related molecules on electrodes. *Electroanalytical Chemistry*, 19, 110-335.

Fogel, R., & Limson, J. L. (2011). Probing fundamental film parameters of immobilized enzymes—Towards enhanced biosensor performance. Part I—QCM-D mass and rheological measurements. *Enzyme and Microbial Technology*, 49(2), 146-152.

Grieshaber, D., MacKenzie, R., Voeroes, J., & Reimhult, E. (2008). Electrochemical biosensors-sensor principles and architectures. *Sensors*, 8(3), 1400-1458.

Hammond, J. L., Bhalla, N., Rafiee, S. D., & Estrela, P. (2014). Localized surface plasmon resonance as a biosensing platform for developing countries. *Biosensors*, 4(2), 172-188.

Haes, A. J., & Van Duyne, R. P. (2003). Nanoscale optical biosensors based on localized surface plasmon resonance spectroscopy. In *Optical Science and Technology, SPIE's 48th Annual Meeting*. International Society for Optics and Photonics. 5221, 47-58

Haynes, C. L., McFarland, A. D., Zhao, L., Van Duyne, R. P., Schatz, G. C., Gunnarsson, L., Prikulis, J., Kasemo, B., & Käll, M. (2003). Nanoparticle optics: the importance of radiative dipole coupling in two-dimensional nanoparticle arrays. *The Journal of Physical Chemistry B*, 107(30), 7337-7342.

Hermanson, G. T. (2013). *Bioconjugate Techniques*. Academic press: Chicago.

Hirschorn, B., Orazem, M. E., Tribollet, B., Vivier, V., Frateur, I., & Musiani, M. (2010). Determination of effective capacitance and film thickness from constant-phase-element parameters. *Electrochimica Acta*, 55(21), 6218-6227.

Homola, J. (2008). Surface plasmon resonance sensors for detection of chemical and biological species. *Chemical Reviews*, 108(2), 462-493.

Homola, J. (Ed.). (2006). *Surface plasmon resonance based sensors* (Vol. 4). Springer Science & Business Media: Germany, 4, 3-44

Höök, F., Kasemo, B., Nylander, T., Fant, C., Sott, K., & Elwing, H. (2001). Variations in coupled water, viscoelastic properties, and film thickness of a Mefp-1 protein film during adsorption and cross-linking: a quartz crystal microbalance with dissipation monitoring, ellipsometry, and surface plasmon resonance study. *Analytical Chemistry*, 73(24), 5796-5804.

Hsu, C. H., & Mansfeld, F. (2001). Technical note: concerning the conversion of the constant phase element parameter Y0 into a capacitance. *Corrosion*, 57(09), 1-2

Janata, J. (2002). Electrochemical sensors ant their impedance: a tutorial. *Critical Reviews in Analytical Chemistry*, 32(2): 109-120

Jolly, P., Formisano, N., Tkáč, J., Kasák, P., Frost, C. G., & Estrela, P. (2015). Label-free impedimetric aptasensor with antifouling surface chemistry: A prostate specific antigen case study. *Sensors and Actuators B: Chemical*, 209, 306-312.

Kasemo, B. (2002). Biological surface science. *Surface Science*, 500(1), 656-677.

Lasia, A. (2002). Electrochemical impedance spectroscopy and its applications. In *Modern Aspects of Electrochemistry*. Springer: USA, 32, 143-248

Li, P. (2008). A study of electrochemical transduction mechanisms in biosensor applications (Doctoral dissertation, University of Cambridge).

Lowe, C. R., Hin, B. F. Y., Cullen, D. C., Evans, S. E., Stephens, L. D. G., & Maynard, P. (1990). *Biosensors. Journal of Chromatography* A, 510, 347-354.

Luppa, P. B., Sokoll, L. J., & Chan, D. W. (2001). Immunosensors—principles and applications to clinical chemistry. *Clinica Chimica Acta*, 314(1), 1-26.

Love, J. C., Estroff, L. A., Kriebel, J. K., Nuzzo, R. G., & Whitesides, G. M. (2005). Self-assembled monolayers of thiolates on metals as a form of nanotechnology. *Chemical Reviews*, 105(4), 1103-1170.

Macdonald, J. R., & Johnson, W. B. (2005). Fundamentals of impedance spectroscopy. *Impedance Spectroscopy: Theory, Experiment, and Applications, Second Edition*, 1-26.

Macdonald, J. R. (1992). Impedance spectroscopy. *Annals of Biomedical Engineering*, 20(3), 289-305.

Madeira, A., Öhman, E., Nilsson, A., Sjögren, B., Andrén, P. E., & Svenningsson, P. (2009). Coupling surface plasmon resonance to mass spectrometry to discover novel protein–protein interactions. *Nature Protocols*, 4(7), 1023-1037.

Miller, C., & Graetzel, M. (1991). Electrochemistry at. omega.-hydroxythiol coated electrodes. 2. Measurement of the density of electronic states distributions for several outer-sphere redox couples. *The Journal of Physical Chemistry*, 95(13), 5225-5233.

Miller, C., Cuendet, P., & Graetzel, M. (1991). Adsorbed. omega.-hydroxy thiol monolayers on gold electrodes: evidence for electron tunneling to redox species in solution. *The Journal of Physical Chemistry*, 95(2), 877-886.

O'Sullivan, C. K., & Guilbault, G. G. (1999). Commercial quartz crystal microbalances–theory and applications. *Biosensors and Bioelectronics*, 14(8), 663-670.

Orazem, M. E., Pébère, N., & Tribollet, B. (2006). Enhanced graphical representation of electrochemical impedance data. *Journal of The Electrochemical Society*, 153(4), B129-B136.

Orazem, M. E., & Tribollet, B. (2008). An integrated approach to electrochemical impedance spectroscopy. *Electrochimica Acta*, 53(25), 7360-7366.

Orazem, M. E., & Tribollet, B. (2011). *Electrochemical impedance spectroscopy* (Vol. 48). John Wiley & Sons: USA.

Xia, Y., Campbell, D. J. (2007). Plasmons: why should we care?. *Journal of Chemical Education* 84(1), 91.

Porter, M. D., Bright, T. B., Allara, D. L., & Chidsey, C. E. (1987). Spontaneously organized molecular assemblies. 4. Structural characterisation of n-alkyl thiol monolayers on gold by optical ellipsometry, infrared spectroscopy, and electrochemistry. *Journal of the American Chemical Society*, 109(12), 3559-3568.

Putzbach, W., & Ronkainen, N. J. (2013). Immobilisation techniques in the fabrication of nanomaterial-based electrochemical biosensors: A review. *Sensors*, 13(4), 4811-4840.

Rinken, T. (2013). *State of The Art in Biosensors-General Aspects*. Intech publications, 277-310.

Ron, H., Matlis, S., & Rubinstein, I. (1998). Self-assembled monolayers on oxidized metals. 2. Gold surface oxidative pretreatment, monolayer properties, and depression formation. *Langmuir*, 14(5), 1116-1121.

Ron, H., & Rubinstein, I. (1994). Alkanethiol monolayers on preoxidized gold. Encapsulation of gold oxide under an organic monolayer. *Langmuir*, 10(12), 4566-4573.

Scholz, F. (2009). *Electroanalytical Methods: Guide to Experiments and Applications*. Springer Science & Business Media.

Schreiber, F. (2000). Structure and growth of self-assembling monolayers. *Progress in Surface Science*, 65(5), 151-257.

Steel, A. B., Herne, T. M., & Tarlov, M. J. (1998). Electrochemical quantitation of DNA immobilized on gold. *Analytical Chemistry*, 70(22), 4670-4677.

Stern, O. (1924). The theory of the electrolytic double-layer. *Z. Elektrochem*, 30(508), 1014-1020.

Su, L., Sankar, C. G., Sen, D., & Yu, H. Z. (2004). Kinetics of ion-exchange binding of redox metal cations to thiolate-DNA monolayers on gold. *Analytical chemistry*, 76(19), 5953-5959.

Su, X., Wu, Y. J., & Knoll, W. (2005). Comparison of surface plasmon resonance spectroscopy and quartz crystal microbalance techniques for studying DNA assembly and hybridisation. *Biosensors and Bioelectronics*, 21(5), 719-726.

Ter Heijne, A., Schaetzle, O., Gimenez, S., Fabregat-Santiago, F., Bisquert, J., Strik, D. P., Barrière, F., Buisman, C. J. N., & Hamelers, H. V. (2011). Identifying charge and mass transfer resistances of an oxygen reducing biocathode. *Energy & Environmental Science*, 4(12), 5035-5043.

Thévenot, D. R., Toth, K., Durst, R. A., & Wilson, G. S. (2001). Electrochemical biosensors: recommended definitions and classification. *Biosensors and Bioelectronics*, 16(1), 121-131.

Vékey, K. (1996). Internal energy effects in mass spectrometry. *Journal of Mass Spectrometry*, 31(5), 445-463.

Voinova, M. V., Rodahl, M., Jonson, M., & Kasemo, B. (1999). Viscoelastic acoustic response of layered polymer films at fluid-solid interfaces: continuum mechanics approach. *Physica Scripta*, 59(5), 391.

Chapter 3. EIS applications for biosensing

3.1 Introduction

Rapid and cost-effective sensors for early stage detection of markers (i.e. molecules specifically associated to a particular disease) is crucial for point-of-care diagnosis and much effort in research has been put in the last decades for their development. Label-free sensors are very intensively studied, as the lack of the labelling processes lowers their individual costs and the reduced sample preparation results in more rapid tests when compared to enzyme or fluorescent-labelled assays (Keighley *et al.*, 2008).

Since its introduction in biosensing applications, EIS was often only employed as a characterisation technique, in particular for confirming the layer by layer fabrication of the sensors (Jaffrezic-Renault, 2013). However, EIS has gained much more popularity recently and the number of biosensors based on impedimetric measurements rapidly increased in the last years. Currently EIS represents one of the most promising label-free measurement techniques and it has been demonstrated to be able to reach sensitivities down to the femto and attomolar ranges (Bertok *et al.*, 2013; Berggren *et al.*, 2001; Kongsuphol *et al.*, 2014). Despite the diffusion of EIS sensors, some systems do not allow a straightforward application of the impedimetric principles for sensing because of several factors. Primarily, the use of this technique is still hampered by the intrinsic complexity of the electrochemical systems which makes the data obtained difficult to interpret. In addition, the dependence of the EIS

signals on different factors generates the need of a careful optimisation of the systems to be analysed.

In this chapter the basis of EIS will be analysed and then attention will be given to some of the aspects that must be addressed for widening the application of EIS to biosensing. These aspects include observing the size and charge combined effect, the optimisation of surface density for aptamer-based applications, the implementation of non-Faradaic measurements and the challenges that could be overcome introducing to the use of signal probes.

3.2 Basis of an EIS system

EIS is theoretically based on a very simple concept: a *molecular trap*, which we will call a *probe*, is immobilised on an electrode and when the capture of the target takes place, the addition of such molecules causes changes in the properties of the sensors. In a three-electrode system under controlled conditions of applied a.c. potentials, the changes in the sensor properties cause variations of the flow of current. Using the values of the applied potentials and the measured currents one can quantitatively define the parameter that we call *impedance* and associate it to the changes of the physico-chemical properties at the electrode interface. Moreover, if the impedance is measured over a wide range of frequencies, it is referred to as *impedance spectroscopy* and can give a more complete characterisation of the electrochemical system if compared to traditional electrochemical techniques where only the sum of Faradaic and non-Faradaic measurements are obtained (Park and Yoo, 2003).

One of the biggest advantages of EIS is the possibility to differentiate the different phenomena happening at the electrochemical double layer, for instance the charge transfer, the diffusion transport or the double layer formation. At the same time this requires a wise use of the analytical data in order to interpret and extract the parameters that one is looking for (Vladikova, 2003). It is only by applying a model (such as an equivalent electrical circuit) that it is possible to associate values of impedance to the chemico-physical property of the system. One example is the Randles equivalent circuit (Figure 2.15) that can be used to describe a simple EIS system and takes into

account both the Faradaic and non-Faradaic components of the currents which sum can be derived from the Butler-Volmer equation (2.26). As introduced in Chapter 2, in amperometric sensors the non-Faradaic component is generally considered to be the noisy part of the total current and hence, efforts are put to reduce or eliminate its contribution (see DPV, Chapter 2). In EIS the non-Faradaic behaviour can be analysed by studying the capacitive component of the Randles equivalent circuit and it can provide information as useful as the Faradaic under particular conditions. This will be described in the next sections. Exploiting a broad range of frequencies, information such as the solution resistance can be obtained (to be more accurate, it can be isolated) as well as the mass transport of the redox species within the solution can be studied by means of the Warburg element. The resistor in series with it denotes the charge transfer resistance, which multiplies together with the capacitance to give rise to the time constant of the reaction:

$$\tau^* = C_{DL} \times R_{ct} \tag{3.1}$$

The final analysis of an EIS experiment consists in interpreting the changes in impedance and assigning quantifiable values to the capacitive and resistive components of the equivalent electrical circuit (the Warburg element is also used at times for the analysis) at different frequencies. Such values are directly related to the phenomena happening at the sensor interface. Some more straightforward approaches to prove the binding events have been reported and consist of the direct analysis of the impedance values or the impedance phase shifts (Zaccari *et al.*, 2014).

In the next sections, a few considerations are presented with respect to the circuit elements of the generalised Randles equivalent circuit (introduced in Chapter 2) and the Faradaic and non-Faradaic processes.

3.2.1 Constant phase element (CPE)

The concept of constant phase element (CPE) can be applied to any circuit element that is found to be dependent upon the frequency with a relation distant from an ideal

behaviour. In the particular case of EIS sensors, the non-ideal behaviour is caused by the roughness and inhomogeneity of the surface properties (Vladikova, 2004).

In reality, the concept of CPE can be only applied to the capacitors used to describe the charged separation layers. Bisquert *et al.* (2000) reported on the inaccuracy that often results when using capacitors as equivalent elements for the behaviour of porous electrodes. This is due to the excessive idealisation of the phenomena happening at the electrode interface which are, instead, far from an ideal behaviour because of the inhomogeneity, complexity and absence of order that often characterize such electrodes. In fact, what is not considered in ideal capacitors is the charge dispersion at the surfaces interface which can modify the dependency of the capacity on the frequency. In practice, the description of the double layer through a CPE becomes necessary especially considering the improved accuracy achieved for the mathematical fitting when replacing common capacitors (Hsu and Mansfeld, 2001). Since the CPE is introduced to describe a non-ideal behaviour in non-ideal systems, there is a discrepancy in literature about how to extract the exact value of impedance from it. The most common spread relationship used is (Gamry instruments; Bisquert *et al.*, 2000; Hsu and Mansfeld, 2001; Terezo *et al.*, 2001; Martens *et al.*, 1997; Barsoukov and Macdonald, 2005):

$$Z_{CPE} = Y_0^*(j\omega)^{-\alpha} \tag{3.2}$$

where Y_0^* is the magnitude of the admittance of the system at $\omega = 1rad/s$ and α, the exponent of the CPE, can only have a value between 0 and 1. For $\alpha = 1$, the expression of Z_{CPE} becomes the impedance of a pure capacitor.

It should be noted that sometimes the following definition for Z_{CPE} can also be found (Boukamp; Eco Chemie):

$$Z_{CPE} = (Y_o j\omega)^{-\alpha} \tag{3.3}$$

Although the discrepancy between the two formula can be not particularly significant, the main difference is mostly in the dimensional unit of the parameter Y_0^* and Y_o which can be either $F\ s^{1-\alpha}$ or $F^{-\alpha}\ s^{1-\alpha}$, respectively.

An estimation of the value of capacitance associated to the CPE can be obtained by:

$$C_{Est} = \frac{(Y_o R_{ct})^{\frac{1}{\alpha}}}{R_{ct}} \tag{3.4}$$

In cases of homogeneous layers, a variation of the CPE is given by introducing the bounded constant phase element (BCP) having equation (3.5), which at high frequencies can be described by a classic CPE.

$$Z_{BCP} = Y_0^{*-1}(j\omega)^{-\alpha} \tanh[R_o Y_0^*(j\omega)^{\alpha}] \tag{3.5}$$

3.2.2 Resistance

The resistance of an equivalent circuit models the phenomenon of dissipation of energy, the presence of potential barriers or processes that limit the charge transfer. In common electrochemical systems three types of resistance are usually found: the solution resistance (R_s), the polarisation resistance (R_p) and the charge transfer resistance (R_{ct}). The solution resistance depends on the ionic concentration in the electrochemical cell, as well as its physical nature, such as temperature and the geometry of the cell and is described by equation (3.6) where l is the distance between the electrodes (cm), λ is the conductance ($S\ cm^{-1}$) and A is the area (cm^2):

$$R_s = \frac{l}{\lambda A} \tag{3.6}$$

The polarisation resistance, R_p, is the resistance that is opposed to the flow of current when the electrode is polarised, i.e. it is forced to be at a potential different from its open circuit potential. R_p becomes the charge transfer resistance, R_{ct}, when the overpotential η (i.e. the difference between the potential applied and the equilibrium potential) is of small entity, namely $|F\eta| < RT$. The R_{ct} can be obtained by the relation:

$$R_{ct} = \frac{\eta}{i} = \frac{RT}{F i_0} \tag{3.7}$$

3.2.3 Faradaic EIS experiments

In a typical EIS experiment performed under Faradaic conditions the electrochemical cell contains both reduced and oxidised forms of a redox couple (e.g. $[Fe(CN)_6]^{3-/4-}$ which were used in this study). The redox probes facilitate the charge transfer, thus, the Faradaic current that can flow through the working electrode. The equilibrium potential across the working electrode and the reference electrode is dependent upon the ratio between the concentrations of the oxidised and reduced forms of the redox couple and can therefore change according to this proportion. In the studies presented in this thesis, Ag/AgCl and Hg/Hg_2SO_4 reference electrodes have been used.

Typical Faradaic EIS experiments consist of recording the variations in the electrical current generated by the redox probes due to the obstructing effect of the analyte. In fact a binding event can produce a higher or lower blocking effect that changes the accessibility of the redox markers to the electrode surface. In particular, the impedance of a probed system can increase because of the blocking effect generated by the "bulky" properties of the analyte or because of an increased electrostatic barrier that impedes the redox probes to approach the electrode surface. Reductions in the impedance value can be due to a decrease of the electrostatic barrier onto the sensor surface (e.g. if molecules having opposite sign with respect to the redox probes are bound on the surface) or to changes in the molecules conformation. More complicated situations can arise if the signal change is due to a combination of different effects, as for the study reported in Chapter 4. Such cases can result in situations where the conditions of maximum analyte binding do not comport a maximum impedance signal change. To the best of our knowledge there are no previous studies that report on similar cases, thus the finding reported in Chapter 4 can be of significant importance.

An aspect to consider about the use of redox probes is that although they can facilitate the impedance analysis, their use would be challenging in real applications and could therefore be in part limited to laboratory studies.

3.2.4 Non-Faradaic EIS experiments

For non-Faradaic processes particular importance can be given to the analysis of the double layer capacitance C_{DL} rather than R_{ct}. Indeed, in non-Faradaic experiments the charge transfer can be neglected and the main contribution to the impedance is given by the capacitive component (Tsouti *et al.*, 2011). In such cases, if we consider a generic EIS experiment having impedance:

$$Z = Z' + jZ'' \tag{3.8}$$

and define a complex capacitance given by the following relationship:

$$C^* = \frac{1}{j\omega Z} \tag{3.9}$$

one approach for calculating the capacitance of the electrochemical system (Formisano *et al.*, 2015; Jolly *et al.*, 2015) can be obtained by using (3.8) in (3.9):

$$C^* = -\frac{Z''}{\omega|Z|^2} - j\frac{Z'}{\omega|Z|^2} = C' + jC'' \tag{3.10}$$

Calculating C' and C'' from the measured values of Z' and Z'', the *complex capacitance* can be plotted (in Figure 3.2 an example is shown).

Another approach reported in literature, as well as suggested by several electrochemical software produced by companies such as Ivium Technologies for the C_{DL} calculation in non-Faradaic experiment is based on the assumption that the charge transfer resistance and the diffusion contributions can be neglected (Couniot *et al.*, 2015). Therefore the electrical equivalent circuit becomes a resistor in series with a capacitor as shown in Figure 3.1.

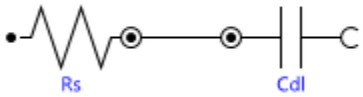

Figure 3.1 electrical equivalent circuit for non-Faradaic measurements based on the assumption that charge transfer processes and diffusion contribution can be neglected.

As a result, the total impedance is given by:

$$Z = Z' + jZ'' \cong R_S^* - j\frac{1}{\omega C_{DL}^*} \tag{3.11}$$

from which the real part of the capacitance is:

$$C_{DL}^* = -\frac{1}{\omega Z''} \tag{3.12}$$

In the studies here reported, the use of equation (3.12) versus the use of C' from equation (3.10) for the calculation of the capacitive changes led to a maximum of 4.0 % difference only.

Using non-Faradaic EIS experiments a large number of studies on capacitive sensors have been reported (Tsouti *et al.*, 2011; Berggren *et al.*, 2001, Daniels and Pourmand, 2007). The first capacitive biosensor was reported by Newman and co-workers (1986) based on interdigitated electrodes (IDEs). At present, most capacitive sensors are based on IDEs and on electrode-solution interfaces. IDE sensors exploit changes in the permittivity given by the biological sample. Sensors based on electrode-solution interfaces (as those reported in the present dissertation), instead, exploit also the changes in the distance between the separation planes of the pseudo-capacitor and the displacement of ions and solvated molecules from the sensing surface (Tsouti *et al.*, 2011; Daniels and Pourmand, 2007). IDEs can be miniaturised by exploiting standard lithography fabrication techniques. These sensors are characterised by having significant losses of the electrical field usable for the analysis due to the fringing effect at the edges of the conductive combe-structure where the biological sample is not immobilised.

A drawback of capacitive sensors based on electrode-solution interfaces is the need to form good insulating layers on top of the electrode surface. This can be achieved by fabricating compact and defect-free SAMs which prevent leakage currents. Leakage currents are responsible for short-circuiting the metal and solution phases producing a loss of sensitivity (Berggren *et al.*, 2001). Thus, well-organised and insulating SAMs are desired for capacitive measurements. In order to achieve insulating SAMs, a good

option consists in the use of SAMs with a number of alkane chains larger than 8 and having polyethylene-glycol (PEG) terminated groups. On the other hand, long SAMs produce a small capacitance which can partially or totally mask the effect of the analyte binding on top of the so modified electrode due to the principle that in a series of capacitances the smallest dominates the total capacitance. Furthermore, it is worth noticing that the surface chemistry used for immobilizing the probes onto SAMs can affect the insulating properties of the surface. It has been shown that the immobilisation strategy using 1-ethyl-3-(3-dimethylaminopropyl)carbodiimide/N-Hydroxysulphosuccinimide chemistry (EDC/NHS) is amongst the best in order to retain the insulating properties of the SAM (Mirsky *et al.*, 1997).

According to the literature, binding events happening onto capacitive sensors' surfaces (the same consideration can be extended for generic EIS sensors) produce contradictory signal changes: both increases and decreases in capacitance are reported even using the same type of sensor and analyte as molecular targets (Daniels and Pourmand, 2007). Reasonable explanations are given each time in order to explain the signal change in a particular case. However no specific studies have been carried out so far in order to clearly correlate molecular phenomena to EIS changes in a broader context. For this reason, different authors attribute the signal changes obtained to various factors such as changes in the dielectric properties, the displacement of water molecules, electrostatic repulsions between immobilised samples and ions in solution, the change of the molecular conformation onto the surface electrodes and so on.

Putting the work of this dissertation in such a context, the results obtained here, especially those reported in Chapter 6 where capacitive measurements are performed, are critically analysed each time and confronted with what has already been reported in literature.

3.2.5 Challenges in EIS applications

Significant variations in the impedimetric signals are not always generated in an experiment upon the recognition of a target. It may happen that the changes at the micro-nano scale of the properties at the electrode-solution interface upon binding do

not generate a significant signal to be measured. In addition, cases where the magnitude of the impedance change is expected to be larger than the actual measured signal can arise. It may be that the single properties cause contrasting effects so that the overall signal does not correlate to the binding event with an appropriate sensitivity. This case is faced in Chapter 4 where the combined effect of mass loading and changes of surface charge result in a decrease of EIS signals.

Another issue that can arise in an electrochemical system when it is analysed by means of EIS is that the molecular layer formed at the interface between the electrode and the solution might not be capable of retaining its properties over time or, simply, it takes a certain amount of time to reach a state of equilibrium. In this case the system is referred to as *not stable* and it means that the impedance values keep changing over time even if no external changes are applied to the system. Often in the literature a study can be found where more or less significant intervals of time are required for the systems to stabilize so that reliable EIS measurements could be taken. Different studies report on checking the stability for intervals of time ranging from several hours to a few days (Jolly *et al.*, 2015; Guo *et al.*, 2011). Factors that can affect the stabilisation of the sensor properties at the interface electrode-measurement solution can be the cleanliness of the sensor surface, the SAM formation, the probe orientation, eventual blocking steps used and the type of molecular target. Such delay, obviously, is not ideal for real sensor applications. In order to reduce the stability issues, all the mentioned steps must be properly controlled by applying the same conditions and meticulous care has to be adopted in the sensor fabrication.

EIS measurements have been greatly simplified with the introduction of frequency response analysers (FRAs). However, sweeping the frequencies in a relatively wide band (typically EIS experiments are performed in the window 0.1 Hz – 100 KHz) can end up in a long acquisition time (note that only frequencies lower than 1 KHz produce a time consuming response), especially when compared with other electrochemical techniques such as DPV or chronocoulometry. Studies that aimed to accelerate the measurement time were based on adopting fast Fourier transform (FFT) methods

applied on current responses to noise signals instead of frequency scanning as for conventional EIS (Jeno *et al.*, 1997; Házì *et al.*, 1998). A similar but simplified approach led to a decrease down to 0.1 second for the measurement time although the scan was limited to fewer frequencies (Popkirov and Schindler, 1992). Later on, further improved methods based on FFT to EIS were reported using multisine ac scanning combined with staircase voltammetry (Rosvall and Sharp, 2000) or with cyclic voltammetry (Darowicki *et al.*, 2000; Pettit *et al.*, 2006). An improved strategy combining the application of sinusoidal a.c. signals with chronoamperometry readings and the application of FFT was also reported (Chang *et al.*, 2008; Mozaffari *et al.*, 2009).

Despite the efforts towards reducing the acquisition times introducing new strategies, in this dissertation the example systems have been investigated through the use of conventional EIS. However, although a full frequency scan is essential for the initial investigations of a new EIS sensor, which comports longer acquisition times, single frequency acquisition points are demonstrated in order to meet the criteria of real biosensing applications. In fact, upon an initial characterisation of the electrochemical system, the electrochemical response at only a single frequency can provide reliable proof of the marker binding. The frequency to choose can be selected as the one that minimizes the imaginary components of the electrical elements associated with the system. This would be the frequency at which the contribution of the imaginary impedance finds its minimum. In a general complex plane diagram (Figure 2.17), it corresponds to the point of relative minimum of Z'' and the semicircle that it forms can give an indication of the R_{ct}. In order to study single-point responses, in non-Faradaic processes the real capacitance of the system can be obtained by applying the same considerations valid for the charge transfer: the double layer capacitance can be graphically obtained by the amplitude of the semicircle in the complex capacitance plot (Figure 3.2).

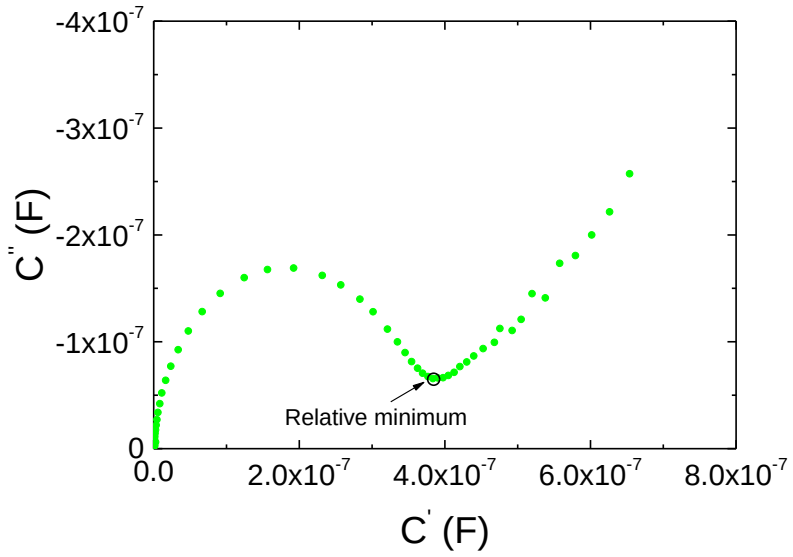

Figure 3.2 Example of complex capacitance plot. The red circle and the arrow indicate the relative minimum of the imaginary part of capacitance at which the real part of the capacitance is sampled.

An EIS system can be modelled by an equivalent electric circuit and the charge transfer is represented by the resistive component R_{ct}. However in case of non-properly clean electrodes or oxidation of the gold, impurities can adsorb on the surface, therefore well organised SAMs might not form (Schreiber, 2000; Love *et al.*, 2005). In particular, the oxidation of gold electrodes is not recommendable since the oxide surface formed on gold is not stable and therefore the adsorption of adventitious organic materials can occur as a means to lower its free energy (Love *et al.*, 2005) Alkanethiolated SAMs can show hydrophobic properties that help in repelling water molecules at the electrode-solution interface resulting in a blocking step towards non-specific targets (Herne and Tarlov, 1997). Furthermore, the solvent molecules and the ions in solution will form the Helmholtz plane onto the SAM layer at a distance defined by the length of the alkane chains, thus affecting the capacitance given by the electrochemical double layer. This means that things can dramatically change in case of non-properly distributed SAM structures: significant gold areas could be not properly insulated by SAM molecules and hence directly exposed to the charge carriers in the solution. Such a condition results in a different model of the system where parts of the area of the sensor can be represented by short-circuits. In terms of

EIS analysis this implies a more complicated study and signals not easily correlated with the amount of analyte binding. It was also demonstrated that even after a formation of mixed a SAM, a further backfilling step would further cover empty spaces on the gold surface (Formisano *et al.*, 2015; Jolly *et al.*, 2015).

3.3 Electrode fabrication and cleaning

The first step in order to ensure a good SAM formation is a proper surface cleaning prior the alkanethiols adsorption (Love *et al.*, 2005). The presence of pinholes reduces the compactness of the SAM layer providing the access to the gold surface for the molecules in solution. Pinholes are likely to be dependent mostly on the cleanliness and purity of the gold layer (Zhao *et al.*, 1996). Different procedures are reported in literature for the gold electrodes cleaning such as chemical (Steel *et al.*, 1998; Aoki and Tao, 2007; Ron *et al.*, 1998; Creager *et al.*, 1992), mechanical (Hoogvliet *et al.*, 2000), thermal (Burke *et al.*, 2001) and electrochemical cleaning (Hoogvliet *et al.*, 2000; Dijksma *et al.*, 2000). In this study, commercial gold macro-electrodes were cleaned with the following procedure: a sonication of 10 min in acetone and in ethanol respectively, in order to provide an initial gross removal of organic and non-organic compounds from previous experiment was followed by 3 min of mechanical polishing on pads using diamond slurry of 1 µm diameter. Successive 5 min mechanical polishing on pad with alumina slurry 50 nm (Buehler) and on 2 min on pad with only ultrapure water steps were performed. The mechanical polishing were intervalled by 10 min of sonication in ethanol for removing the compounds non-specifically adsorbed on the gold. After the mechanical polishing a strong oxidizing treatment to remove organic contaminants was performed by means of piranha solution dipping the electrodes in a mixture of 3 parts of concentrated H_2SO_4 and 1 part of H_2O_2 for 10 min. After a thorough rinsing with ultrapure water and further sonication in ethanol, the electrodes underwent electrochemical cleaning in 0.5 M H_2SO_4 solution by applying 50 CV cycles (or repeating the procedure until the CV cycles reached a steady state) from 0 to 1.5 V *vs.* Ag/AgCl reference electrode, at a scan rate of 200 mV/s, (Figure 3.3). The CV scans further remove both contaminants and gold oxide

by repetitively oxidising and reducing the gold surface and finely smoothened the electrode area. Finally the electrodes where rinsed, dried and ready for the overnight SAM immobilisation.

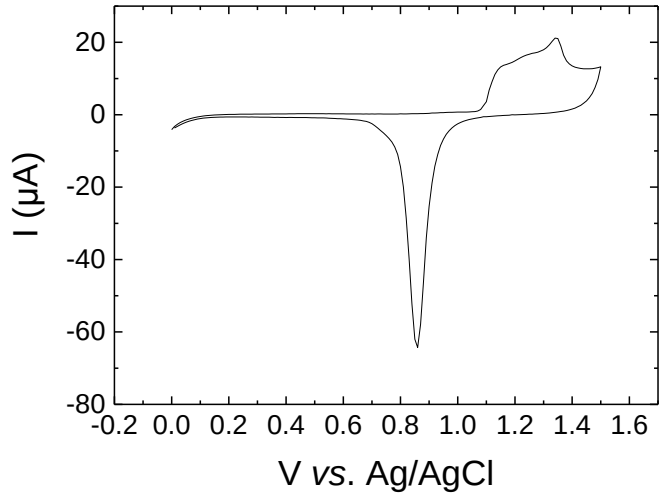

Figure 3.3 Example of electrochemical cleaning performed on bulk gold electrode in 0.5 M H_2SO_4 solution. For clarity only the last CV cycle is shown in the plot.

In case of evaporated gold electrodes (Figure 3.4), these were in-house prepared on glass slides supports using a thermal evaporator (BOC Edwards, UK). The process performed under fine vacuum (2.0×10^{-6} mbar) consists of an initial evaporation of 20 nm of chromium on glass followed by an evaporation step of a thicker layer (usually between 100 and 200 nm) of gold. Chromium was used as in intermediate layer since gold does not naturally adhere to glass. The glass slides used for this process were previously cleaned by undergoing RCA cleaning: the electrodes were firstly dipped into a mixture made of 1 part of NH_4OH, 1 part of H_2O_2 and 5 parts of H_2O pre-heated at 80 ºC for the removal of organic and particles contaminants and then in a mixture made of 1 part of HCl, 1 part of H_2O_2 and 5 parts of H_2O pre-heated at 80 ºC to remove metallic ion contaminants.

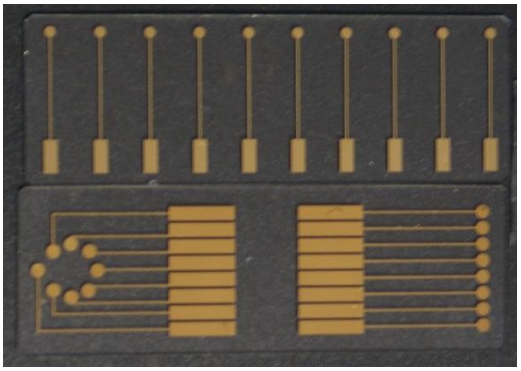

Figure 3.4 Gold electrodes obtained by means of thermal evaporation on glass slides.

3.4 EIS apparatus and methods

EIS measurements were carried out in a 3-electrode set up as shown in Figure 2.2. An Hg/Hg_2SO_4 (BASi, USA) or an Ag/AgCl were used as reference electrodes and a platinum wire as a counter electrode (ALS, Japan). Macroelectrodes (CH Instruments, USA) have 1.0 mm radius and followed the cleaning described in the previous section previous to their use. A μAUTOLAB III / FRA2 potentiostat (Metrohm, Netherlands) and a CompactStat potentiostat (Ivium Technologies, The Netherlands) were used for the measurement readings. For the Faradaic processes, measurements were taken with the use of the $[Fe(CN)_6]^{3-/4-}$ redox couple. The measurement solution was chosen accordingly to the experiments performed. EIS measurements were taken by scanning the frequencies between 100 KHz and 0.1 Hz of an a.c. potential voltage of 10 mV superimposed to the d.c. formal potential of the $[Fe(CN)_6]^{3-/4-}$ redox couple (*vs.* the relative reference electrode used). In case of non-Faradaic processes, the measurements were taken in the same frequency window applying a 10 mV a.c. voltage with respect to the open circuit potential. All chemicals were of analytical grade and were used as received, unless otherwise specified. Aqueous solutions were obtained using double de-ionised water, 18.2 MΩ cm, with a Pyrogard filter (Millipore, USA).

For the EIS signal changes, as well as when other techniques were used, in the studies presented in this dissertation

3.5 Charge and size effects on the EIS signal

The analysis of EIS experiments is mostly performed by recording the changes of the charge transfer resistance and the double layer capacitance which rely on either the modifications in the surface charge or on the mass loading effect. It follows, quite straightforwardly, that limitations in gathering a detectable EIS signal can arise from binding of small and uncharged analytes. On the other hand, the bigger and more electrostatically charged is the target molecule, the more favourable is the EIS detection (Daniels and Pourmand, 2007). To be more general, the EIS signal change can also arise from altered properties of the probe layer used for targeting the analyte. In the case of a DNA sensor, for instance, the charge present on the geometrical plane of oligonuceotidic probes can be greatly affected upon the binding of the target. An increased electrostatic barrier against redox markers in solution can be obtained when the complementary DNA strands are hybridised. Conversely, a screening of the DNA layer can be obtained when neutrally or oppositely charged molecules, such as antigens, are bound.

Preliminary experiments carried out in the course of this doctorate consisted in performing EIS measurements upon testosterone binding using a specific antibody. Although the optimisation of an EIS sensor for testosterone detection could not be completed due to budget and timing limitations, this study provided interesting starting results. Gold macroelectrodes were modified with a mixed SAM made of MUA:MCH 1mM in a ratio 1:9 and an antibody raised against testosterone was attached by means of EDC/sulfo-NHS chemistry and unreacted activated sites were blocked by using 10 mM ethanolamine (see Figure 3.5 for a schematic description of the essay).

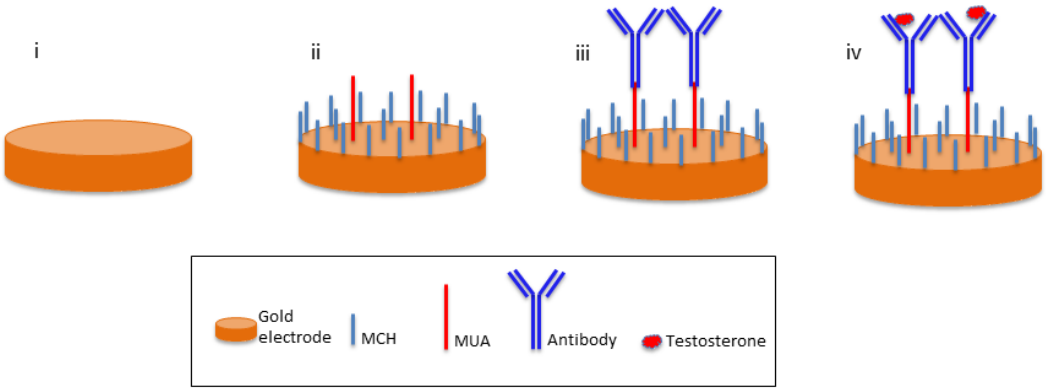

Figure 3.5 Immobilisation steps performed to obtain testosterone detection: cleaned gold macroelectrodes (i) were functionalised with a mixed SAM made of MUA:MCH in a ratio 1:9 (ii); successively testosterone antibody was immobilised on the SAM by means of EDC/sulfo-NHS chemistry (iii) and a final testosterone step was performed (iv) after a blocking step with ethanolamine (not reported) to block the non-reacted activated carboxylic groups.

Faradaic measurements were performed in 50 mM PB + 100 mM K_2SO_4 buffer with addition of 10 mM $[Fe(CN)_6]^{3-/4-}$ applying -0.190 V *vs.* Hg/Hg_2SO_4 reference electrode. Although the validity of the essay was confirmed by a colorimetric technique (TMB assay), the measurements did not produce any significant shift in the R_{ct} and C_{DL}. In fact, upon immobilisation of up to 35 µM of testosterone, both variations in R_{ct} and C_{DL} - calculated using (2.57) - were limited to values smaller than 3 % (the modified Randles equivalent circuit was applied for fitting the complex impedance plot). The complex impedance plot of one testosterone experiment is reported in Figure 3.6. EIS detection was impeded by the characteristic of the target molecule. Indeed, testosterone is a small molecule (288 Dalton) that neither alters significantly the electrostatic charge upon binding the antibody (which has a molecular weight of about 150,000 Dalton) nor produces a significant mass layer addition onto the electrode area. As a result, no significant changes were produced in terms of electrostatic barrier, water molecule displacement or obstructing effect at the electrode interface able to induce EIS changes.

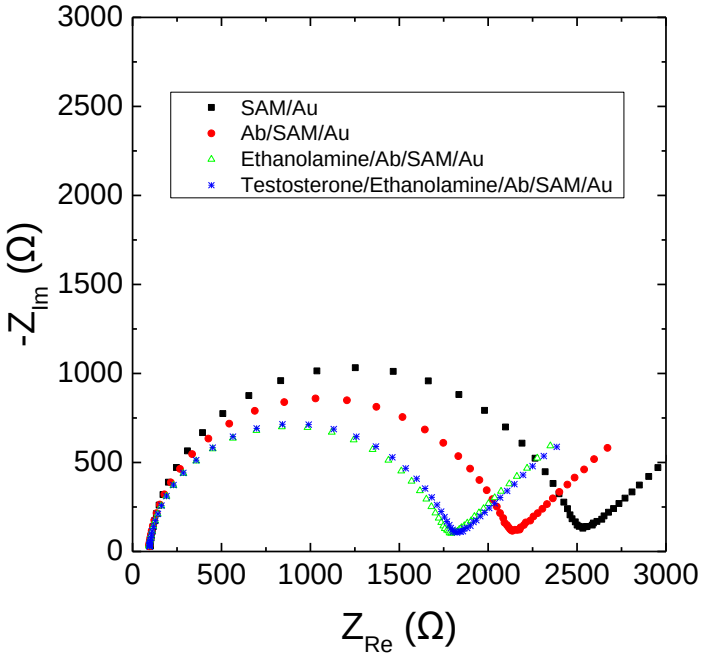

Figure 3.6 Complex impedance plots performed for testosterone detection. Gold macroelectrodes were modified with a mixed SAM made of MUA:MCH 1mM in a ratio 1:9 and 150 nM antibody raised against testosterone was attached by means of a 40 mM EDC and 10 mM sulfo-NHS solution. Unreacted activated sites were blocked by using 10 mM ethanolamine and a solution of 100 nM of testosterone was used for the final binding. EIS measurements were performed in 50 mM PB + 100 mM K_2SO_4 with addition of 10 mM $[Fe(CN)_6]^{3-/4-}$.

In Chapter 4 and 6, example systems in which the EIS signals are dependent upon modifications of the surface charge and mass loading (produced by big molecules such as cells and bacteria), are instead reported. It can be noted that using similar SAMs and surface chemistry, bigger and charged molecules are able to produce significant EIS changes without the need of using complex strategies.

3.6 Optimisation of the surface probe density in DNA-based sensors

In electrochemical oligonucleotide-based sensors, the capture of a target causes an alteration of the charge onto the electrode surface. For instance, a typical indicator of hybridisation detection in DNA-DNA interaction is the increase of negative charge upon binding. Such changes in the double layer charge have been proved to be measured by means of field effect-devices (Souteyrand *et al.*, 1997; Fritz *et al.*, 2002)

and EIS (Bardea *et al.*1999, Patolsky *et al.*2001, Liu *et al.*2005). In EIS experiments the electrostatic charge of the nucleotides acts as a barrier towards the redox probes resulting in variations of the R_{ct}. However, the charge of the nucleotides can be screened because of the counterion condensation effect if the salt concentration of the measurement solution is too high or the length of the DNAs is too long (Rant *et al.*, 2003; Deserno *et al.*, 2000).

3.6.1 DNA aptamer-based sensors

In Chapter 4 the optimisation of an aptasensor is reported with main focus on the surface probe density and on the combined effect that the mass loading and the charge changes have on the overall EIS signal. Aptamers represent a novel frontier towards electrochemical biosensing. They have been initially studied as a means for targeting diseases and in the last decades have also gained much attention for biosensing applications (Hianik & Wang, 2009; Iliuk *et al.*, 2011). Aptamers are DNA or RNA sequences, small in size, and can be synthesised for targeting a higher variety of analytes such as amino acids, peptides, proteins, drugs, whole cells not scarifying affinities and sensitivities if compared to antibodies (Song *et al.*, 2008). This class of molecules have the interesting property of undergoing conformational changes when the target is captured: it is said that the aptamer folds in its secondary structure (Hermann & Patel, 2000; Song *et al.*, 2008; Hianik & Wang, 2009). This property made aptamers being exploited as a biosensing probe element (Clark & Remcho, 2002; Tombelli *et al.*, 2005; Willner & Zayats, 2007; Mairal *et al.*, 2008; Song *et al.*, 2008; Liu *et al.*, 2012). Aptamers are mostly thought as an alternative solution to the use of antibodies. Currently antibodies still represent the gold standard in current clinical biosensing, nevertheless they are affected by some disadvantages such as the *in vivo* production that implies not simple manipulating processes and can dramatically increase the batch-to-batch variability (Keefe *et al.*, 2010). In addition, the integration of antibodies into biosensor platforms is difficult to achieve in real applications due to their relatively short shelf life (McKeague *et al.*, 2011). On the other hand, unlike antibodies, DNA aptamers can be produced *in vitro* by means of the Systematic Evolution of Ligands by Exponential enrichment (SELEX) process (Stoltenburg *et al.*,

2007). The introduction of innovative *in vitro* selection techniques for DNA aptamers allowed their production with high purity, reproducibility and chemical stability (Xiao *et al.*, 2005).

3.6.2 Optimisation of DNA aptamer-based sensors

Despite the advantages with respect to antibodies, the introduction of EIS aptamer-based sensors has been hampered by several drawbacks or factors that must be taken in consideration for their development. For instance, a careful optimisation is required in order to reduce undesired signals and this involves the choice of an optimal DNA density coverage. The amount of aptamer able to effectively capture the antigen is also correlated to the steric hindrance effect. The steric hindrance effect occurs when chemical interactions are prevented because of an excess of molecule density. In that respect the nucleotidic density coverage modulates the aptamer-aptamer interactions since repulsive forces between the strands can generate. The importance of optimizing the DNA or PNA lateral density for DNA detection was already previously reported (Keighley *et al.*, 2008a; Keighley *et al.*, 2008b). Ideal aptasensors are characterised by having good hybridisation efficiency and low non-specific interactions. Therefore the choice of the SAM and the type of molecules used are crucial factors for the development of an effective aptasensor. Moreover, the hydration, charge and conformation of the biomolecular sensing layer and the buffer condition can have a major impact on the EIS signals (Radi and O'Sullivan, 2006) and the affinity towards the target can be affected by the buffer conditions.

When gold surfaces are used as electrodes for electrochemical sensors, thiol-chemistry is one of the most popular choices for building SAMs. A good strategy for reducing the non-specific adsorptions consists in employing a mixed SAM where spacer molecules ensure both the repulsion for undesired molecules attachment and good spacing conditions for minimizing the steric hindrance effect. Yet the search for an optimum surface probe density is essential for guaranteeing the best efficiency for a DNA-based sensor. Using long chain alkanethiols one can obtain well organised SAMs with a higher degree of order because of the increased van der Waals forces

that stabilize the structure (Darling *et al.*, 2002). On the other side, long-chains may result in having the binding of target molecules too far from the electrode surface (with respect to the Debye length). For Faradaic EIS this is a non-convenient condition for measuring changes in R_{ct}. Conversely, short-chain alkanethiols can form a higher number of defects in the SAM but the successive binding event can take place at a reasonable distance from the electrode surface. Thus the length of the SAM molecules, along with the optimal lateral probe density must be decided when designing an aptasensor. A good compromise is represented by adopting a mixed SAM made of thiolated DNA aptamer and MCH as a spacer element. MCH ensures a good electron transfer for tunnelling effect since the length of MCH molecules is smaller than 9 Å (Nogues *et al.*, 2004). In addition, MCH molecules help the aptamer strands to stand in the up-right position enabling better capturing properties towards the target (Levicky *et al.*, 1998). The use of thiolated aptamer allowed to reduce the immobilisation steps by avoiding the alkanethiol aptamer coupling.

In this context, in Chapter 4, valuable information obtained by means of Quartz Crystal Microbalance with Dissipation mode (QCM-D) was used in order to optimize the EIS response and find the optimal aptamer:MCH ratio for a PSA aptasensor. QCM-D is used as a mass sensor which can provide data on the biolayer hydration, hence on the viscoelastic properties at the interface. Therefore using QCM-D we can relate on the optimal conditions for PSA binding at different surface coverage density. We then correlated these data with the EIS responses.

3.7 Are label-free techniques the right choice?

The advantages of label-free biosensors have been mentioned in the previous sections. However drawbacks of label-free techniques include low sensitivity, at times, and the possible lack of specificity (Tsouti *et al.*, 2011; Li and Wu, 2013; Vestergaard *et al.*, 2007). Although amongst the label-free sensors EIS is one of the most promising, this technique is not employed in current central laboratories. Moreover, the actual gold standards for clinical detection are still represented by *indirect labelling* techniques such as fluorescent methods and ELISA (Hu *et al.*, 2014). In indirect-labelling techniques, the signal probe is not attached on the target prior the capturing but is

added afterwards to form the so-called sandwich essay. In this way, the binding properties of the target are not affected by an eventual tag which can physically occupy the binding site. In addition, if we consider Faradaic EIS experiments, redox probes are required and their use in a clinical laboratory is challenging to imagine. Conversely, although labelling-processes can be time-consuming, expensive and sometimes make use of hazardous reagents, they allow to reach good levels of sensitivity as well as to discriminate true positives. Firstly, it is worth reminding ourselves that label-free technologies often require very elaborated readout methods in order to catch the small surface properties changes upon target binding and convert them in a quantifiable signal. Secondly, real biosensing applications will likely be performed on complex matrixes, for instance blood samples, where the interference of non-specific proteins, such as albumin and immunoglobulin, represent up to the 65 % of the proteomic content of the specimen (Vestergaard *et al.*, 2007). Such abundancy of molecules can mask the real signal, impede an accurate detection and introduce false positives (Daniels and Pourmand, 2007). In Chapter 5, this aspect will be highlighted showing a system where the compounds used to carry out *in vitro* a chemical reaction that naturally occurs *in vivo*, namely protein phosphorylation, produce non-reproducible results. Moreover, it was not possible to clearly discriminate protein phosphorylation reactions. For analogy, thus, we can imagine such interaction as something that could occur in real human samples.

Therefore, the label-free aspect of EIS sensors must be addressed in a more critique manner and the possibility of introducing signal probes has to be considered in those cases where a greater efficacy can be achieved for detecting the desired markers. A more detailed literature review about contradictory results obtained using EIS for protein phosphorylation is reported in Chapter 5.

Another consideration about the use of signal probes is that they can enable multi-modal detections, i.e. using different techniques. Indeed, it is not rare to find studies where EIS has been used in combination with field-effect devices (Estrela *et al.*, 2008) or with other electrochemical (Hu *et al.*, 2013; Erdem *et al.*, 2012; Raoof *et al.*, 2009; Keighley *et al.*, 2008), optical (Formisano *et al.*, 2015; Patskovsky *et al.*, 2014; Vandenryt *et al.*, 2013; Lu *et al.*, 2012), piezoelectric (Briand *et al.*, 2010; Estrela *et*

al., 2008) techniques and so on. Such combinations are adopted in order to increase the reliability of single techniques and reduce the cases of false positives. In this context, signal enhancers such as gold nanoparticles or redox probes can be exploited for the generation of signals in different types of techniques.

References

Aoki, H., & Tao, H. (2007). Label-and marker-free gene detection based on hybridisation-induced conformational flexibility changes in a ferrocene–PNA conjugate probe. *Analyst*, 132(8), 784-791.

Barsoukov, E., & Macdonald, J. R. (Eds.). (2005). *Impedance Spectroscopy: Theory, Experiment, and Applications*. John Wiley & Sons.

Berggren, C., Bjarnason, B., & Johansson, G. (2001). Capacitive biosensors. *Electroanalysis*, 13(3), 173-180.

Bertok, T., Sediva, A., Katrlik, J., Gemeiner, P., Mikula, M., Nosko, M., & Tkac, J. (2013). Label-free detection of glycoproteins by the lectin biosensor down to attomolar level using gold nanoparticles. *Talanta*, 108, 11-18.

Bisquert, J., Garcia-Belmonte, G., Fabregat-Santiago, F., Ferriols, N. S., Bogdanoff, P., & Pereira, E. C. (2000). Doubling exponent models for the analysis of porous film electrodes by impedance. Relaxation of TiO_2 nanoporous in aqueous solution. *The Journal of Physical Chemistry B*, 104(10), 2287-2298.

Boukamp, B. A. (2000). FRA Software for autolab electrochemical instrumentation. *Eco Chemie BV*, Utrecht: The Netherlands.

Briand, E., Zäch, M., Svedhem, S., Kasemo, B., & Petronis, S. (2010). Combined QCM-D and EIS study of supported lipid bilayer formation and interaction with pore-forming peptides. *Analyst*, 135(2), 343-350.

Burke, L. D., Hurley, L. M., Lodge, V. E., & Mooney, M. B. (2001). The effect of severe thermal pretreatment on the redox behaviour of gold in aqueous acid solution. Journal of Solid State Electrochemistry, 5(4), 250-260. *State Electrochemistry*, 5(4):250-260, 2001.

Creager, S. E., Hockett, L. A., & Rowe, G. K. (1992). Consequences of microscopic surface roughness for molecular self-assembly. *Langmuir*, 8(3), 854-861.

Chang, B. Y., Ahn, E., & Park, S. M. (2008). Real-time staircase cyclic voltammetry Fourier transform electrochemical impedance spectroscopic studies on underpotential

deposition of lead on gold. *The Journal of Physical Chemistry C*, 112(43), 16902-16909.

Couniot, N., Afzalian, A., Van Overstraeten-Schlögel, N., Francis, L. A., & Flandre, D. (2015). Capacitive biosensing of bacterial cells: Analytical model and numerical simulations. *Sensors and Actuators B: Chemical*, 211, 428-438.

Daniels, J. S., & Pourmand, N. (2007). Label-free impedance biosensors: Opportunities and challenges. *Electroanalysis*, 19(12), 1239-1257.

Darling, S. B., Rosenbaum, A. W., Wang, Y., & Sibener, S. J. (2002). Coexistence of the $(23\times\sqrt{3})$ Au (111) reconstruction and a striped phase self-assembled monolayer. *Langmuir*, 18(20), 7462-7468.

Darowicki, K., Orlikowski, J., & Lentka, G. (2000). Instantaneous impedance spectra of a non-stationary model electrical system. *Journal of Electroanalytical Chemistry*, 486(2), 106-110.

Deserno, M., Holm, C., & May, S. (2000). Fraction of condensed counterions around a charged rod: Comparison of Poisson-Boltzmann theory and computer simulations. *Macromolecules*, 33(1), 199-206.

Dijksma, M., Kamp, B., Hoogvliet, J. C., & Van Bennekom, W. P. (2000). Formation and electrochemical characterisation of self-assembled monolayers of thioctic acid on polycrystalline gold electrodes in phosphate buffer pH 7.4. *Langmuir*, 16(8), 3852-3857.

Erdem, A., Muti, M., Papakonstantinou, P., Canavar, E., Karadeniz, H., Congur, G., & Sharma, S. (2012). Graphene oxide integrated sensor for electrochemical monitoring of mitomycin C–DNA interaction. *Analyst*, 137(9), 2129-2135.

Estrela, P., Paul, D., Li, P., Keighley, S. D., Migliorato, P., Laurenson, S., & Ferrigno, P. K. (2008). Label-free detection of protein interactions with peptide aptamers by open circuit potential measurement. *Electrochimica Acta*, 53(22), 6489-6496.

Finklea, H. O. (1996). Electrochemistry of organized monolayers of thiols and related molecules on electrodes. *Electroanalytical Chemistry*, 19, 110-335.

Formisano, N., Bhalla, N., Wong, L. C., Di Lorenzo, M., Pula, G., & Estrela, P. (2015). Multimodal electrochemical and nanoplasmonic biosensors using ferrocene crowned nanoparticles for kinase drug discovery applications. *Electrochemistry Communications*, 57, 70-73.

Guo, X., Kulkarni, A., Doepke, A., Halsall, H. B., Iyer, S., & Heineman, W. R. (2011). Carbohydrate-based label-free detection of Escherichia coli ORN 178 using electrochemical impedance spectroscopy. *Analytical Chemistry*, 84(1), 241-246.

Házì, J., Elton, D. M., Czerwinski, W. A., Schiewe, J., Vicente-Beckett, V. A., & Bond, A. M. (1997). Microcomputer-based instrumentation for multi-frequency Fourier transform alternating current (admittance and impedance) voltammetry. *Journal of Electroanalytical Chemistry*, 437(1), 1-15.

Herne, T. M., & Tarlov, M. J. (1997). Characterisation of DNA probes immobilized on gold surfaces. *Journal of the American Chemical Society*, 119(38), 8916-8920.

Hoogvliet, J. C., Dijksma, M., Kamp, B., & Van Bennekom, W. P. (2000). Electrochemical pretreatment of polycrystalline gold electrodes to produce a reproducible surface roughness for self-assembly: a study in phosphate buffer pH 7.4. *Analytical Chemistry*, 72(9), 2016-2021.

Hsu, C. H., & Mansfeld, F. (2001). Technical note: concerning the conversion of the constant phase element parameter Y0 into a capacitance. *Corrosion*, 57(09).

Hu, C., Yang, D. P., Wang, Z., Yu, L., Zhang, J., & Jia, N. (2013). Improved EIS performance of an electrochemical cytosensor using three-dimensional architecture Au@ BSA as sensing layer. *Analytical Chemistry*, 85(10), 5200-5206.

Hu, J., Wang, S., Wang, L., Li, F., Pingguan-Murphy, B., Lu, T. J., & Xu, F. (2014). Advances in paper-based point-of-care diagnostics. *Biosensors and Bioelectronics*, 54, 585-597.

Gamry Instruments. (2005). *Electrochemical Impedance Spectroscopy Primer*. Warminster, PA, 6.

Jaffrezic-Renault, N. (2013). label-free affinity biosensors based on electrochemical impedance spectroscopy. In *Microelectrode Biosensors*. Humana Press, 80, 295-318.

Jolly, P., Formisano, N., Tkáč, J., Kasák, P., Frost, C. G., & Estrela, P. (2015). Label-free impedimetric aptasensor with antifouling surface chemistry: A prostate specific antigen case study. *Sensors and Actuators B: Chemical*, 209, 306-312.

Keighley, S. D., Estrela, P., Li, P., & Migliorato, P. (2008). Optimisation of label-free DNA detection with electrochemical impedance spectroscopy using PNA probes. *Biosensors and Bioelectronics*, 24(4), 906-911.

Keighley, S. D., Li, P., Estrela, P., & Migliorato, P. (2008). Optimisation of DNA immobilisation on gold electrodes for label-free detection by electrochemical impedance spectroscopy. *Biosensors and Bioelectronics*, 23(8), 1291-1297.

Kongsuphol, P., Ng, H. H., Pursey, J. P., Arya, S. K., Wong, C. C., Stulz, E., & Park, M. K. (2014). EIS-based biosensor for ultra-sensitive detection of TNF-α from non-diluted human serum. *Biosensors and Bioelectronics*, 61, 274-279.

Levicky, R., Herne, T. M., Tarlov, M. J., & Satija, S. K. (1998). Using self-assembly to control the structure of DNA monolayers on gold: a neutron reflectivity study. *Journal of the American Chemical Society*, 120(38), 9787-9792.

Li, J., & Wu, N. (Eds.). (2013). *Biosensors Based on Nanomaterials and Nanodevices*. CRC Press.

Love, J. C., Estroff, L. A., Kriebel, J. K., Nuzzo, R. G., & Whitesides, G. M. (2005). Self-assembled monolayers of thiolates on metals as a form of nanotechnology. *Chemical Reviews*, 105(4), 1103-1170.

Lu, J., Wang, W., Wang, S., Shan, X., Li, J., & Tao, N. (2011). Plasmonic-based electrochemical impedance spectroscopy: Application to molecular binding. *Analytical Chemistry*, 84(1), 327-333.

Mertens, S. F., Xhoffer, C., De Cooman, B. C., & Temmerman, E. (1997). Short-term deterioration of polymer-coated 55% Al-Zn-Part 1: Behavior of thin polymer films. *Corrosion*, 53(5), 381-388.

Mirsky, V. M., Riepl, M., & Wolfbeis, O. S. (1997). Capacitive monitoring of protein immobilisation and antigen–antibody reactions on monomolecular alkylthiol films on gold electrodes. *Biosensors and Bioelectronics*, 12(9), 977-989.

Mozaffari, S. A., Chang, T., & Park, S. M. (2009). Diffusional electrochemistry of cytochrome c on mixed captopril/3-mercapto-1-propanol self-assembled monolayer modified gold electrodes. *The Journal of Physical Chemistry C*, 113(28), 12434-12442.

Nogues, C., Cohen, S. R., Daube, S. S., & Naaman, R. (2004). Electrical properties of short DNA oligomers characterized by conducting atomic force microscopy. *Physical Chemistry Chemical Physics*, 6(18), 4459-4466.

Park, S. M., & Yoo, J. S. (2003). Peer reviewed: electrochemical impedance spectroscopy for better electrochemical measurements. *Analytical Chemistry*, 75(21), 455-A.

Patskovsky, S., Latendresse, V., Dallaire, A. M., Doré-Mathieu, L., & Meunier, M. (2013). Combined surface plasmon resonance and impedance spectroscopy systems for biosensing. *Analyst*, 139(3), 596-602.

Peterson, B. W., Sharma, P. K., van der Mei, H. C., & Busscher, H. J. (2012). Bacterial cell surface damage due to centrifugal compaction. *Applied and Environmental Microbiology*, 78(1), 120-125.

Pettit, C. M., Goonetilleke, P. C., Sulyma, C. M., & Roy, D. (2006). Combining impedance spectroscopy with cyclic voltammetry: Measurement and analysis of kinetic parameters for Faradaic and nonFaradaic reactions on thin-film gold. *Analytical Chemistry*, 78(11), 3723-3729.

Popkirov, G. S., & Schindler, R. N. (1992). A new impedance spectrometer for the investigation of electrochemical systems. *Review of Scientific Instruments*, 63(11), 5366-5372.

Porter, M. D., Bright, T. B., Allara, D. L., & Chidsey, C. E. (1987). Spontaneously organized molecular assemblies. 4. Structural characterisation of n-alkyl thiol

monolayers on gold by optical ellipsometry, infrared spectroscopy, and electrochemistry. *Journal of the American Chemical Society*, 109(12), 3559-3568.

Rant, U., Arinaga, K., Fujiwara, T., Fujita, S., Tornow, M., Yokoyama, N., & Abstreiter, G. (2003). Excessive counterion condensation on immobilized ssDNA in solutions of high ionic strength. *Biophysical Journal*, 85(6), 3858-3864.

Raoof, J. B., Hejazi, M. S., Ojani, R., & Hamidi-Asl, E. (2009). A comparative study of carbon nanotube paste electrode for development of indicator-free DNA sensors using DPV and EIS: Human interleukin-2 oligonucleotide as a model. *International Journal of Electrochemical Science*, 4, 1436-1451.

Ron, H., Matlis, S., & Rubinstein, I. (1998). Self-assembled monolayers on oxidized metals. 2. Gold surface oxidative pretreatment, monolayer properties, and depression formation. *Langmuir*, 14(5), 1116-1121.

Rosvall, M., & Sharp, M. (2000). A complete system for electrochemical impedance spectroscopy which combines FFT methods and staircase voltammetry. *Electrochemistry Communications*, 2(5), 338-343.

Schreiber, F. (2000). Structure and growth of self-assembling monolayers. *Progress in Surface Science*, 65(5), 151-257.

Steel, A. B., Herne, T. M., & Tarlov, M. J. (1998). Electrochemical quantitation of DNA immobilized on gold. *Analytical Chemistry*, 70(22), 4670-4677.

Terezo, A. J., Bisquert, J., Pereira, E. C., & Garcia-Belmonte, G. (2001). Separation of transport, charge storage and reaction processes of porous electrocatalytic IrO_2 and IrO_2/Nb_2O_5 electrodes. *Journal of Electroanalytical Chemistry*, 508(1), 59-69.

Tsouti, V., Boutopoulos, C., Zergioti, I., & Chatzandroulis, S. (2011). Capacitive microsystems for biological sensing. *Biosensors and Bioelectronics*, 27(1), 1-11.

Vandenryt, T., Pohl, A., van Grinsven, B., Thoelen, R., De Ceuninck, W., Wagner, P., & Opitz, J. (2013). Combining electrochemical impedance spectroscopy and surface plasmon resonance into one simultaneous read-out system for the detection of surface interactions. *Sensors*, 13(11), 14650-14661.

Vestergaard, M., Kerman, K., & Tamiya, E. (2007). An overview of label-free electrochemical protein sensors. *Sensors*, 7(12), 3442-3458.

Vladikova, D. (2004, September). The technique of the differential impedance analysis. Part I: Basics of the impedance spectroscopy. In *Proceedings of the International Workshop "Advanced Techniques for Energy Sources Investigation and Testing*, 4-9.

Zaccari, I., Walti, C., & Laurenson, S. X. (2014, December). Label-free electrochemical biosensors for clinical diagnostic. In *Biomedical Engineering Conference (CIBEC), 2014 Cairo International*, *IEEE*, 15-18

Zhao, X. M., Wilbur, J. L., & Whitesides, G. M. (1996). Using two-stage chemical amplification to determine the density of defects in self-assembled monolayers of alkanethiolates on gold. *Langmuir*, 12(13), 3257-3264.

Chapter 4. The effect of mass loading and charge on EIS signals

The work presented in this Chapter has been partly published (Formisano *et al.*, 2015).

4.1 Introduction

As is the case with the majority of electrochemical techniques, EIS systems require careful optimisation of the experimental conditions in order to maximize the reading response. In particular, the optimisation of the sensor surface modification can play a vital role in the maximisation of an EIS signal. In a general context, the response of an EIS sensor using DNA aptamers can be affected by the DNA density, charge and conformational changes upon DNA-target binding and buffer conditions. In addition, the mass loading effect upon the target recognition causes signal changes too. These are the motivations that bring us to analyse the results reported in the next sections, where the issue of optimising an EIS sensor, with a main focus on the surface modification, is faced. Moreover, the combined effect of the mass loading and of the analyte charge, two of the main intrinsic properties of a molecular target, are analysed.

Following it is reported a case study where an aptasensor for prostate specific antigen (PSA) detection is used as biorecognition element. The optimisation of the impedimetric aptasensor has been achieved by using supporting techniques such as Quartz Crystal Microbalance with Dissipation mode (QCM-D) and chronocoulometry.

One of the most important parameters requiring optimisation was the aptamer lateral density, i.e. the number of aptamer molecules per unit of area. The effect of the aptamer lateral density was investigated since it can have a major impact on the microscopic environmental properties and therefore on the aptamer conformation which can alter the ability to capture the targets (Pestourie *et al.*, 2006; Radi & O'Sullivan, 2006). In addition, the secondary structure of the aptamer also plays an important role since EIS signals can be affected by the redistribution of the charges that they cause upon the analyte binding.

It is worthy of remark that the work presented in this Chapter is directly intended to serve as a case study to prove some of the aforementioned properties of EIS systems. The fabrication of an effective aptasensor for PSA detection, instead, was developed in another work led by Jolly *et al.* (2015a) and thus is not presented here.

4.2 PSA as a biomarker for prostate cancer

At present, the chances of a man developing prostate cancer in the course of his lifetime are high. Nevertheless, it might happen that a person can live for many years with the cancer until death occurs because of other unrelated causes. In terms of mortality rates however, prostate cancer still represents the second worldwide leading cause of cancer-related death amongst men (Ferlay *et al.*, 2013). In fact, the slow progression of the disease and the lack of evident symptoms of its development often leads to a late diagnosis of the tumour, leaving the person with poor probability of being effectively treated and hence, surviving. At present, collection of tissue samples through a biopsy and histological test are the most reliable screenings for prostate cancer (Lilja *et al.*, 2008; Gilgun *et al.*, 2013). However infections, complications and other inconveniences can manifest because of this procedure (Basch *et al.*, 2012). The decision of whether or not to perform a biopsy is carefully taken and relies on preliminary screenings such as digital rectal examination and the measurement of PSA blood levels. Values of PSA into the blood above 120 pM are considered to be related to pathogenic conditions (Gilgunn *et al.*, 2013). PSA is a 33-34 kDa glycoprotein produced by the prostate. Tissue damage in the prostate due to cancer leads to releases

of PSA into the bloodstream with a consequent increase of its levels in the serum. However, PSA levels can be altered also for other reasons unrelated to cancer (Carter *et al.*, 1992) and this makes its use for biosensing matter of debate among scientists.

Although the aim of this study did not consist in developing a new biosensor for PSA detection, a vast literature reports on different types of sensors. Studies can be found on electrochemical and chemi-luminescent sensors (Okuno *et al.*, 2007; Panini *et al.*, 2008; Albrecht *et al.*, 1994; Seto *et al.*, 2001), ELISA assays (Acevedo *et al.*, 2002) as well as sensors based on cantilevers (Wee *et al.*, 2005). Amongst the electrochemical sensors, Arya & Bhansali (2012) proposed a sensing system where gold electrodes are functionalised with a cysteamine-based SAM by using conventional EDC/NHS chemistry. Li *et al.* (2005) proposed a combined use of In_2O_3 nanowires and p-type carbon nanotubes, where antibodies are immobilised through succinimidyl linking molecules. Chiriacò *et al.* (2013) developed an EIS sensor for both total and free PSA detection on gold electrodes by exploiting two different antibodies and using a SAM made of 11-mercaptoundecanoic acid and 2-mercaptoethanol and EDC/NHS chemistry.

The above mentioned assays however, are mostly based on the use of antibodies as recognition elements. One of the alternatives to antibodies are aptamers which can offer several advantages over the former. Extensive research is being carried out to prove whether antibodies can be replaced by aptamers to develop a real and effective biosensor for clinical applications.

4.3 Aptasensors for PSA detection

Jolly *et al.* (2015b) recently reported about advances in the field of DNA aptamer sensors with respect to prostate cancer detection, following the recent development of a sequence specific for this target (Savory *et al.*, 2010). An RNA aptamer sequence specific for PSA was also found and developed (Jeong *et al.*, 2010) but its high number of nucleotidic bases makes the use and production more difficult compared to the DNA aptamer. At present, only a few studies have been focused on PSA detection using DNA aptamers.

With respect to aptamer-based sensors for PSA detection, a strategy based on DPV was developed by Liu *et al.* (2012), exploiting a graphite electrode with gold nanoparticles encapsulated by graphitised mesoporous carbon and biotinylated-aptamer/streptavidin coupling. This biosensor achieved a limit of detection (LOD) of 7 pM with a dynamic range from 7 pM to 6 nM. Cha *et al.* (2014) reported on a chemiluminescent resonance energy transfer aptasensor for PSA with an LOD of 30 pM. A chemiluminescent aptasensor that is able to remove impurities that hamper PSA detection in human serum with sensitivity comparable to enzyme immunoassays was developed by Choi and Lee (2013). Another sensor, developed by Ma *et al.* (2014), was based on surface-enhanced Raman scattering in serum samples showing a detection limit of 5 aM. Chen *et al.* (2012) proposed the use of an optical method of detection in the range 4 pM to 3 nM with LOD of ~1 pM, based on a resonance light-scattering (RLS) and gold nanoparticles assay where the changes in aptamer conformation upon PSA recognition is exploited.

With respect to EIS detection, an aptasensor was reported by Jolly *et al.* (2015a) exploiting the anti-fouling properties of sulfo-betaine molecules for the formation of the SAM, whereas Yang *et al.* (2015) reported on PSA detection using aptamers following both an in-solution strategy using a DNA intercalator and on-chip assays. In Yang's work, as well as in the sensor reported by Liu *et al.* (2012), which used EIS only to characterize the layer formation, an increase in R_{ct} was reported upon PSA detection. Although the sensor fabrications were different, this was in contrast with what reported in this work both by Rodriguez *et al.* (2005) in an EIS application where a DNA aptamer was used to bind a lysozyme and by Jolly *et al.* (2015a), where a decrease in the R_{ct} was demonstrated. In the latter, a negative R_{ct} change was reported upon 300 nM of PSA at different ratios of aptamer/MCH. Conversely, a positive shift in R_{ct} was found using human serum albumin (HSA) indicating that different mechanisms occurred for the non-specific bindings. In order to further investigate such a phenomenon as well as the effect of the ratios, LOD and correlation with mass binding (QCM-D data), dose responses were studied and are now reported in this dissertation.

4.4 Sensor design, experimental set up and conditions

4.4.1 Sensor functionalisation

The principle of detection in the aptasensor is described in Figure 4.1. All the chemical reagents used for the experiments were of analytical grade and purchased from Sigma-Aldrich (UK) unless otherwise specified and ultrapure water (18.2 MΩ cm) was used for all the aqueous solutions (Millipore, USA). For the sensor modification, the DNA aptamer raised against PSA and developed by Savory *et al.* (2010) was thiolated and used in a mixture with MCH for the SAM formation. The use of MCH as a spacer molecule allows a better control of the lateral density of the DNA aptamer as well as to both reduce the non-specific interactions and regulate the charge transfer for EIS experiments (Keighley *et al.*, 2008). Gold substrates for both QCM-D and EIS measurements were then functionalised with a mixture of MCH and the thiolated DNA aptamer having sequence 5′-HS-$(CH_2)_6$-TTT TTA ATT AAA GCT CGC CAT CAA ATA GCT TT-3′. Since MCH is poorly miscible in aqueous solutions, it was initially diluted to reach the concentration of 100 mM in ethanol and successively in the measurement buffer to reach the desired concentration. Then the DNA aptamer was added to the prepared solution. In order to stabilise the initial DNA aptamer structure and enhance the efficiency towards the PSA binding, the DNA solution was heated for 10 min at 95 °C and rapidly cooled down to room temperature, as described by Savory *et al.* (2010), prior addition to the MCH solutions. The MCH/thiolated aptamer mixtures were prepared in such a way that the final thiol concentration was 100 μM. However, different aptamer to MCH fractions were tested, namely 1:50, 1:100, 1:200 and 1:500 molecular ratios.

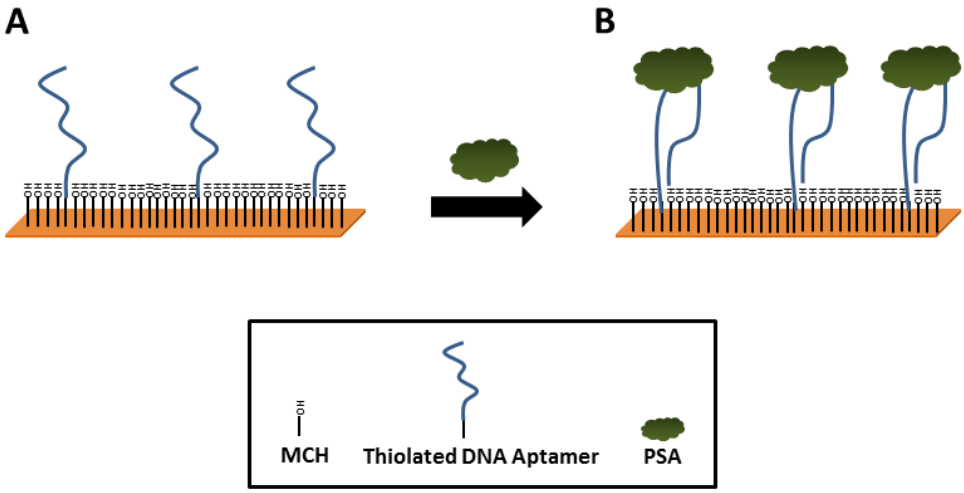

Figure 4.1Biosensor detection principle with representation of the electrode gold surface modifications before (A) and after (B) PSA binding.

Although gold−sulphur bonds happen relatively quickly (in few seconds or mimutes), the electrodes were left overnight reacting with the SAM sample (about 16 h) in order to foster the formation of a well-organised SAM structure. A good SAM ensures a more even accessibility of the ferri/ferrocyanide redox couples $[Fe(CN)_6]^{3-/4-}$ to the electrode surface, thereby yielding a more reliable EIS recording (Love *et al.*, 2005). After a 16-hour incubation period, a further backfilling step with MCH at the concentration of 1 mM provided further electrode coverage due to SAM reorganisation, coverage of pinholes in the initial SAM (see Figure 4.2 for a schematic representation), and lifting of any DNA lying flat on the surface due to electrostatic interactions.

Figure 4.2 A backfilling step with MCH after an initial SAM formation provided a better reorganisation of the SAM structure.

PSA from human seminal fluid in PBS, pH 7.4, 0.1% NaN_3, purity ≥98% by SDS-PAGE (product number 539831, from Merck Chemicals Ltd., UK) was then prepared in concentrations of 11, 22, 44, 89, 200, and 400 nM and used as a target.

4.4.2 EIS measurements

Impedance measurements were recorded in a 0.1 M phosphate buffer, 0.1 M KCl, 10 mM ferri/ferrocyanide $[Fe(CN)_6]^{3-/4-}$ (EIS measurement buffer), scanning 61 frequencies between 100 KHz and 0.1 Hz of the applied 10 mV a.c. voltage superimposed to the d.c. formal potential of the $[Fe(CN)_6]^{3-/4-}$ redox couple (-0.190 V versus Hg/Hg_2SO_4). The impedance of the electrochemical interface was modelled with the modified Randles equivalent circuit (Figure 2.16) where the capacitor that models the double layer has been replaced by a CPE in order to obtain a better estimation of the electrochemical double layer capacitance.

All the measurements were carried out in triplicate and the values reported in this study are the mean of replicates. Reported errors are standard deviations from the mean. EIS recordings were repeated every 30 min prior to the interaction with PSA until the signal was stable for two consecutive measurements. This stabilisation time was typically reached within 3 h.

4.4.3 Chronocoulometry measurements

The number of aptamer molecules per cm^2 was calculated by performing chronocoulometry with a μAUTOLAB III potentiostat in a three electrode system using a 10 mM Tris buffer pH 7.4, both in the absence and presence of 100 μM of hexaammineruthenium(III) chloride, $Ru(NH_3)_6^{3+}$. The potential was stepped from -0.3 V, where the potential was held for 200 ms, to -0.8 V versus $Hg/HgSO_4$ and held at this value for 500 ms, whilst the resulting currents were recorded. An example of chronocoulometry data is shown in Figure 4.3 where the values of charge are plotted versus $t^{1/2}$ and refers to an experiment performed on a mixed SAM made of DNA aptamer/MCH 100 μM in a ratio 1:200. By performing the measurements both in

absence and presence of $Ru(NH_3)_6^{3+}$ the difference of the intercepts at $t = 0$ of the two least square fits is used to derive the term $nFA\Gamma_O$ and therefore the DNA aptamer surface coverage from (2.37).

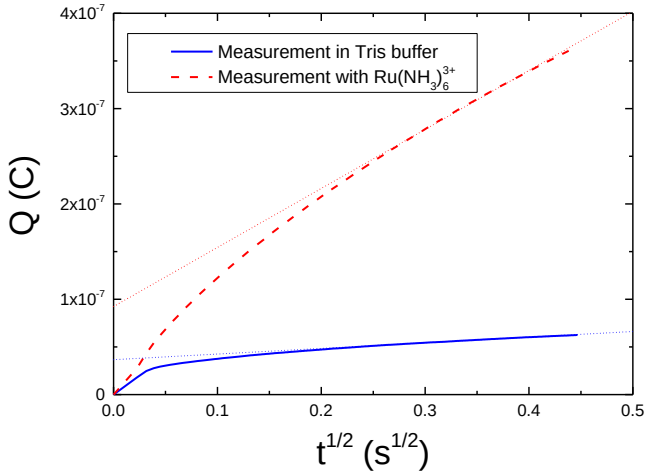

Figure 4.3 Chronocoulometry response for a gold electrode modified with a mixed SAM made of DNA aptamer/MCH 100 μM in a ratio 1:200. The dotted lines are linear fits used to obtain the intercepts for the determination of the DNA charge.

4.4.4 QCM-D measurements

Prior to modification and subsequent testing, AT-cut 5 MHz gold-coated quartz crystals (Q-Sense, Sweden) were cleaned by exposure to a solution of 5:1:1 of ultrapure water, hydrogen peroxide and ammonia preheated at 75 °C for 5 minutes. Cleaned crystals were rinsed successively with ultrapure water, ethanol and, again, ultrapure water and dried with nitrogen gas. A further step of 1 min UV/ozone exposure provided the final removal of organic contaminants before the crystals could be used for the QCM-D measurement. Quartz crystals were mounted in titanium chambers and used with an E4 QCM-D sensor system (Q-Sense, Sweden). The chamber temperature was set at 21.2 °C. DNA immobilisation, PSA binding and measurements were performed in the same buffer in which the aptamer was raised (Savory *et al.*, 2010): 10 mM Tris−HCl, 150 mM NaCl, 5 mM KCl, 5 mM $MgCl_2$, pH 7.4 (TBS buffer) with an ionic strength of 175 mM. In order to compare the amount of PSA bound on the quartz crystal for different aptamer/MCH fractions, three

concentrations of PSA were tested: 22, 89 and 200 nM. QCM-D analysis made use of an Ismatec peristaltic pump, set on a flow rate of 20.0 µl/min. After finding the best aptamer/MCH fraction, the biosensor detection was tested with dissolved PSA concentrations ranging between 0 and 400 nM. Sauerbrey and Voigt masses, which respectively give an approximate estimation of the dry and hydrated immobilised masses, were calculated using the frequency and dissipation values generated during protein titration. The frequency signals upon surface modifications are based on equation (2.58) whereas the estimation of the mass bound was obtained by integrating the dissipation values using the Voigt model (Voinova *et al.*, 1999; Dutta *et al.*, 2008; Höök *et al.*, 2001). The Voigt model was fitted using the QTools software (LOT-Oriel AG, Germany) by setting a film density of 1050 kg/m^3 and fluid viscosity of 0.001 kg/m s. From these bound mass responses, the dissociation constant of the PSA-immobilised aptamer complex was calculated.

4.5 Generation of EIS signals and strategy for the sensor optimisation

The negative charge of the DNA aptamer produces an electrostatic barrier to the negatively charged redox marker $[Fe(CN)_6]^{3-/4-}$, which hinders the charge transfer processes between the redox marker in solution and the conductive gold surface. The redox markers are responsible for generating the Faradaic current and therefore a reduction of their activity at the electrode interface would result in an increase in the resistance value. For this reason, a higher aptamer density on the electrode surface results in higher values of R_{ct}. According to the sensor fabrication as described in Figure 4.1, a change in the impedance of the system could be generated upon PSA binding. In particular, one would intuitively expect that the binding of the analyte to the aptamer (Figure 4.4A) produces an increase in the EIS signal (Figure 4.4B) as a consequence of the mass loading which can be recorded using the QCM-D (Figure 4.4C). Such an increase is expected as a result of a further blocking effect caused by PSA molecules towards the approach of the redox probes to the gold surface.

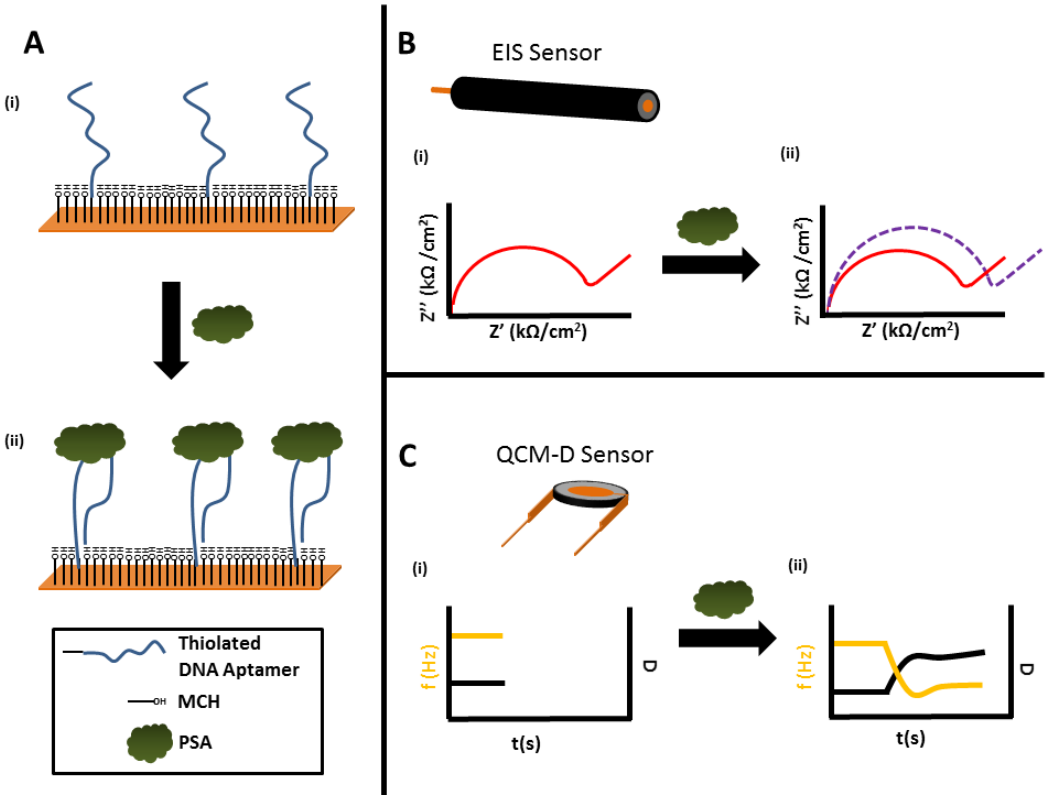

Figure 4.4 Correlation of the PSA detection process by means of EIS and QCM-D: (A) Biosensor detection principle with representation of the electrode gold surface; (b) EIS measurements showing a signal change in the complex impedance plot before (i) and after (ii) PSA binding; (c) QCM-D measurements showing frequency and dissipation responses before (i) and after (ii) PSA binding.

However, it must also be considered that when PSA binds to the aptamer, a conformational change of the DNA strand occurs with a consequent modification of the layer structure and possible screening of the DNA charges. Nevertheless, the conformational changes are not expected to affect the final QCM-D response as significantly, since the total value of mass bound (obtained by fitting the Voigt model) takes into account the alterations in the hydration level of the bound layer, induced by both the protein binding (prominent contribution) and DNA aptamer conformational changes.

It can be finally stated that the generation of the EIS signal is dependent upon a series of changes at the electrode interface. Preliminary results reported in a work led by Jolly *et al.* (2015a) showed that an aptamer/MCH ratio of 1:9 produced a minor response (0.76%) in ΔR_{ct} upon addition of 300 nM PSA. This suggested that the

sensitivity for the PSA detection could be enhanced by varying the surface conditions such as the aptamer density per unit area. In the same study, different ratios were tested using one PSA concentration (300 nM) and it was found that (i) such a system produced negative shifts in R_{ct} upon PSA binding and (ii) that such systems needed to be further optimised to maximise the EIS signal arising from the PSA binding.

Chronocoulometry of aptamer-modified electrodes was performed in order to estimate the DNA aptamer density on the electrode surface for different ratios of MCH/aptamer. The surface DNA distribution can play an important role in the sensor response (Keighley *et al.*, 2008). Chronocoulometry measurements also allowed one to correlate the LOD of EIS signals to the aptamer-to-MCH ratio used for the modification of the sensor. Nevertheless the highest probe density on the sensor surface does not always correspond to the maximum target binding. It might happen that the electrostatic repulsions of the aptamer probes can alter their structure and as a result their ability to effectively recognize the target. Successively, QCM-D has been used to find the aptamer/MCH fraction that maximises the PSA binding.

4.6 Effect of different Aptamer-to-MCH ratios

4.6.1Characterisation of the SAMs

The amount of DNA aptamer molecules bound to the gold electrodes could be obtained by performing chronocoulometry measurements upon the sensor functionalisation. The values of aptamer molecules per electrode area were calculated using the integrated Cottrell equation (2.35) and (2.37). Four different aptamer/MCH ratios were tested: 1:50, 1:100, 1:200 and 1:500. Chronocoulometry data (Figure 4.5) showed an aptamer density ranging from 0.86×10^{12} to 1.51×10^{12} molecules/cm^2 for increasing aptamer/MCH molar fractions in solution which are in agreement with values reported in previous studies on the optimisation of DNA-based sensors (Keighley *et al.*, 2008).

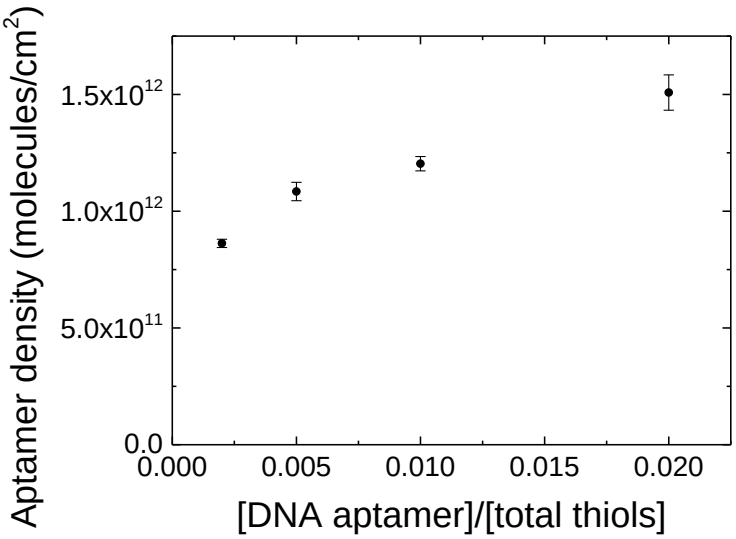

Figure 4.5 DNA aptamer molecule density distribution on the electrode surface vs. DNA aptamer/MCH molar fraction in solution.

These results were confirmed by EIS signals reported by Jolly (2016), which showed increasing values of initial R_{ct} as the ratio is decreased: 1059 ± 43 Ω, 1557 ± 50 Ω, 1634 ± 164 Ω and 1858 ± 161 Ω for 1:500, 1:200, 1:100 and 1:50 aptamer/MCH ratios (Figure 4.6), respectively, which also well correlates with DNA aptamer density from chronocoulometry data (inset Figure 4.6). The EIS results confirmed the correlation between the R_{ct} and the DNA aptamer density as anticipated in the section 4.5.

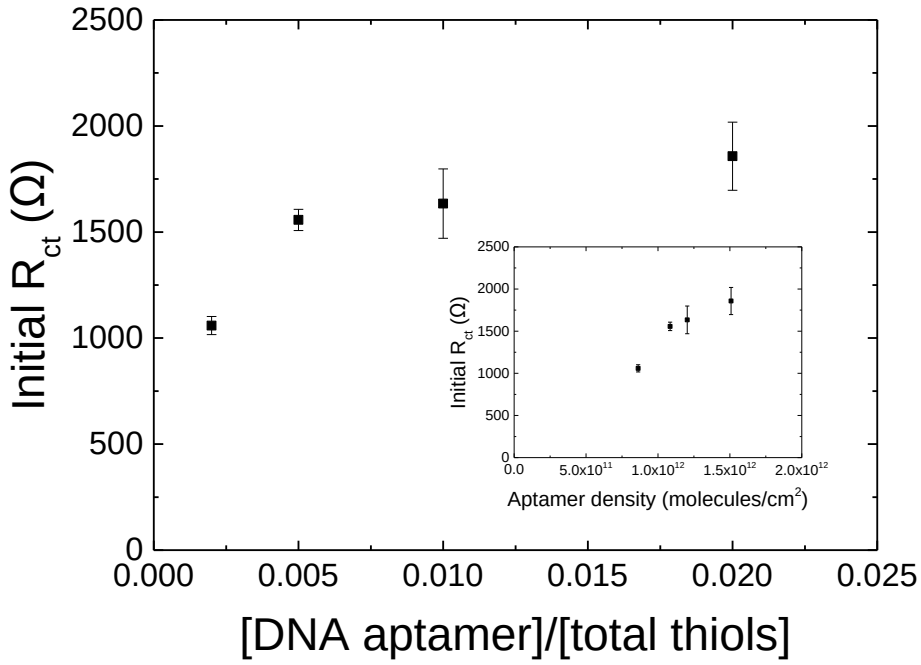

Figure 4.6 Initial R_{ct} for different DNA aptamer/MCH ratios. Reproduced from Jolly (2016).

Furthermore, preliminary QCM-D tests confirmed a different extent of mass binding upon SAM formation using different ratios. In such tests the electrode functionalisation performed with mixed SAMs of 1:9 and 1:200 aptamer/MCH ratio yielded QCM-D signal changes of 24.9 and 8.2 Hz, respectively, when the measurements were performed in an open chamber without flow (Figure 4.7). The difference in frequency shift, hence of bound mass, is consistent with the consideration that the thiolated DNA aptamer is longer and heavier than MCH. As a result a mixed SAM made of a higher content of thiolated aptamer (i.e. 1:9) causes a higher frequency shift than for samples modified with a smaller fraction of thiolated DNA aptamer (1:200).

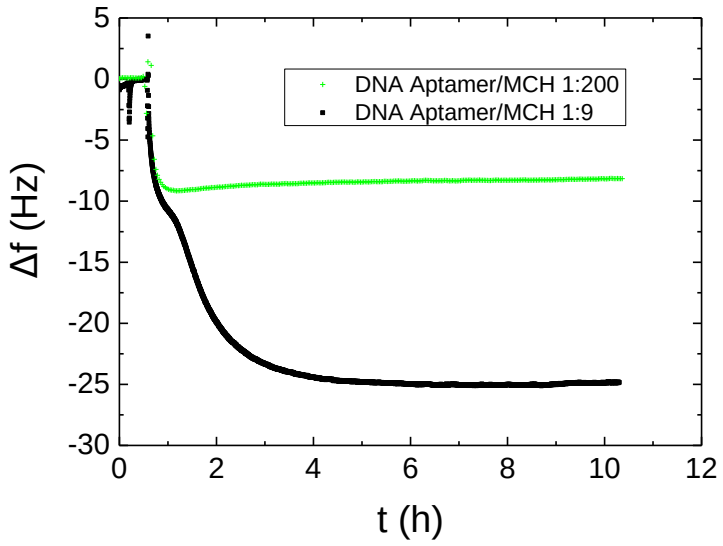

Figure 4.7 QCM-D frequency shift response obtained by functionalising two quartz crystals with mixed SAMs of DNA aptamer/MCH at the ratio of 1:200 and 1:9, respectively. The measurements were performed in an open chamber without flow.

4.6.2 Mass binding at different DNA aptamer/MCH fractions.

As introduced in Chapter 2, the response of a QCM instrument correlates the mass binding on a gold coated quartz crystal with the changes in the resonance frequency. In order to investigate the efficiency of the sensor in terms of target binding, QCM-D measurements were carried out on four different gold coated quartz crystals modified with aptamer/MCH in a ratio 1:500, 1:200, 1:100 and 1:50, respectively. The measurements were performed using three PSA solutions with concentrations of 22, 89 and 200 nM in a flow chamber using an Ismatec peristaltic pump set on a flow rate of 20.0 μl/min.

The four ratios were analysed by performing QCM-D measurements and obtaining the Voigt model responses. In Figure 4.8 the frequency responses (i.e. the frequency shift reading without applying any dissipation compensation factor) of the quartz crystals modified with different SAMs can be observed.

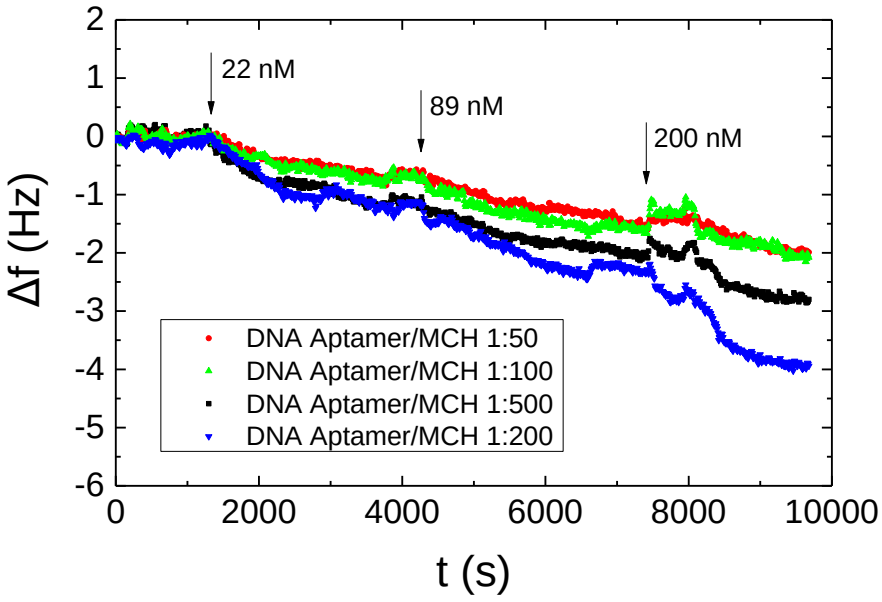

Figure 4.8 QCM-D frequency response of quartz crystals modified with different ratios of DNA aptamer/MCH. The measurements were performed in a flow chamber with a flow rate of 20.0 µl/min. The arrows indicate the PSA sample injection into the chambers.

Nevertheless, such signals are not accurately correlated to the mass binding. It is through the dissipation factor, in fact, that the hydration of the layers can be taken into account and a more accurate estimation of the amount of PSA bound can be given. This is an important point that can be exploited especially in case of protein modifications since they can entrap a high amount of water. In such cases, the frequency dampening of the quartz crystal can be reduced when a dissipative layer is present on the sensor. The oscillating signal was not able to completely sense the whole biological layer entrapped in the water. This can occur to such an extent that the effective protein mass could be largely underestimated if the solely Sauerbrey equation (therefore, ignoring the dissipation information) is used.

From the QCM-D signals, the four aptamer/MCH ratios showed different levels of hydration and of total PSA mass bound (Figure 4.9). Analysing the hydrated response, i.e. combining the dry-mass response with the dissipation signal, the electrode functionalised with an aptamer/MCH ratio of 1:200 exhibited the highest response in

terms of PSA binding, with an extent of pmoles/cm^2 129% higher than the electrode functionalised with a ratio of 1:50. However, a further decrease of the aptamer fraction (ratio 1:500) lowered the efficiency of the biosensor as shown in Figure 4.9. The trend obtained can be explained by considering the combination of two effects: the steric hindrance effect, which prevails for ratios up to 1:200, and the total number of aptamer molecules available for PSA targeting, which becomes more consistent for a lower DNA aptamer fraction. Furthermore, QCM-D revealed the difference in hydration amongst the four ratios. If we divide the amount of Voigt mass, i.e. the hydrated mass, by the Sauerbrey mass, i.e. the dry mass, we can have an indication of the correction factor due to the hydration level for each DNA aptamer/MCH fraction analysed. Respectively, 1:50, 1:100, 1:200 and 1:500 exhibited an average hydration level across the points shown in Figure 4.9 of 1.01, 0.80, 1.19 and 1.37. The values (very close or smaller than 1.00) obtained for the ratios 1:50 and 1:100 suggest that a higher DNA aptamer density can affect the rigidity of the biolayer. Moreover, the very packed probe layers can reduce the accessibility of the PSA protein (lower target binding obtained, as shown in Figure 4.8 and 4.9) as well as the access to solvent molecules carried with the flow of buffer. Therefore, a small amount of water remain entrapped in the biolayer using high densities of DNA aptamer. Increasing the space between the DNA aptamer molecules (ratios of 1:200 and 1:500), PSA molecules can bind more easily and entrapment of water molecules happens, as it is shown by the Voigt-to-Sauerbrey mass ratio larger than 1.00. The highest hydration level was achieved for the 1:500 ratio. However, as shown in Figure 4.9, the 1:500 ratio does not guarantee enough DNA aptamer coverage in order to ensure the maximum PSA binding to the sensor surface. In conclusion, the best compromise in terms of probe density coverage for obtaining the maximum binding is given by the ratio 1:200.

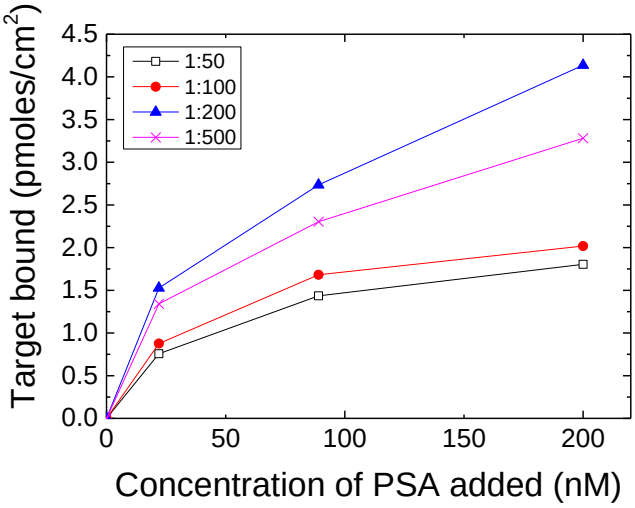

Figure 4.9 Hydrated mass QCM-D responses for measurements performed in a flow chamber with a flow rate of 20.0 µl/min for PSA binding at different DNA aptamer/MCH ratios. Measurements obtained from a single repetition.

4.6.3 EIS responses for different DNA aptamer/MCH ratios

Once the correlations between the different DNA aptamer/MCH ratios and the amount of PSA binding were found, the EIS responses were analysed using the same conditions. In order to test the EIS performance of the sensor, impedance measurements were compared for PSA concentrations between 300 fM and 300 nM using electrodes functionalised with different SAMs (Figure 4.10).

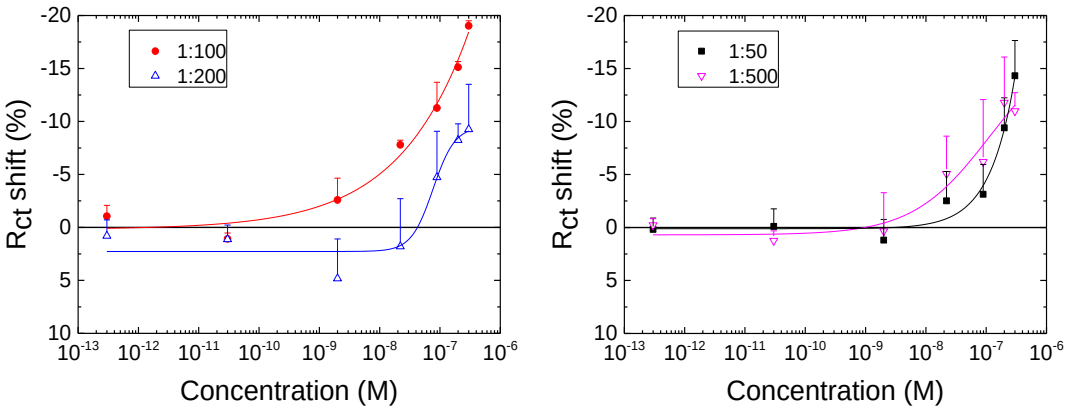

Figure 4.10 R_{ct} change upon incubation with PSA in different SAM over range of DNA aptamer/MCH concentration fraction. Standard deviations are reported only on one side for clarity. The lines, which serve as guides to the eye, are fits of the data to a Hill dose response equation: $y = y_0 + (y_{max} - y_0)\, c^n/(k^n + c^n)$ where c is the concentration. The EIS responses at 300 nM are in agreement with the data reported by Jolly (2016).

Measurements showed a general trend where the biosensor impedance moved towards smaller R_{ct} values upon increasing PSA, confirming the results reported by Jolly et al (2015a). With respect to the negative R_{ct} changes, it is worth highlighting that the isoelectric point of the PSA is between 6.9 and 7.2 (Zhang *et al.*, 1996). This means that PSA binding to the DNA aptamer is supposed to add a small increase in negative charge to the system when the biosensor is operated at pH equal to 7.4, which would increase the electrostatic barrier to the redox couple $[Fe(CN)_6]^{3-/4-}$, therefore increasing slightly R_{ct}. The folding of the DNA aptamer into its secondary structure upon PSA binding increases the density of charge closer to the surface and expands it to a larger geometrical area – factors which should also lead to an increase in R_{ct}. The presence of the bulky PSA molecules on the surface has an obstructing effect to the redox markers and would further hamper the electron transfer during EIS measurements as anticipated in the previous sections. However, decreases in R_{ct} upon PSA binding were recorded, as shown in Figure 4.10. One reasonable explanation can be attributed to the partial screening of the negative charge of the DNA aptamer by PSA binding, which lowers the electrostatic barrier to the redox markers, facilitating their approach to the sensor surface. The EIS response is in fact due to the combination of all the effects mentioned: a negative shift in R_{ct} is only observed when the screening of the DNA aptamer charge caused by the protein binding is the dominant effect. Such an effect was more relevant for high concentrations of PSA. In support of this theory, a couple of studies have been reported where the negative change in R_{ct} caused by the recognition of an antigen (Rodriguez *et al.*, 2005) including PSA (Jolly *et al.*, 2015a) by their specific aptamer is attributed to the screening of the negative charge of the DNA. This effect is reflected, in turn, on the interaction with the redox probes, which can more easily approach to the sensor surface because of the lowered electrostatic barrier.

The ΔR_{ct} *vs.* [PSA] curves roughly follow (the R^2values are 0.950, 0.968, 0.886 and 0.905 for the ratios 1:50, 1:100, 1:200 and 1:500, respectively) a Hill dose-response equation of the type:

$$y = y_0 + (y_{max} - y_0)\, c^n/(k^n + c^n) \quad (4.1)$$

where c is the concentration of the target. Therefore, no reliable values of the parameters can be extracted from the fits, presumably due to the complex dependencies of R_{ct} on the charge and mass of the biolayer.

The second important consideration that can be observed from the analysis of the EIS measurements, is that the maximum response from the impedimetric signal is obtained for an aptamer/MCH ratio of 1:100. In addition, for this ratio, the reproducibility of the EIS signals is also improved if we compare the responses from the sensors modified with different SAMs. This result showed that the maximum analyte binding (of which the value of ratio has been obtained by means of QCM-D) did not produce a maximum EIS response.

4.7 Optimisation of the PSA aptasensor

The EIS response at different PSA concentrations is reported in Figure 4.11 for the ratio 1:100.

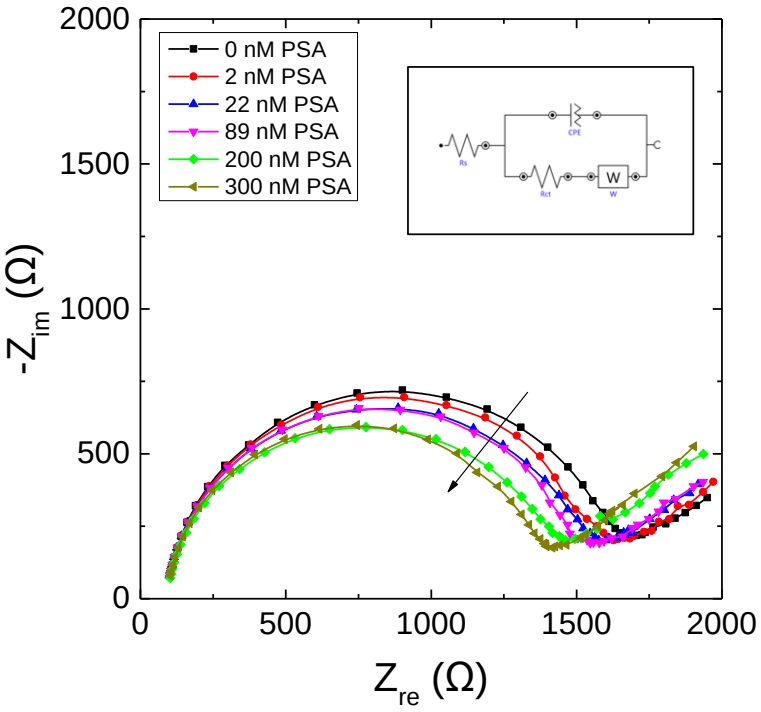

Figure 4.11 Complex impedance plot for different PSA concentrations using an aptamer/MCH ratio of 1:100. Inset: Randles equivalent circuit. R_s is the solution resistance, R_{ct} is the charge transfer resistance, CPE is the constant phase element and W is the Warburg element.

The EIS signal depends not only on the total mass bound on the surface (for which a maximum signal is obtained for a 1:200 ratio as seen by the QCM-D) but also on the screening of the DNA charge, which is expected to be higher for more densely packed DNA layers. The LODs obtained from the EIS data improve as one goes from a ratio of 1:500 towards 1:200 and 1:100, where the best value was obtained (<40 nM). However, for the 1:50 ratio, there is a significant increase in the LOD. Correlating the LODs obtained from the EIS responses for different aptamer densities (Figure 4.12), it can be seen that small changes of aptamer/thiols fraction can greatly affect the sensitivity towards the PSA detection: e.g. an increase in aptamer surface density from 1.2 to 1.5 × 10^{12} molecules/cm^2, leads to a significant increase in LOD. In particular, the LODs were 137 nM, 40 nM, 43 nM and 63 nM for the ratios 1:50, 1:100, 1:200 and 1:500, respectively.

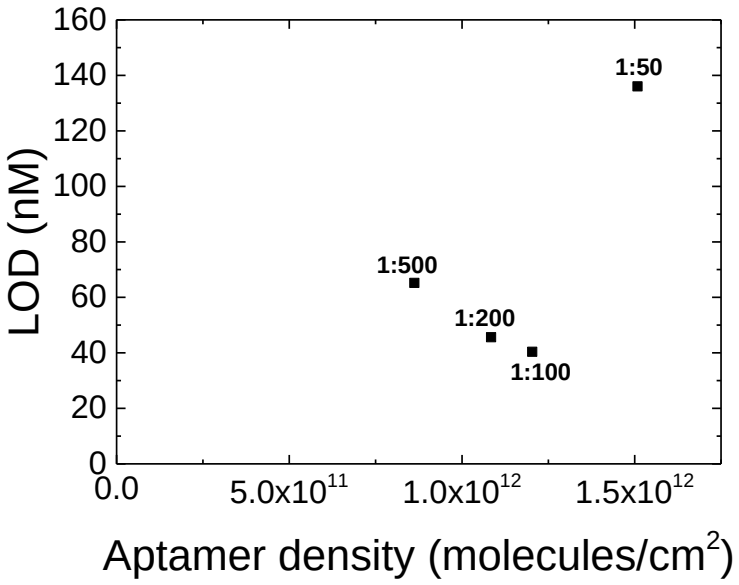

Figure 4.12 LODs obtained from the EIS responses for different DNA aptamer/MCH molar fraction vs. surface aptamer density.

Cases where the probe density is not monotonically followed (in mathematical terms) by the EIS sensor responses can be found elsewhere in literature such as in the work reported by Keighley (2008) where the R_{ct} response finds its maximum at a particular ratio in between the range 1:200 and 1:1 of [DNA]/[total thiol].

It is this fine balance between mass loading and charge effects that leads to a different optimal ratio for EIS measurements. In our previously reported work led by Jolly (2015a), the stability of the aptasensor with respect to repeated EIS measurements over time was also studied. It reported on the effect of changing types of buffer on the impedance signal as to make a clear point on reliable acquisition of data reflecting only binding of PSA to the aptasensor. It was demonstrated that changing the measurement solution altered the impedance value and only after a certain interval of time a new stable baseline could be reached.

As showed in Figure 4.9 from the QCM-D signals, the maximum target binding is achieved using a 1:200 aptamer/MCH ratio. In Figure 4.13 the QCM-D and the relative kinetic curves of frequency shift and dissipation changes are reported.

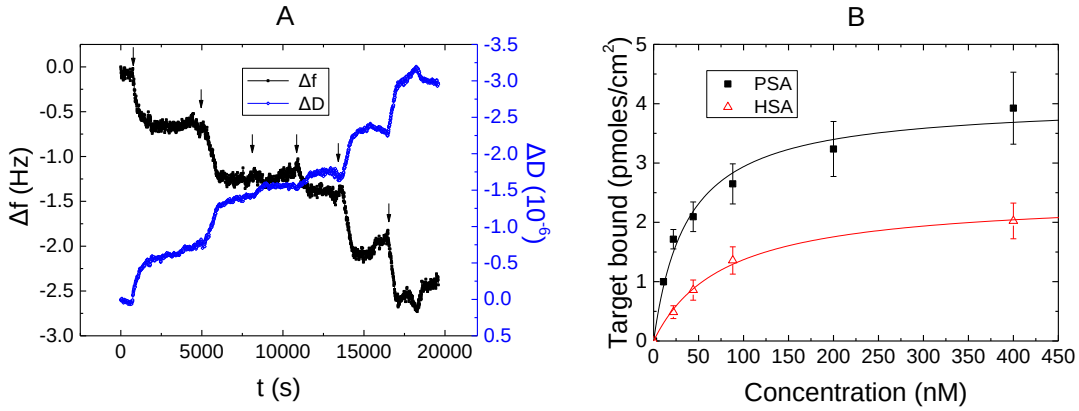

Figure 4.13(A) Kinetic curves of frequency and dissipation response upon increasing PSA additions in flow-condition. Arrows indicate additions of PSA; (B) Hydrated mass QCM-D response in a flow mode for PSA and HSA using an aptamer/MCH ratio of 1:200. Fitting is obtained by using a hyperbolic dose-response equation $y = y_{max}\, c/(K_d + c)$ *where c is the concentration and* K_d *the dissociation constant.* R^2 *is equal to 0.983 for PSA and 0.995 for HSA.*

It can be seen how increasing concentrations of PSA added to the chamber in flow conditions follow typical association curve responses. Moreover, PSA additions enhanced the viscoelastic properties of the biofilm as shown by the dissipation response. The dissipation signal allows estimating the mass of protein bound to the aptamer to be made with better accuracy. This can be extremely important in particular for low concentrations of PSA, where a correction as large as 10-fold was obtained when using the Voigt model with respect to the solely dry mass response. Figure 4.13B shows the hydrated QCM-D responses for PSA and HSA (used as a control) obtained with the aptamer/MCH ratio of 1:200. QCM-D data shows a hyperbolic dose response with a dissociation constant of K_d = 37 ± 6.3 nM for PSA.

Investigating the aptasensor by means of EIS, Jolly (2016) reported an increase in R_{ct} of 12 ± 6% upon 100 µM of HSA, which is the typical concentration of this protein in blood. However, unlike for PSA, the shift in R_{ct} deriving from non-specific binding of HSA is positive and, hence, easily distinguishable from PSA. In terms of EIS sensor performance, this is not a favourable feature for the biosensor. We cannot neglect the fact that using the biosensor in the presence of both proteins would result in a lower efficacy towards PSA detection. In complex matrix samples, such as blood,

non-specific interactions of other molecules represent one of the biggest challenges in biosensor development. However with respect to this study, keeping apart the development of a practical biosensor for PSA detection, there is a key consideration that is worth highlighting: the non-specific binding of proteins, in this case of HSA, occurs primarily within the MCH areas, yielding an increase in R_{ct} due to a blocking effect towards the redox couple. Moreover, the Voigt mass (reported in Figure 4.13B) differs less than 1 % from the Sauerbrey mass when HSA is detected. This is greatly different from what is obtained for PSA where a Voigt mass up to 10-fold was obtained with respect to the Sauerbrey mass. This indicates that HSA rigidly binds onto the molecular layer, not allowing as much entrapment of water as it happens for PSA.

4.8 Conclusions

In this study, we investigated strategies for the optimisation of an EIS aptamer-based sensor. We used a PSA-specific aptamer as a case study and monitored the total PSA mass bound by varying the binding conditions and recording QCM-D data. QCM-D results confirmed the importance of DNA surface coverage optimisation for efficient aptamer-protein binding. In particular, we found that a ratio 1:200 of aptamer/MCH provides the maximum PSA binding. However, EIS data demonstrated that a higher DNA aptamer surface density (obtained for a 1:100 ratio) is required for an optimal impedimetric signal. A negative R_{ct} signal change was recorded upon targeting the DNA aptamer as a result of the screening of the aptamer charge by bound PSA. Impedimetric measurements in aptasensors depend on the balance between different factors such as the antigen-binding bulk effect, surface charge, and DNA conformational changes happening upon target binding. Therefore, the DNA aptamer surface density, for which maximum antigen binding occurs, is not necessarily the optimal surface density for EIS measurements. Moreover in this study, we have shown a decrease in the ΔR_{ct} signal upon targeting the DNA aptamer. The decrease in R_{ct} cannot, however, be generalised for any aptamer-based sensor as the EIS signal is not only generated by the obstructing effect induced by the target binding but also by the charge and conformational redistributions that happen on the sensor surface. A

direct consequence is that a maximum analyte binding, as here demonstrated, not always corresponds to a maximum signal response for an EIS sensor. The results of this study could then be applied to future label-free EIS sensors.

As a side note, it can also be concluded that although aptamers have great potential towards the development of biosensors, aptasensors require a careful design in order to provide an acceptable binding efficiency. In the last decade, a large effort has been put into developing aptasensors, however, antibody-based sensors have not been replaced yet by newer technologies in real applications.

Finally, in terms of sensor performance a K_d value of 37 nM was found for the DNA aptamer towards its PSA target.

References

Acevedo, B., Perera, Y., Ruiz, M., Rojas, G., Benítez, J., Ayala, M., & Gavilondo, J. (2002). Development and validation of a quantitative ELISA for the measurement of PSA concentration. *Clinica Chimica Acta*, 317(1), 55-63.

Albrecht, S., Brandl, H., Steinke, M., & Freidt, T. (1994). Chemiluminescent enzyme immunoassay of prostate-specific antigen based on indoxyl phosphate substrate. *Clinical Chemistry*, 40(10), 1970-1971.

Arya, S. K., & Bhansali, S. (2012). Anti-prostate specific antigen (anti-PSA) modified interdigitated microelectrode-based impedimetric biosensor for PSA detection. *Biosensors Journal*, 1, H110601.

Basch, E., Oliver, T. K., Vickers, A., Thompson, I., Kantoff, P., Parnes, H., Loblaw, D. A., Williams, J., & Nam, R. K. (2012). Screening for prostate cancer with prostate-specific antigen testing: American Society of Clinical Oncology provisional clinical opinion. *Journal of Clinical Oncology*, 30(24), 3020-3025.

Carter, H. B., Pearson, J. D., Metter, E. J., Brant, L. J., Chan, D. W., Andres, R., Fozard, J. L., & Walsh, P. C. (1992). Longitudinal evaluation of prostate-specific antigen levels in men with and without prostate disease. *Journal of the America Medical Association*, 267(16), 2215-2220.

Cha, T., Cho, S., Kim, Y. T., & Lee, J. H. (2014). Rapid aptasensor capable of simply diagnosing prostate cancer. *Biosensors and Bioelectronics*, 62, 31-37.

Chen, Z., Lei, Y., Chen, X., Wang, Z., & Liu, J. (2012). An aptamer based resonance light scattering assay of prostate specific antigen. *Biosensors and Bioelectronics*, 36(1), 35-40.

Chiriacò, M. S., Primiceri, E., Montanaro, A., de Feo, F., Leone, L., Rinaldi, R., & Maruccio, G. (2013). On-chip screening for prostate cancer: an EIS microfluidic platform for contemporary detection of free and total PSA. *Analyst*, 138(18), 5404-5410.

Choi, H. K., & Lee, J. H. (2013). Role of magnetic Fe 3 O 4 graphene oxide in chemiluminescent aptasensors capable of sensing tumor markers in human serum. *Analytical Methods*, 5(24), 6964-6968.

Dutta, A. K., Nayak, A., & Belfort, G. (2008). Viscoelastic properties of adsorbed and cross-linked polypeptide and protein layers at a solid–liquid interface. *Journal of Colloid and Interface Science*, 324(1), 55-60.

Ferlay, J., Soerjomataram, I., Ervik, M., Dikshit, R., Eser, S., Mathers, C., Rebelo, M., Parkin, D. M., Forman, D., & Bray, F. (2013). GLOBOCAN 2012 v1. 0, cancer incidence and mortality worldwide: IARC CancerBase No. 11 [internet]. International Agency for Research on Cancer, Lyon. globocan. iarc. fr (accessed 10 October 2014).

Formisano, N., Jolly, P., Bhalla, N., Cromhout, M., Flanagan, S. P., Fogel, R., Limson, J. L., & Estrela, P. (2015). Optimisation of an electrochemical impedance spectroscopy aptasensor by exploiting quartz crystal microbalance with dissipation signals. *Sensors and Actuators B: Chemical*, 220, 369-375.

Gilgunn, S., Conroy, P. J., Saldova, R., Rudd, P. M., & O'Kennedy, R. J. (2013). Aberrant PSA glycosylation—a sweet predictor of prostate cancer. *Nature Reviews Urology*, 10(2), 99-107.

Hianik, T., & Wang, J. (2009). Electrochemical aptasensors–recent achievements and perspectives. *Electroanalysis*, 21(11), 1223-1235.

Höök, F., Kasemo, B., Nylander, T., Fant, C., Sott, K., & Elwing, H. (2001). Variations in coupled water, viscoelastic properties, and film thickness of a Mefp-1 protein film during adsorption and cross-linking: a quartz crystal microbalance with dissipation monitoring, ellipsometry, and surface plasmon resonance study. *Analytical Chemistry*, 73(24), 5796-5804.

Jeong, S., Han, S. R., Lee, Y. J., Kim, J. H., & Lee, S. W. (2010). Identification of RNA aptamer specific to mutant KRAS protein. *Oligonucleotides*, 20(3), 155-161.

Jolly, P. (2016) DNA based development of electrochemical sensor for detection of prostate cancer biomarkers (Doctoral dissertation, University of Bath).

Jolly, P., Formisano, N., Tkáč, J., Kasák, P., Frost, C. G., & Estrela, P. (2015a). Label-free impedimetric aptasensor with antifouling surface chemistry: A prostate specific antigen case study. *Sensors and Actuators B: Chemical*, 209, 306-312.

Jolly, P., Formisano, N., & Estrela, P. (2015b). DNA aptamer-based detection of prostate cancer. *Chemical Papers*, 69(1), 77-89.

Keighley, S. D. (2008). Label-free detection of nucleic acids by their intrinsic molecular charge (Doctoral dissertation, University of Cambridge).

Keighley, S. D., Li, P., Estrela, P., & Migliorato, P. (2008). Optimisation of DNA immobilisation on gold electrodes for label-free detection by electrochemical impedance spectroscopy. *Biosensors and Bioelectronics*, 23(8), 1291-1297.

Lilja, H., Ulmert, D., & Vickers, A. J. (2008). Prostate-specific antigen and prostate cancer: prediction, detection and monitoring. *Nature Reviews Cancer*, 8(4), 268-278.

Liu, B., Lu, L., Hua, E., Jiang, S., & Xie, G. (2012). Detection of the human prostate-specific antigen using an aptasensor with gold nanoparticles encapsulated by graphitized mesoporous carbon. *Microchimica Acta*, 178(1-2), 163-170.

Love, J. C., Estroff, L. A., Kriebel, J. K., Nuzzo, R. G., & Whitesides, G. M. (2005). Self-assembled monolayers of thiolates on metals as a form of nanotechnology. *Chemical Reviews*, 105(4), 1103-1170.

Ma, W., Yin, H., Xu, L., Wu, X., Kuang, H., Wang, L., & Xu, C. (2014). Ultrasensitive aptamer-based SERS detection of PSAs by heterogeneous satellite nanoassemblies. *Chemical Communications*, 50(68), 9737-9740.

O'Sullivan, C. K. (2006). Aptamer conformational switch as sensitive electrochemical biosensor for potassium ion recognition. *Chemical Communications*, (32), 3432-3434.

Okuno, J., Maehashi, K., Kerman, K., Takamura, Y., Matsumoto, K., & Tamiya, E. (2007). Label-free immunosensor for prostate-specific antigen based on single-walled carbon nanotube array-modified microelectrodes. *Biosensors and Bioelectronics*, 22(9), 2377-2381.

Panini, N. V., Messina, G. A., Salinas, E., Fernández, H., & Raba, J. (2008). Integrated microfluidic systems with an immunosensor modified with carbon nanotubes for detection of prostate specific antigen (PSA) in human serum samples. *Biosensors and Bioelectronics*, 23(7), 1145-1151.

Pestourie, C., Cerchia, L., Gombert, K., Aissouni, Y., Boulay, J., Franciscis, V. D., Libri, D., Tavitian, B., & Ducongé, F. (2006). Comparison of different strategies to select aptamers against a transmembrane protein target. *Oligonucleotides*, 16(4), 323-335.

Rodriguez, M. C., Kawde, A. N., & Wang, J. (2005). Aptamer biosensor for label-free impedance spectroscopy detection of proteins based on recognition-induced switching of the surface charge. *Chemical Communications*, (34), 4267-4269.

Savory, N., Abe, K., Sode, K., & Ikebukuro, K. (2010). Selection of DNA aptamer against prostate specific antigen using a genetic algorithm and application to sensing. *Biosensors and Bioelectronics*, 26(4), 1386-1391.

Seto, Y., Iba, T., & Abe, K. (2001). Development of ultra-high sensitivity bioluminescent enzyme immunoassay for prostate-specific antigen (PSA) using firefly luciferase. *Luminescence*, 16(4), 285-290.

Voinova, M. V., Rodahl, M., Jonson, M., & Kasemo, B. (1999). Viscoelastic acoustic response of layered polymer films at fluid-solid interfaces: continuum mechanics approach. *Physica Scripta*, 59(5), 391.

Wee, K. W., Kang, G. Y., Park, J., Kang, J. Y., Yoon, D. S., Park, J. H., & Kim, T. S. (2005). Novel electrical detection of label-free disease marker proteins using piezoresistive self-sensing micro-cantilevers. *Biosensors and Bioelectronics*, 20(10), 1932-1938.

Yang, Z., Kasprzyk-Hordern, B., Goggins, S., Frost, C. G., & Estrela, P. (2015). A novel immobilisation strategy for electrochemical detection of cancer biomarkers: DNA-directed immobilisation of aptamer sensors for sensitive detection of prostate specific antigens. *Analyst*, 140(8), 2628-2633.

Zhang, W. M., Leinonen, J., Kalkkinen, N., Dowell, B., & Stenman, U. H. (1995). Purification and characterisation of different molecular forms of prostate-specific antigen in human seminal fluid. *Clinical Chemistry*, 41(11), 1567-1573.

Chapter 5. Immobilisation of signal probes for improving EIS detection: multimodal protein phosphorylation detection as a case study

The work presented in this Chapter has been partly published (Formisano *et al.*, 2015).

5.1 Introduction

In this Chapter a strategy that makes use of signal probes for EIS detection is reported. This can be considered as an "indirect labelling" assay since the label used for enhancing the measurement signals is attached on the target after its recognition with the probe. Therefore, contrarily to the direct labelling strategies, this method does not affect the binding properties of the target towards its probe. For this reason, it is important to clarify that the strategy here used is still considered as label-free although reagents for increasing the sensitivity of the assay are used.

Introduction sections of countless published works on EIS sensors stress the importance of impedimetric sensors as a label-free technique. In the course of this dissertation, instead, a critical view has been used on both the advantages and drawbacks of label-free techniques as well as EIS itself as a detection technique. The advantages of EIS as a label-free technique have already been reported in the previous sections and include the reduced times of assay implementation since often secondary probes or other reagents are not used for obtaining reliable signals. On the other hand,

the aspects that lead to the study of an indirect labelling process for an EIS sensor can be summarised as: firstly pure label-free techniques can lack both selectivity and sensitivity with respect to other strategies. This is due in some cases to the lack of any amplification or supplementary conditioning that enables easier signal generation resulting in a lower sensitivity (see Chapter 3). Secondly, in electrochemical systems modifications of the electrochemical double layer equilibrium by means of mechanisms not related to the binding of the analyte are not rare. Such perturbations could produce false signals that can mask the measurement arising from the capture of the target. As a result, in order to gather a reliable signal and to not let external factors generate false positives, the measurement set up must be accurately controlled (Daniels and Pourmand, 2007). This is often a necessary but not sufficient condition to ensure the repeatability in EIS measurements. It is not surprising that EIS measurements on similar systems produced, at times, completely contradictory results (in the next sections, references will be given with examples found in literature). On the other hand, the use of signal enhancers can enable multimodal detection increasing the reliability of the detection, as it will be demonstrated in this study.

As a case system for demonstrating the points here mentioned, detection of protein phosphorylation has been analysed where ferrocene-crowned gold nanoparticles (GNP-Fc) enabled multimodal sensing exploiting both electrochemical and plasmonic techniques on a linear array of electrodes in a flow cell. Protein phosphorylation could be detected in real time by an OCP set up by Wong (2016) as well as by DPV, EIS and LSPR. Different electrochemical techniques can be used for fast, miniaturised biosensing systems, with each technique providing different information, which can then be correlated to a certain concentration of analyte. Often more than one technique is used to validate the biosensor signal or provide complementary information on the biological recognition system (e.g. kinetics and concentration). A few reports have integrated different techniques on the same measurement system in order to look at different properties of an interaction or validate the detection of an analyte (She *et al.*, 2015; Bhalla *et al.*, 2015a). Such integrated systems open the doors towards generic biosensors that can be used for a range of applications where the user selects which

techniques to use according to the properties of the biomolecule to be measured or the information required.

In summary, in this Chapter the advantage that can be brought by labelling processes is introduced as well as a new multimodal approach for protein phosphorylation detection applicable in drug discovery application is reported.

5.2 Protein phosphorylation

5.2.1 Phosphorylation reaction and its consequences

Protein phosphorylation refers to the process through which a protein gains phosphate groups (PO_4^{3-}). It is one of the main post translational modifications of proteins and such process is responsible for changing the biological behaviour of the proteins which can result in either advantageous or unfavourable for the cell activity. As a result, many cellular mechanisms can be activated, inhibited or altered to a certain extent upon protein phosphorylation (Cohen, 2002). It is evident how this process plays an important role in the regulation of various cellular functions, for instance cell differentiation, cell proliferation and glucose metabolism, to mention a few.

Phosphorylation is modulated by enzymes called kinases. Kinases enable transfer of phosphate groups from a phosphate donor such as adenosine-triphosphate (ATP) to the serine, threonine, tyrosine or histidine amino-acid residues of a protein (Caballero *et al.*, 2012). The transfer of phosphate groups from ATP induces covalent attachments of phosphate groups to the protein and a modification of the cells involved in the process. In such reaction, ATP, which is the source of phosphate groups, transforms into adenosine-diphosphate (ADP) (Bantscheff *et al.*, 2012). Figure 5.1 shows the mechanism of protein phosphorylation. In this process, the truncation of the terminal PO_3^{2-} group of the ATP is aided by Mg^{2+}. The PO_3^{2-} group is eventually translocated to the OH termination of one of the amino acids available for the phosphorylation (serine, threonine, tyrosine and histidine). Here, a kinase is responsible of initiating the phosphorylation by inducing the proton transfer that let the oxygen bind the PO_3^{2-}

moiety. As a result the protein attaches the PO_3^{2-} group and the protein becomes phosphorylated (Figure 5.1).

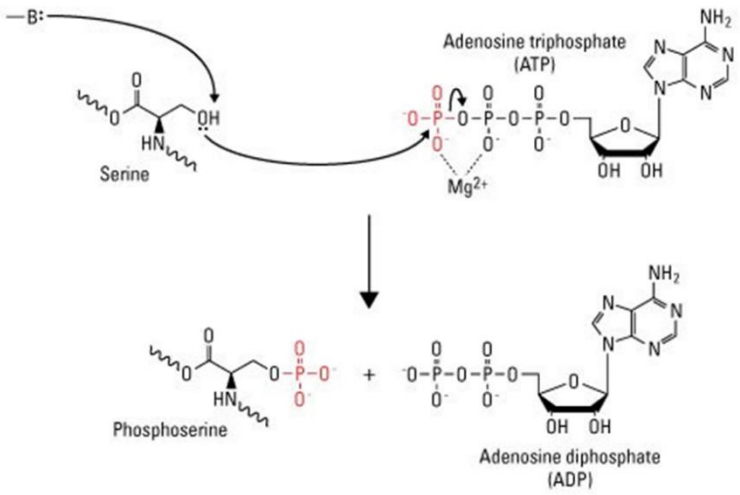

Figure 5.1 Mechanism of the protein phosphorylation reaction. A kinase activator (-B:) induces a proton transfer at the OH amino acid termination of a protein. Meanwhile the magnesium facilitates the separation of a PO_3^{2-} group form the ATP which will be eventually be available to attach on the protein. The reaction results in the phosphorylation of the protein and in the conversion of ATP to ADP. Reproduced from https://www.thermofisher.com/uk/en/home/life-science/protein-biology/protein-biology-learning-center/protein-biology-resource-library/pierce-protein-methods/phosphorylation.html (last access on 16/09/2015).

Since such a process is one of the most important post-transcription modifications in all of the normal biological functions of a human, an abnormal phosphorylation can biologically modify the proteins and cells behaviour inducing a wide number of diseases. An example of abnormal protein phosphorylation that induces cells transformation is represented in Figure 5.2.

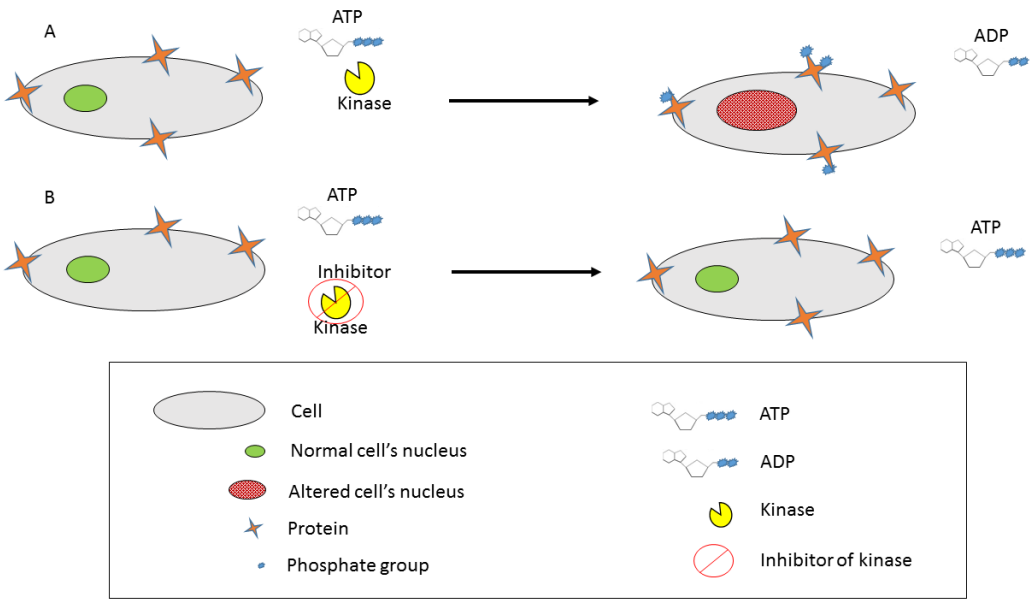

Figure 5.2 Principle of protein phosphorylation process. A) The transfer of phosphate groups from ATP to the proteins of a cell driven by the kinase's activity induces damage to the cell. B) No phosphorylation in the presence of inhibitor occurs with no consequent changes in the morphological and functional structure of the cell involved.

Therefore, an altered phosphorylation process is associated with several conditions such as cancer, diabetes, neural and autoimmune diseases and over 400 illnesses are today linked either directly or indirectly to the activity of protein kinases (Cohen and Alessi, 2013; Jänne *et al.*, 2012; Parang and Sun, 2010; Cohen, 2002). Nowadays, the discovery of new kinase inhibitors is one of the most pursued research fields for developing drugs for cancer treatment (Zhang *et al.*, 2009).

5.2.2 Standard and newer developed techniques for protein phosphorylation detection

From what has been introduced so far, it is evident that one way of regulating an altered phosphorylation process of proteins is to inhibit the kinase activity. Such strategy can be implemented by means of a class of molecules called "inhibitors of kinases" which prevents the protein phosphorylation and hence can act as drugs to treat phosphorylation related disorders. Inhibitors of kinases prevent or slow down phosphorylation by binding to the extracellular domain of kinase and are currently

used as drugs in chemotherapy and for other diseases treatments. Studies on the phosphorylation of proteins have been explored by a number of researchers to develop biosensors for drug discovery applications. To address the need of kinase inhibitors, both researchers in academia and industry have extensively worked on the development of tools to detect phosphorylation of proteins that are capable of screening inhibitors of kinase. However, the current kinase inhibitor drug market is very premature with less than 30 protein kinase inhibitors approved by the United States Food and Drug Administration (FDA) until 2014 (Roskoski Jr., 2015). The discovery of new drugs in this field is hampered at times by the time-consuming, cost-inefficient, and laborious detection techniques used in pharmaceutics to understand the kinase activity. Currently, western blot (Sawasdikosol, 2010; Sugimoto and Hashimoto, 2006; MacKeigan *et al.*, 2005; Xu *et al.*, 2004) and ELISA (Delbroek *et al.*, 2013; Kee *et al.*, 2013, Diamandi *et al.*, 2000) are the most used technique by pharmaceutical researchers to detect kinase activity. Western blot is a relatively cheap technique but involves laborious preparation of gels through which proteins of interest are separated in a time consuming manner by electrophoresis (the whole assay can last up to 3 days). A western blot assay eventually requires a secondary antibody and the detection is obtained by means of the chemo-luminescent signal that it emanates. Apart from the time-expensive process that it necessitates, western blot does not allow to obtain information about the kinetic of phosphorylation reactions.

ELISA can allow a better parallel screening inhibitors of kinases exploiting the multi-well plate platform. An additional advantage with respect to western blot is that the quantification of the protein phosphorylation can be automatically obtained by means of calibration standards. The ELISA's response is a colourimetric- or fluorometric-based signal obtained using secondary labelled antibodies that attach to the phosphorylated proteins. Drawbacks of ELISA methods include false positive arising from non-specific binding of the secondary antibody and the limited ability of monitoring the reaction kinetics as the technique does not allow real time recordings.

Another technique which is currently used by researchers is autoradiography through which an isotope's activity on a modified surface is monitored. This implies labelling of phosphoproteins with radioactive compounds (Laufer *et al.*, 2005; Yan *et al.*, 1998).

In particular, the ATP terminal phosphate group that is transferred to the protein in the phosphorylation reaction (also called γ-phosphoryl group) is tagged with a radioactive isotopes which eventually generates the autoradiography signal. The radioactivity allows the quantification of levels of phosphorylation however, potential damages at the proteins can occur affecting the influence of the kinase inhibitor on the protein itself. Moreover, while this technique provides high sensitivity, it is not environmental or user friendly since an autoradiography assay involves potential harmful reagents and produces hazardous wastes.

Electrochemical strategies used for protein phosphorylation detection are reported in the next section. Other emerging and/or less established techniques on which protein phosphorylation detection has been based can be mentioned: QCM (Morick *et al.*, 2013; Xu *et al.*, 2012; Kinoshita *et al.*, 2012; Furusawa *et al.*, 2012), mass spectroscopy (Chen *et al.*, 2007), infrared spectroscopy (Goldsztein *et al.*, 2010), contact angle (Wieckowska *et al.*, 2008; Wilner *et al.*, 2008), plasmonic biosensors (Bhalla *et al.*, 2015a; Bhalla *et al.*, 2015b; Nordin *et al.*, 2005), quantum dots (Shiosaki *et al.*, 2013; Wang *et al.*, 2010; Freeman *et al.*, 2010), field-effect devices (Bhalla *et al.*, 2015a; Bhalla *et al.*, 2015b; Freeman *et al.*, 2007; Lindsay, 2012;), cantilevers (Kwon *et al.*, 2007).

5.2.3 Electrochemical protein phosphorylation assays: main features and limitations

Currently an increasing number of studies on electrochemical biosensors for protein phosphorylation assays or kinase inhibitor discovery can be found. Upon phosphorylation there is a negative charge imparted on the proteins by the addition of phosphate groups. This is one of the most important parameters of the phosphorylation reaction that is exploited by electrochemists to quantify the phosphorylation event. Figure 5.3 shows a general phosphorylation reaction occurring on a sensor surface that could be monitored in a typical electrochemical experiment. In such a system, the proteins are immobilised on the electrode. The electrode is then exposed to kinase, kinase activator and ATP to initiate phosphorylation of proteins.

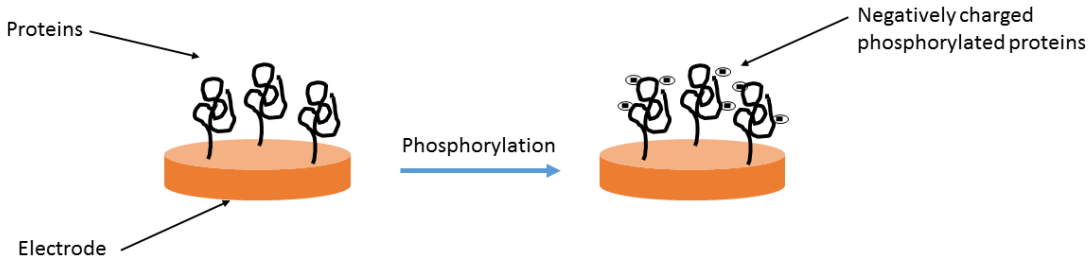

Figure 5.3 Protein monolayer transformation after phosphorylation reaction.

Although some sensors have shown high levels of sensitivity, one drawback of this type of system is that it has always a probability to non-specifically attach either kinase, ATP or other activating/inhibiting molecules under test. This could lead to a very non-reproducible systems for electrochemical detection. Evidence of the non-reproducibility can be found in the contradictory results of the EIS sensors reported in literature for the detection of phosphorylation.

Earlier studies on Faradaic measurements of the kinase activity using EIS revealed an increase in the charge transfer resistance of the electrode upon phosphorylation of proteins (Wilner *et al.*, 2008; Miao *et al.*, 2011; Chen *et al.*, 2013). The authors claim that the negative charge upon phosphorylation of proteins repels the negatively charged redox marker in the electrolyte. Dose and time dependent kinetics of the phosphorylation was successfully achieved by the authors. More recent accounts (Snir *et al.*, 2011; Snir *et al.*, 2015) report a decrease in the electron transfer resistance upon phosphorylation of oligopeptides. Although authors mention that the decrease in electron transfer resistance was unexpected, they attribute these changes to the reduction in the packing density of the peptide monolayer. Moreover, these reports also demonstrated dose response with increasing concentration of kinase that showed a clear trend of decrease in the resistance with increase in kinase activity. While there are opposite results for the system, nevertheless the authors can clearly differentiate between phosphorylated and unphosphorylated samples that allows them to assert the use of their biosensor for screening inhibitors of kinases.

Interestingly, all the above mentioned electrochemical sensors either do not report the EIS signals upon the use of kinase inhibitors (Wilner *et al.*, 2008; Snir *et al.*, 2015, Snir *et al.*, 2011) or a second technique other than EIS is used to confirm the activity of the inhibitors - for instance electrochemiluminescence (Chen *et al.*, 2013) or chronocoulometry (Miao *et al.*, 2011). This questions the reliability and robustness of an EIS system for such biosensing applications.

In light of the results reported, it is not surprising to find other biosensors for protein phosphorylation detection using various electrochemical techniques exploiting labels such as gold nanoparticles (Kerman and Kraatz, 2009; Kerman *et al.*, 2007) or a biotin-streptavidin-GNP complex (Wang *et al.*, 2011) to enhance the selectivity of the assay.

One way to address the problem of the reliability of the EIS measurements is increasing the specificity of the biosensor. Based on the findings of the reported EIS studies, detection of the phosphorylation of proteins presented an exploratory platform where the selectivity of EIS biosensors must be optimised. Therefore the work described in this chapter focuses on highly specific detection of phosphorylated proteins using electrochemical techniques.

5.3 Preliminary EIS study on protein phosphorylation detection

The system used for the measurements consisted of a gold electrode modified with a mixed SAM made of MUA and MCH in a ratio 1:9. The assay protocol for phosphorylation detection on gold surfaces was optimised by Bhalla and co-workers (2015b).

Preliminary Faradaic measurements did not produce a time-dependent stable baseline for EIS experiments. Measurements performed using 5 mM ferri/ferrocyanide $[Fe(CN)_6]^{3-/4-}$ initially in 10 mM Tris base pH 7.4 (with addition of 6 mM NaCl and 0.4 mM $MgCl_2$), and successively in 0.1 M phosphate buffer (with addition of 0.1 M KCl) generated a variability from 11 to 94 % of signal change when 2 measurements of the same sample were performed at a time interval of 30 minutes upon no addition of any binding molecule. The stability did not improve when keeping the electrodes

up to 2 days sealed in plastic tubes with the measurement solution. The large variability of the EIS signal did not allow to carry out the phosphorylation of the proteins bound on the electrode surface since a comparative analysis could not be effectively accomplished. The reason of the instability could be due to the very flexible orientation of the proteins used for the phosphorylation assay on the SAM which lead to a large variability of the obstructing effect towards the redox markers in solution that contribute to the EIS signal.

A different approach was then used exploiting the non-Faradaic measurements thus avoiding the use of the redox markers. This approach significantly improved the stability of the system probably due to the lack of $[Fe(CN)_6]^{3-/4-}$ redox molecules that could interact with the exposed charges of the proteins and a valid baseline could be obtained (the capacitance shift was $\leq$ 1.5 % over repeated measurements spaced out by 30 minutes intervals). However, the capacitance changes upon phosphorylation were smaller than 3.5 % with a large standard deviation (Figure 5.4)

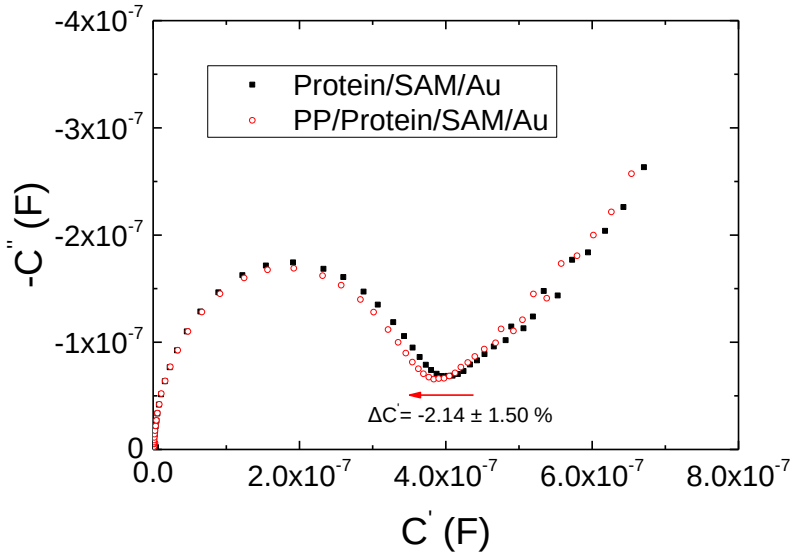

Figure 5.4 Complex capacitance plot for non-Faradaic EIS measurements performed right before (solid symbols) and after (open symbols) protein phosphorylation (PP).

This can be explained taking into account the small size of the phosphate groups (only 95 Da) which does not guarantee a sufficient displacement of solvent molecules at the

electrode interface. Along with the small changes in the biolayer geometry, it must be considered that the phosphorylation sites might be hindered within the 3D protein structure hampering even more the capacitance changes. A different approach for the protein phosphorylation was then needed.

5.4 Multimodal assay for protein phosphorylation detection

5.4.1 Detection principle and assay's implementation

In order to increase the sensitivity of the detection, a more elaborated process was therefore required. A strategy for enabling signal amplification as well as multiple detection by means of different techniques consisted in using signal probes (i.e. molecules able to enhance the magnitude of the measured response) that could specifically attach to phosphorylated proteins. Such a strategy would have allowed both to generate a larger signal exploiting the use of tags - such as redox probes - and to specifically distinguish between electrochemical signals arising from phosphorylation reaction and from reactions in presence of inhibitor of phosphorylation. The latter is not a trivial point since the compounds used for the phosphorylation reaction could interfere with the assay and cause non-specific signals. To implement such a strategy, thio-phosphorylation was carried out instead of normal phosphorylation reaction. Thio-phosphorylation is a process that differs from normal phosphorylation only for having a sulphur atom that substitutes an oxygen atom in the phosphate group PO_4^{3-}. A thiophosphate group is then transferred from the sulphur-modified ATP (ATP-S) to the protein that becomes thio-phosphorylated. Thus, by using ATP-S, the protein gains a PSO_3^{3-} group instead of PO_4^{3-} but the substantial difference in a biosensing platform is that the sulphur atom provides a means for gold nanoparticles to specifically tag only phosphorylated protein. This happens because of the strong sulphur-gold affinity (Pensa *et al.*, 2012; Häkkinen, 2012). Evidence that ATP-S do not affect the amount of protein phosphorylation can be found in the work of Bhalla *et al* (2015b).

Once the protein is thio-phosphorylated and GNPs specifically bind on it, part of the gold surface can be exposed to a thiolated redox probe, such as 6-(ferrocenyl)hexanethiol (Fc) (Figure 5.5).

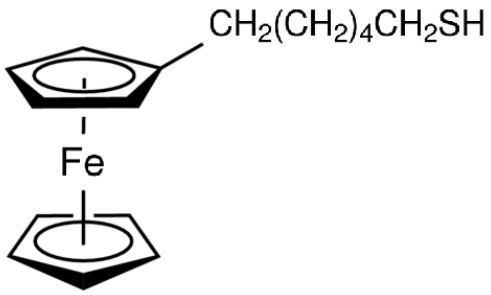

Figure 5.5 6-(ferrocenyl)hexanethiol (Fc) used for the detection of protein phosphorylation assay.

As anticipated, the redox activity of such compounds can enable electrochemical detection using, for instance, DPV. The biosensing principle here reported is graphically depicted in Figure 5.6. By using this strategy, prominent signal changes due to the electrochemical double layer modification were induced by means of the Fc-crown-like-structure in electrodes where thio-phosphorylation occurred. Not only real time OCP measurements but also successive impedimetric and voltammetric recordings could be performed in the same cell without the need of changing measurement solution, simply by flowing suitable reagents to the array. The multimodal detection both provided a cross-validation tool for the different techniques and an effective way to distinguish true positives.

In summary, the novel biosensing principle consists of a 3-step assay in which parallel detection of protein phosphorylation can be carried out by multiple electrochemical and nanoplasmonic techniques. In the first step (Figure 5.6 A-*iv*), phosphorylation of myelin basic protein (MBP) by protein kinase C alpha (PKC-α) is achieved by using 5'-[γ-thio] triphosphate (ATP-S) as a source of phosphate in the presence and absence of known inhibitor PKC-α, GF 109203X. The phosphorylation process is monitored in real time using an in-house built open circuit potential (OCP) measurement system. In the second step, GNPs are added to the reaction (Figure 5.6 A-*v*), which attach spontaneously to the thio-phosphoryl groups. This facilitates detection of

phosphorylated proteins using a localised surface plasmon resonance technique as previously reported in the work led by Bhalla (2015b). Finally, in the last step (Figure 5.6 A-*vi*), thiolated Fc is added to the system, which is grafted onto the gold nanoparticles allowing detection of phosphorylation using DPV and EIS. In terms of measurements recording, OCP could be monitored in real time from the immobilisation of the MBP to the end of the assay while EIS, DPV and LSPR were performed only before and after the OCP recordings.

The advantage of using these techniques on one platform is that they can act as complementary biosensors to each other, providing on-chip self-validation of the results for more effective and reliable measurements.

5.4.2 Biosensor fabrication, methods and experimental set up

The thio-phosphorylation assay described in Figure 5.6 was performed under a flow rate of 100 µl/min using a peristaltic pump (Watson Marlow 323-Du) and an in-house built polytetrafluoroethylene (PTFE) flow cell with an inner chamber of approximate dimensions 25 × 8 × 5 mm^3 (length × width × height) and an internal volume of 1 ml accommodating the array of electrodes. A linear array of 4 gold electrodes with 2 mm diameter was prepared in-house by thermal evaporation (BOC Edwards, UK) of 20 nm Cr and 100 nm Au on glass slides. The electrode array was sonicated for 3 min in acetone followed by rinsing with ethanol and then ultrapure water.

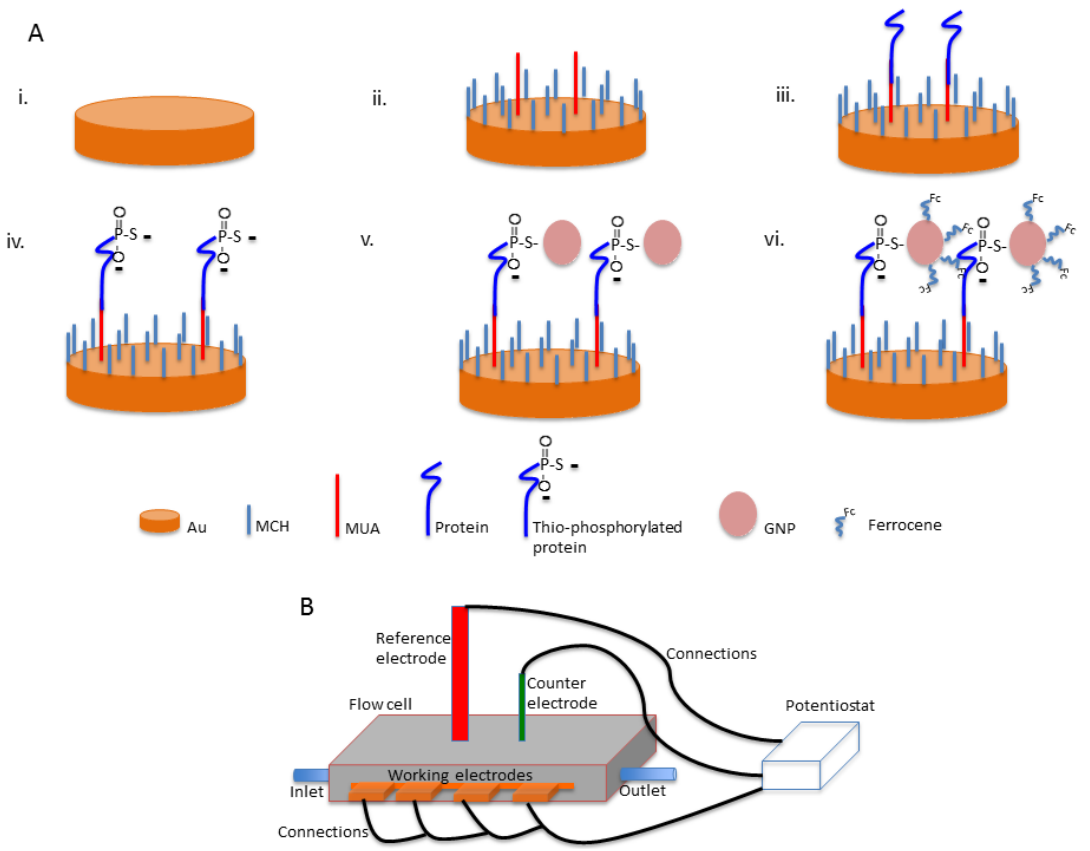

Figure 5.6 Scheme of the phosphorylation detection using the biosensor developed in this work: A) Kinase assay showing (i) bare gold electrode, (ii) surface functionalisation using MUA/MCH, (iii) protein immobilisation, (iv) thio-phosphorylation, (v) attachment of gold nanoparticles, (vi) nanoparticles with attached ferrocene. B) Dummy schematic representation of the in-house built flow cell and measurement system for the electrochemical detection.

A SAM made of 1 mM MUA and MCH in a ratio of 1:9 MUA:MCH was immobilised overnight onto gold electrodes. In order to cover possible pinholes on the gold surface and to reduce non-specific binding, a 1 hour backfilling step was performed with 1 mM MCH. The SAM was activated by injecting 1 ml of an aqueous mixture of 40 mM EDC and 10 mM sulfo-NHS. For protein attachment, 200 µl of 156 µM MBP protein (in 10 mM MOPS pH 7.0 containing 128 mM $MgCl_2$, 641 mM EDTA, 1.134 µg inactive lambda phosphatase, and 0.05% sodium azide) was flown into the cell; unreacted carboxyl groups were blocked using 500 µl of 10 mM ethanolamine, pH 8.5, in aqueous solution. Phosphorylation of MBP was carried out in 10 mM Tris base, pH 7.4 containing 6 mM NaCl, and 0.4 mM $MgCl_2$ (hereafter referred to as *reaction buffer*). The whole reaction volume was fixed to 100 µl for all replicates and their

controls. 1 μM ATP-S and 4 units of PKC-α (1 unit per 25 μl) were subsequently added. To initiate the phosphorylation reaction, 5 μl of PKC-α lipid activator (1:20 of reaction volume) containing 0.5 mg/ml phosphatidylserine and 0.05 mg/ml diacyglycerol in 20 mM MOPS (pH 7.2), 25 mM β-glycerol phosphate, 1 mM sodium orthovanadate, 1 mM dithiothretiol, and 1 mM $CaCl_2$, was diluted. Control reactions were performed by adding 0.1 μM PKC-α kinase inhibitor (GF 109203X) to the phosphorylation reaction. The modification with gold nanoparticles and following washing step required only 10 minutes in flow conditions. A further 10 min step was required for Fc modification by adding 500 μl of 1 mM Fc dissolved in ethanol and finally diluted 1:100 in the reaction buffer.

All chemicals were purchased from Sigma–Aldrich (UK). Dephosphorylated MBP and PKC-α lipid activator were purchased from Millipore. PKC-α human recombinant kinase produced in Sf9 cells was procured from ProSpec-Tany TechnoGene Ltd (Israel).

A CompactStat potentiostat (Ivium Technologies, The Netherlands) was used to perform impedance measurements and DPV in a three-electrode cell with an Ag/AgCl reference electrode (BASi, USA) and a platinum wire counter electrode (ALS, Japan). Once the electrochemical recordings were terminated, LSPR was measured using an in-house built system with discrete components, all bought from Ocean Optics (USA). The system had 3 parts: reflection probe (R400-7-UV-VIS) with both detector and light source, connected to a Tungsten Halogen source (LS-1-LL) and a spectroscope (USB4000-UV-VIS-ES). The data was obtained through absorption mode on a cross platform spectroscopy operation software (SPECTRASUITE) provided by Ocean Optics and each LSPR measurement lasted only few seconds.

The OCP system was home-made implemented and optimised by Wong (2015). The OCP was measured in real time using a complete monolithic FET-input ultra low input bias current instrumentation amplifier INA116 (Texas Instruments, USA). Difet® inputs, a very low input bias current of 3 fA at 25 °C, with special guarding techniques were used to achieve the very low input bias current performance and provide an accurate differential measurement. The circuit was designed in house with 4 amplifiers

operated at ± 15 V on a single PCB circuit board. A power supply circuit was made to provide ± 15 V to minimise the mismatch of the power rails. The outputs of the amplifiers are connected to a 4-channel-input analog-to-digital converter with input resolution of 24 bits measuring a range of ± 1 V (NI 9219 DAQ, National Instruments, UK). The array of 4 functionalised gold electrodes and the Ag/AgCl reference electrode were connected directly to the differential inputs of the amplifiers, with a platinum wire immersed in the cell connecting the electrolyte to ground to prevent common-mode rejection. LabVIEW (National Instruments, UK) was used to monitor and capture the open circuit potential measurement in real time simultaneously from the 4 digital outputs of the DAQ from the amplifiers array.

All the measurements were carried out in triplicate, values reported in this study are the mean of replicates. Reported errors are standard deviations from the mean.

5.4.3 EIS detection of protein phosphorylation

Non-Faradaic EIS measurements were performed on the gold arrays in the above-mentioned reaction buffer, scanning the frequency between 100 KHz and 0.1 Hz of an applied 10 mV a.c. voltage superimposed to the OCP.

Since in non-Faradaic experiments the capacitive component is the parameter mostly exploited in EIS analysis, the complex capacitance plot is generally used in order to characterize the system. The characterisation of the system consisted in plotting the complex capacitance diagram (C'' *vs.* C') and analyse this with respect to the frequency range used for the EIS monitoring. The plots were obtained using (3.10). The characterisation revealed that the frequency at which C'' showed its relative minimum throughout the different steps and for different electrodes was nearly always 1 Hz (Figure 5.7). For a small number of electrodes (< 5%) this frequency was slightly shifted to a lower or higher value, however they always remained on the proximity of 1 Hz. Therefore, for simplicity, 1 Hz was considered as a reference for all the measurements, with an error lower than 0.30 % introduced by this approximation. Introducing a single-point measurement rather than a wide spectrum response allowed

both the EIS experimental time to be significantly reduced from about 3.5 min (sweeping the whole frequency range) to ~ 20 s.

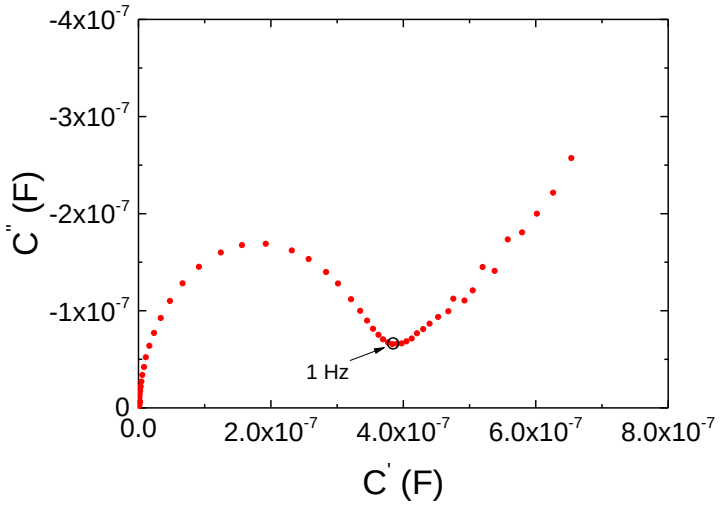

Figure 5.7 Complex capacitance plot for a generic non-Faradaic EIS measurements performed during the thio-phosphorylation assay. The plot is used to show that the measurement point at which the complex capacitance exhibits its relative minimum is obtained at the frequency of 1 Hz (circled point indicated with the arrow).

Furthermore, based on the assumption that the charge transfer resistance and the diffusion contributions can be neglected (Couniot *et al.*, 2015), the electrical equivalent circuit shown in Figure 3.1 can be used to model the electrochemical double layer. As a result, (3.11) and (3.12) can be used for the calculation of the resistive (R_S^*) and capacitive (C_{DL}^*) component of the electrochemical double layer which resulted in a practical easier data analysis implementation. Indeed both the parameters found a consistent correlation to the phosphorylation reaction carried out in the presence and absence of kinase inhibitor and could equally be used to demonstrate whether or not the phosphorylation event took place.

Prior to monitor thio-phosphorylation, the coverage of pinholes on the electrode surface by MCH backfilling was confirmed by means of EIS measurements: a decrease in capacitance signal of 11.3 ± 0.6% was observed (Figure 5.8), indicating the effectiveness of the backfilling process.

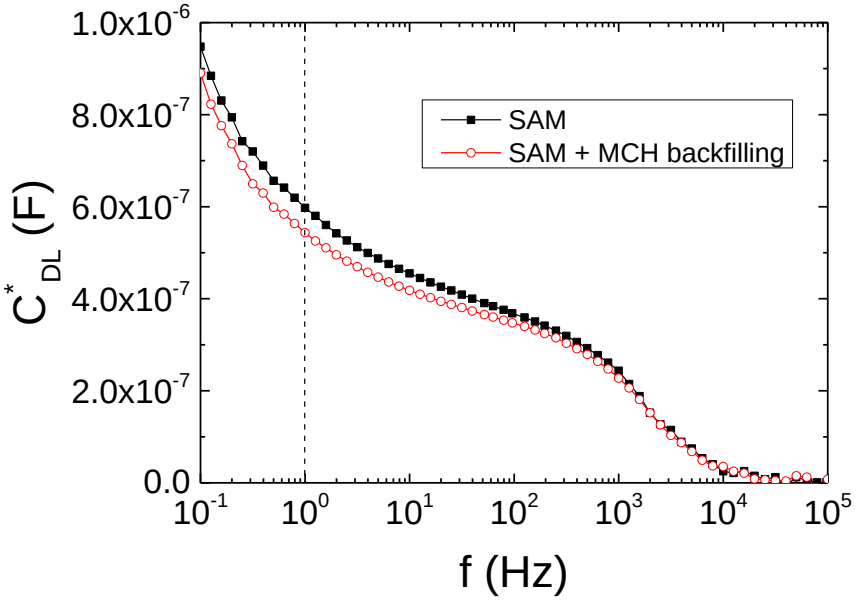

Figure 5.8 Plot of the real part of the complex capacitance ($C^*_{DL} = -\frac{1}{\omega Z''}$) v.s frequency. The plot shows a capacitance decrease after 1 h backfilling step with 1 mM MCH. The dashed line refers to the measurement at the frequency of 1 Hz.

In order to not interfere with the real time OCP measurements, EIS recordings were stopped after the protein immobilisation and retrieved at the end of the OCP monitoring. Therefore, impedimetric data obtained before phosphorylation were then compared with the signal acquired upon the Fc-crowned GNP attachment (Figure 5.9). It is important to highlight that the latter cannot be considered a non-Faradaic measurement any more since a redox probe has been introduced into the system. The effect of Fc, in fact, alters the charge transfer resistance of the electrode interface and the redox activity generates Faradaic current.

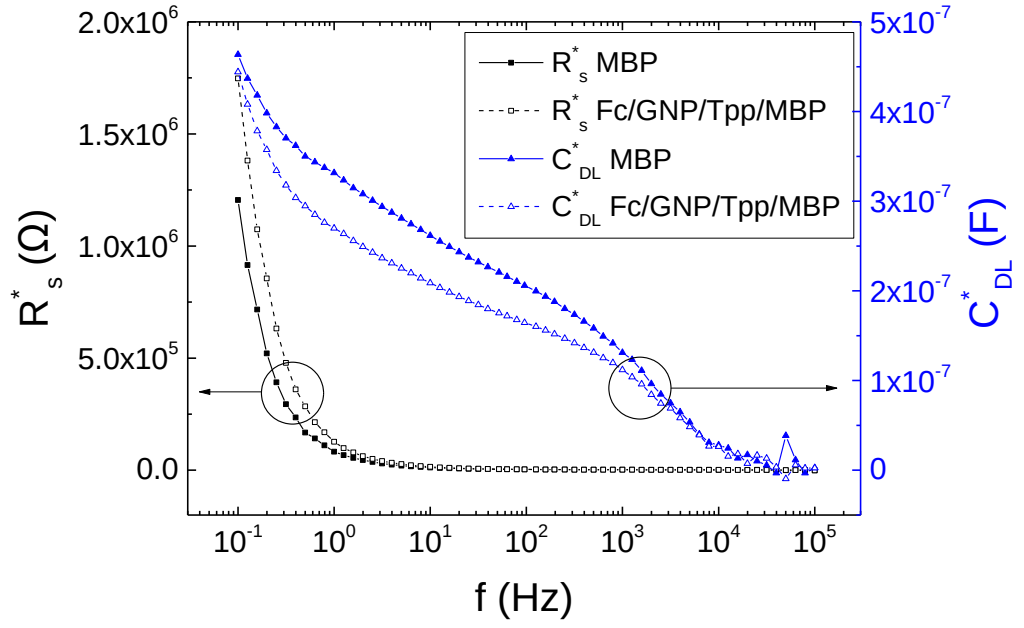

Figure 5.9 Real part of the complex impedance ($R_s^* = Z'$) (black plots) and real part of the complex capacitance ($C_{DL}^* = -\frac{1}{\omega Z''}$) (blue plots) plotted vs. Log (f). The plots refer to the measurements performed after MBP immobilisation (solid symbols) and at the end of the assay (empty symbols) i.e. upon thio-phosphorylation reaction (Tpp), GNPs and Fc attachment.

The impedance data analysis in Figure 5.9 showed an increase in R_s^* and a decrease in C_{DL}^*. However, the value of R_s^* must not be confused with the value of R_{ct} since they are obtained in different ways. It is worth highlighting that the R_{ct} is obtained by applying the Randles equivalent circuit (or any modified version) and fitting the impedance values to those electrical components. In this case instead, R_s^* corresponds solely to the real part of the impedance measurement and is not obtained through any fitting process. The increase in R_s^* ($\equiv Z'$) can be explained by observing Figure 5.10: the addition of Fc to the sensor biolayer induces a Faradaic current and a decrease in the charge transfer resistance that, translated in the complex impedance plot, means a compression of the complex impedance curve. As a result a semicircle could form at lower values of impedance. In Figure 5.10, the dashed lines are only previsions of how the semicircles would be if the measurements could be extended to lower frequencies. This means that the impedance plot obtained for the electrode where the complex GNP-Fc has been added would have a lower R_{ct} compared to the electrode where the phosphorylation reaction as well as the GNP-Fc steps did not take place yet. Moreover,

if we consider single points of the two lines corresponding to the same frequency (in Figure 5.10 such points have been circled, correspond to the frequency of 0.1 Hz and are indicated with Z^*_{MBP} and Z^*_{Fc}), we can notice that in the case of the sample with Fc, such points are characterised by having a higher value of Z' and hence, of R^*_S .

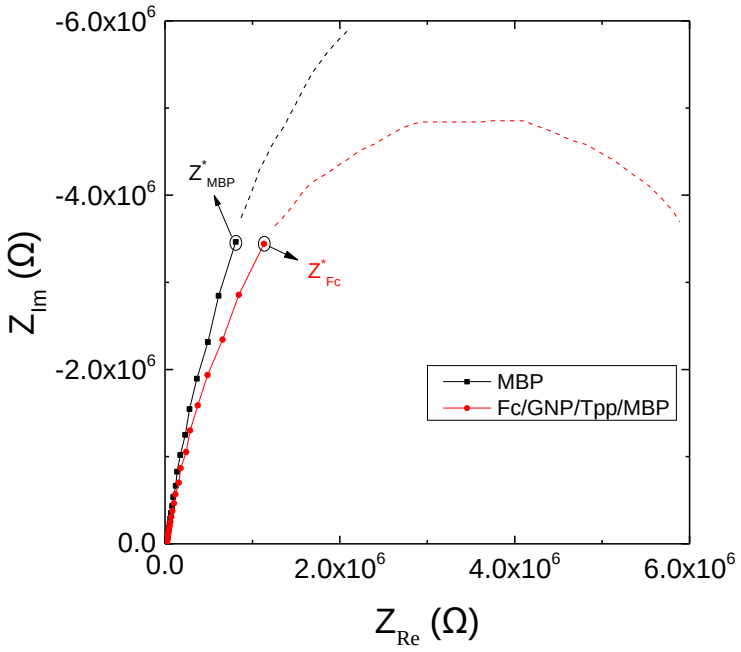

Figure 5.10 Complex impedance plot for non-Faradaic EIS measurements performed after MBP immobilisation (black solid line) and at the end of the assay (red solid line) i.e. upon thio-phosphorylation reaction (Tpp), GNPs and Fc attachment. The plot refers to measurements taken for the thio-phosphorylation assay and is meant to be used to explain the reduction of the R^*_S upon the thio-phosphorylation. The transition from non-Faradaic to Faradaic measurements induced by Fc attachment generated a compression of the impedance plot (red line). The values recorded upon Fc attachment are characterised by having a larger value of Z', which corresponds to R^*_S according to the model used to represent the system (Figure 3.1). The dashed lines are not representative of the measurements recorded but are only a prevision of the complex impedance plot that could be obtained if the frequency range would be extended to lower frequencies. Z^*_{MBP} and Z^*_{Fc} refer to the measurements performed at the frequency of 0.1 Hz.

For the impedimetric analysis, both R_{1Hz} (R^*_S at 1 Hz) and C_{1Hz} (C^*_{DL} at 1 Hz) changes were correlated to the presence and absence of kinase inhibitor as well as where thio-phosphorylation compounds (i.e. kinase, ATP-S and kinase activator) were not used (Figure 5.11). The results report on percentage shifts of 32 ± 10% and -16 ± 4.8% recorded for R_{1Hz} and C_{1Hz}, respectively, in the case of thio-phosphorylation. Negligible signal changes were observed for both control reactions where thio-phosphorylation compounds were not used (ΔR_{1Hz} = -1.4 ± 2.9% and ΔC_{1Hz} = 0.6 ±

1.9%) and where the experiment was carried out in presence of thio-phosphorylation compounds with addition of PKC-α kinase inhibitor (ΔR_{1Hz} = 0.9 ± 3.6% and ΔC_{1Hz} = 0.4 ± 3.1%). The former can give an indication of the non-specific interactions between Fc and protein. The latter is noticeably the most essential control for drug discovery application as it allows proving the efficacy of new possible drugs in terms of preventing protein phosphorylation.

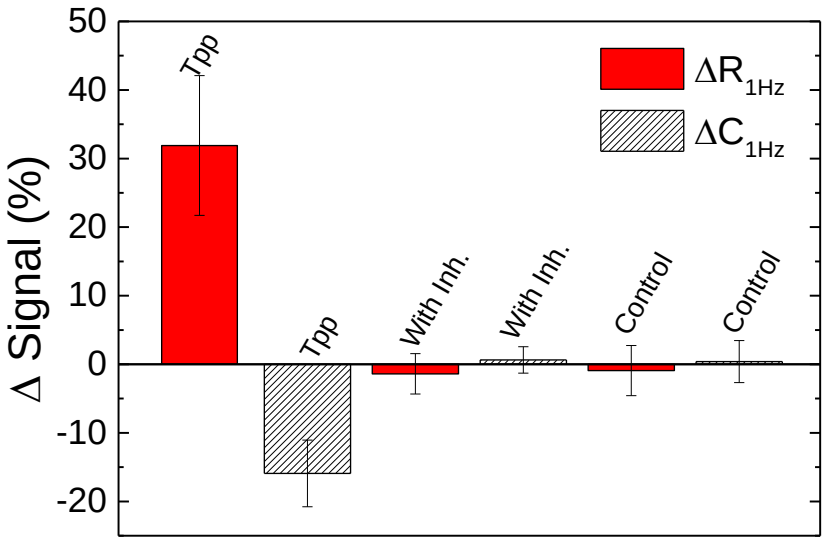

Figure 5.11 Signal changes of R_{1Hz} (solid bars) and C_{1Hz} (black and white bars) obtained for the thio-phosphorylation reaction performed without kinase inhibitor ("Tpp"), with kinase inhibitor ("With Inh.") and in absence of thio-phosphorylation compounds ("Control") i.e. if ATP-S, PKC-α, PKC-α lipid activator and kinase inhibitor were not used.

5.4.4 Detection of the surface charge changes upon protein phosphorylation

The biosensor used in the configuration depicted in Figure 5.6 could monitor the protein phosphorylation in real time by means of an OCP system which measurements and optimisation were performed by Wong (2016). In Figure 5.12 it is showed the OCP real time measurements where a change of -30.0 mV could be registered upon the thio-phosphorylation of MBP protein due to the negative charge of the thio-phosphate groups. The potential change was significantly lower (only -1.7 mV) when

the reaction was carried out in the presence of kinase inhibitor of phosphorylation (PKC-α). Nevertheless, both the potential changes indicate a decrease of the surface charge due to the addition of the negatively charged phosphate groups to MBP. As anticipated, the sulphur atoms resulting from the thio-phosphorylation enabled an easy and rapid attachment of gold nanoparticles by means of sulphur bonds where the thio-phosphorylation takes place.

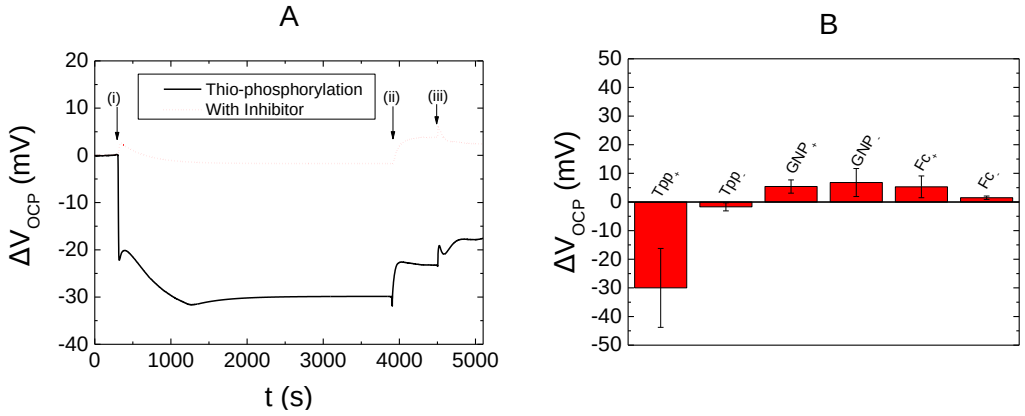

Figure 5.12 A) OCP signal changes obtained for the thio-phosphorylation reaction (solid line) and for the reaction carried out in presence of kinase inhibitor (dotted line). B) Potential variations obtained at different steps in presence (+) and absence (-) of kinase inhibitor.

Upon GNP addition, a voltage shift of 5.4 ± 2.3 mV is observed in thio-phosphorylated samples and -6.8 ± 4.9 mV for inhibition reactions. These shifts are mostly attributed to the changes in buffer conditions upon introducing gold nanoparticles (in 0.1 mM PBS) in the flow cell. In fact, when Fc was successively immobilised on GNPs, this caused a shift of only 1.5 ± 0.6 mV for reactions in presence of inhibitor compared to 5.3 ± 3.8mV shift obtained in absence of inhibitor. This confirms that the attachment of the complex GNP-Fc mostly occurs in presence of thio-phosphorylation where inhibitor is not used. A further confirmation that the OCP signals (upon gold nanoparticles attachment) were due to the buffer effect, was supported by the LSPR detection of nanoparticles in reflection mode which signal was already previously reported by Bhalla *et al.* (2015b).

5.4.5 Validation of the assay by means of DPV and LSPR

The advantage of implementing a multimodal detection platform was the possibility of cross-validating the step-by-step sensor fabrication as well as the validity of the final results. For instance, the presence of gold nanoparticles could be observed by LSPR used in reflection mode. LSPR confirmed a significant presence of GNPs only for thio-phosphorylated samples (Figure 5.13): a consistent red (positive) shift of 5.8 ± 0.4 nm for samples where thio-phosphorylation took place was recorded, compared to 0.9 ± 0.2 nm shift for reactions in presence of phosphorylation inhibitor. The amount of GNPs binding on the surface was previously estimated by means of QCM and reported in the work led by Bhalla *et al.* (2015b). The results obtained in presence of phosphorylation inhibitor can be considered very positive considering the ability of GNPs to non-specifically attach to biolayers. In this respect, carrying out the assay in flow conditions greatly helped to remove the weak non-specifically attached GNPs onto the electrodes surface. It was reported by various authors that a stringent washing step is necessary to leave only the specifically bound GNPs (Star *et al.*, 2003; Whaley *et al.*, 2000) and experiments performed in this lab but not object of this dissertation also demonstrated a better non-specific removal efficacy by using flow systems.

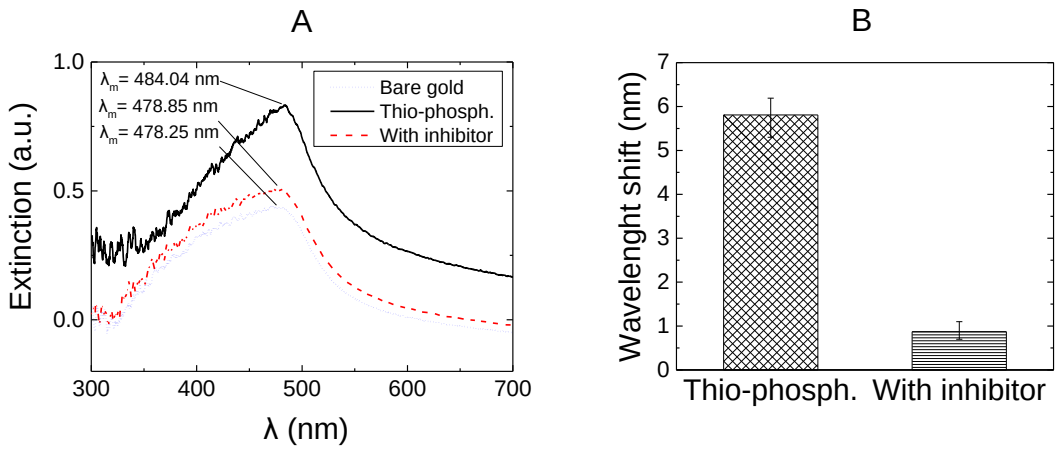

Figure 5.13 A) Raw LSPR spectra in the window of 300–700 nm obtained at the end of the electrochemical experiments; the spectra for a bare gold sample is shown for comparison. B) LSPR wavelength shifts obtained for the thio-phosphorylation reaction performed in presence (left bar) and absence (right bar) of kinase inhibitor.

The GNPs attachment provided a wide surface accessible for Fc grafting which, in turn, was important not only for EIS detection of phosphorylation of the proteins but also for DPV signals (Figure 5.14).

Performing DPV on the same platform, provided perhaps the most powerful tool to crosscheck the thio-phosphorylation event. DPV measurements (Figure 5.14) clearly showed the Fc peaks. An Fc peak of 1.31 ± 0.26 μA height (using baseline subtraction) was detected at 0.59 V, while no peak was observed for the controls.

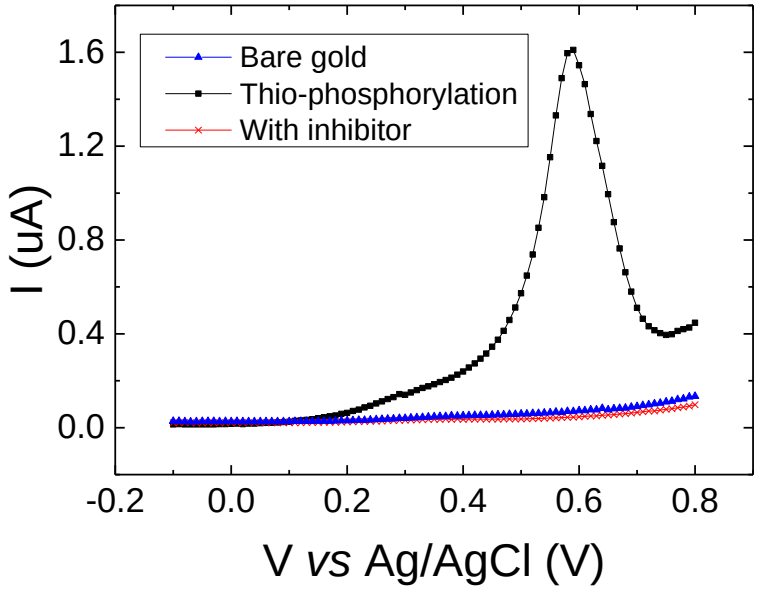

Figure 5.14 DPV measurements recorded after Fc injection.

5.5 Conclusions

In this Chapter a multimodal approach towards the detection of protein phosphorylation has been demonstrated as an example on how the engineering of the biorecognition interaction improve the target detectability. Moreover, the assay that is implemented enables the use of signal probes, such as nanoparticles and redox molecules that are only bound to the surface in the case of a true positive signal. Combining multiple sensing techniques on a single platform introduced specificity and sensitivity to the test and allowed both real time detection and on-chip self-validation of the results for effective and reliable measurements.

In particular, such a multimodal approach was successfully implemented using a small array of electrodes in a flow cell for detecting phosphorylation of proteins driven by kinases. The phosphorylation of MBP by PKC-α in the presence of a known inhibitor was tested, however this approach can be used to assay activity of any kinase-protein pair in the presence of known/unknown inhibitors. In particular, EIS, OCP and DPV were combined for parallel sensing on an array of electrodes. GNPs and a thiolated ferrocenyl compound have been used as reagents to provide extra sensing capabilities. In order to verify GNPs attachment, LSPR has been additionally used for providing further signal validation. The system here reported, allowed protein phosphorylation driven by kinases to be successfully detected. This study could be used to develop an integrated device with multiple sensing technologies, as demonstrated, for pharmaceutical industries and academia to discover drugs. Moreover, screening inhibitors of kinase can be achieved exploiting simple and cost-effective consumables. It must be reported that aspects such as the effect of the thiol surface density, the ATP-S and inhibitor concentrations on the biosensor response have not been addressed due to time limitations but should be further investigated for the biosensor optimisation.

In a broader viewpoint, the multimodal approach could be translated to a range of other biosensing applications, such as biomedical and environmental, where different electrochemical techniques can be used to perform on-chip validation of true positives. The engineering of the biorecognition elements/reagents can allow the use of nanoparticles, redox molecules or other types of signal probes for signal validation and amplification.

References

Bantscheff, M., Hobson, S., & Kuster, B. (2012). Affinity purification of proteins binding to kinase inhibitors immobilized on self-assembling monolayers. In *Kinase Inhibitors*. Humana Press, 795, 149-160

Bhalla, N., Di Lorenzo, M., Pula, G., & Estrela, P. (2015a). Protein phosphorylation detection using dual-mode field-effect devices and nanoplasmonic sensors. *Scientific Reports*, 5, 8687/1-8.

Bhalla, N., Formisano, N., Miodek, A., Jain, A., Di Lorenzo, M., Pula, G., & Estrela, P. (2015b). Plasmonic ruler on field-effect devices for kinase drug discovery applications. *Biosensors and Bioelectronics*, 71, 121-128.

Caballero, D., Martinez, E., Bausells, J., Errachid, A., & Samitier, J. (2012). Impedimetric immunosensor for human serum albumin detection on a direct aldehyde-functionalized silicon nitride surface. *Analytica Chimica Acta*, 720, 43-48.

Chen g-Tai Chen,, Chen, W. Y., Tsai, P. J., Chien, K. Y., Yu, J. S., & Chen, Y. C. (2006). Rapid enrichment of phosphopeptides and phosphoproteins from complex samples using magnetic particles coated with alumina as the concentrating probes for MALDI MS analysis. *Journal of Proteome Research*, 6(1), 316-325.

Chen, Z., He, X., Wang, Y., Wang, K., Du, Y., & Yan, G. (2013). Ru (II) encapsulated phosphorylate-terminated silica nanoparticles-based electrochemiluminescent strategy for label-free assay of protein kinase activity and inhibition. *Biosensors and Bioelectronics*, 41, 519-525.

Cohen, P. (2002). The origins of protein phosphorylation. *Nature Cell Biology*, 4(5), E127-E130.

Cohen, P., & Alessi, D. R. (2012). Kinase drug discovery–what's next in the field?. *ACS Chemical Biology*, 8(1), 96-104.

Cohen, P. (2002). Protein kinases—the major drug targets of the twenty-first century?. *Nature Reviews Drug Discovery*, 1(4), 309-315.

Couniot, N., Afzalian, A., Van Overstraeten-Schlögel, N., Francis, L. A., & Flandre, D. (2015). Capacitive biosensing of bacterial cells: Analytical model and numerical simulations. *Sensors and Actuators B: Chemical*, 211, 428-438.

Daniels, J. S., & Pourmand, N. (2007). Label-free impedance biosensors: Opportunities and challenges. *Electroanalysis*, 19(12), 1239-1257.

Delbroek, L., Van Kolen, K., Steegmans, L., da Cunha, R., Mandemakers, W., Daneels, G., De Bock, P. J., Zhang, J., Gevaert, K., De Strooper, b., Alessi, D. R., Verstreken, P., & Moechars, D. W. (2013). Development of an enzyme-linked immunosorbent assay for detection of cellular and in vivo LRRK2 S935 phosphorylation. *Journal of Pharmaceutical and Biomedical Analysis*, 76, 49-58.

Diamandi, A., Mistry, J., Krishna, R. G., & Khosravi, J. (2000). Immunoassay of insulin-like growth factor-binding protein-3 (IGFBP-3): new means to quantifying IGFBP-3 proteolysis. *The Journal of Clinical Endocrinology & Metabolism*, 85(6), 2327-2333.

Formisano, N., Bhalla, N., Wong, L. C., Di Lorenzo, M., Pula, G., & Estrela, P. (2015). Multimodal electrochemical and nanoplasmonic biosensors using ferrocene crowned nanoparticles for kinase drug discovery applications. *Electrochemistry Communications*, 57, 70-73.

Freeman, R., Finder, T., Gill, R., & Willner, I. (2010). Probing protein kinase (CK2) and alkaline phosphatase with CdSe/ZnS quantum dots. *Nano Letters*, 10(6), 2192-2196.

Freeman, R., Gill, R., & Willner, I. (2007). Following a protein kinase activity using a field-effect transistor device. *Chemical Communications*, (33), 3450-3452.

Furusawa, H., Uemura, K., Yoshimine, H., & Okahata, Y. (2012). In situ monitoring of a trace intermediate during DNA phosphorylation by T4 polynucleotide kinase for transient kinetic studies. *Analyst*, 137(6), 1334-1337.

Goldsztein, A., Babar, S., Voué, M., De Coninck, J., Conti, J., Marchand-Brynaert, J., Devouge, S., Homblé, F., & Goormaghtigh, E. (2010). Gastric ATPase

phosphorylation/dephosphorylation monitored by new FTIR-based BIA–ATR biosensors. *Journal of Spectroscopy*, 24(3-4), 257-260.

Häkkinen, H. (2012). The gold-sulfur interface at the nanoscale. *Nature Chemistry*, 4(6), 443-455.

Jänne, P. A., Gray, N., & Settleman, J. (2009). Factors underlying sensitivity of cancers to small-molecule kinase inhibitors. *Nature Reviews Drug Discovery*, 8(9), 709-723.

Kee, J. M., Oslund, R. C., Perlman, D. H., & Muir, T. W. (2013). A pan-specific antibody for direct detection of protein histidine phosphorylation. *Nature Chemical Biology*, 9(7), 416-421.

Kerman, K., Chikae, M., Yamamura, S., & Tamiya, E. (2007). Gold nanoparticle-based electrochemical detection of protein phosphorylation. *Analytica Chimica Acta*, 588(1), 26-33.

Kerman, K., & Kraatz, H. B. (2009). Electrochemical detection of protein tyrosine kinase-catalysed phosphorylation using gold nanoparticles. *Biosensors and Bioelectronics*, 24(5), 1484-1489.

Kinoshita, E., Kinoshita-Kikuta, E., Sugiyama, Y., Fukada, Y., Ozeki, T., & Koike, T. (2012). Highly sensitive detection of protein phosphorylation by using improved Phos-tag Biotin. *Proteomics*, 12(7), 932-937.

Kwon, H. S., Han, K. C., Hwang, K. S., Lee, J. H., Kim, T. S., Yoon, D. S., & Yang, E. G. (2007). Development of a peptide inhibitor-based cantilever sensor assay for cyclic adenosine monophosphate-dependent protein kinase. *Analytica Chimica Acta*, 585(2), 344-349.

Laufer, S., Thuma, S., Peifer, C., Greim, C., Herweh, Y., Albrecht, A., & Dehner, F. (2005). An immunosorbent, nonradioactive p38 MAP kinase assay comparable to standard radioactive liquid-phase assays. *Analytical Biochemistry*, 344(1), 135-137.

Lindsay, S. (2012). Biochemistry and semiconductor electronics—the next big hit for silicon?. *Journal of Physics: Condensed Matter*, 24(16), 164201.

MacKeigan, J. P., Murphy, L. O., & Blenis, J. (2005). Sensitized RNAi screen of human kinases and phosphatases identifies new regulators of apoptosis and chemoresistance. *Nature Cell Biology*, 7(6), 591-600.

Miao, P., Ning, L., Li, X., Li, P., & Li, G. (2011). Electrochemical strategy for sensing protein phosphorylation. *Bioconjugate Chemistry*, 23(1), 141-145.

Nordin, H., Jungnelius, M., Karlsson, R., & Karlsson, O. P. (2005). Kinetic studies of small molecule interactions with protein kinases using biosensor technology. *Analytical Biochemistry*, 340(2), 359-368.

Parang, K., & Sun, G. (2010). Protein kinase inhibitors in drug discovery. *Pharmaceutical Sciences Encyclopedia*, 27, 1-67.

Pensa, E., Cortés, E., Corthey, G., Carro, P., Vericat, C., Fonticelli, M. H., Benítez, G., Rubert, A. A., & Salvarezza, R. C. (2012). The chemistry of the sulfur–gold interface: in search of a unified model. *Accounts of Chemical Research*, 45(8), 1183-1192.

Roskoski, R. Jr. USFDA approved protein kinase inhibitors. http://www.brimr.org/PKI/PKIs.htm (Last accessed 21 September 2015)

Sawasdikosol, S. (2010). Detecting tyrosine-phosphorylated proteins by western blot analysis. *Current Protocols in Immunology*, 89, 11.3.1-11.3.11.

She, Z., Topping, K., Shamsi, M. H., Wang, N., Chan, N. W., & Kraatz, H. B. (2015). Investigation of the utility of complementary electrochemical detection techniques to examine the in vitro affinity of bacterial flagellins for a toll-like receptor 5 biosensor. *Analytical Chemistry*, 87(8), 4218-4224.

Shiosaki, S., Nobori, T., Mori, T., Toita, R., Nakamura, Y., Kim, C. W., Yamamoto, T., Niidome, T., & Katayama, Y. (2013). A protein kinase assay based on FRET between quantum dots and fluorescently-labeled peptides. *Chemical Communications*, 49(49), 5592-5594.

Snir, E., Joore, J., Timmerman, P., & Yitzchaik, S. (2011). Monitoring selectivity in kinase-promoted phosphorylation of densely packed peptide monolayers using label-free electrochemical detection. *Langmuir*, 27(17), 11212-11221.

Snir, E., Amit, E., Friedler, A., & Yitzchaik, S. (2015). A highly sensitive square wave voltammetry based biosensor for kinase activity measurements. *Peptide Science*, 104(5), 515-520.

Song, H., Kerman, K., & Kraatz, H. B. (2008). Electrochemical detection of kinase-catalyzed phosphorylation using ferrocene-conjugated ATP. *Chemical Communications*, (4), 502-504.

Star, A., Gabriel, J. C. P., Bradley, K., & Grüner, G. (2003). Electronic detection of specific protein binding using nanotube FET devices. *Nano Letters*, 3(4), 459-463.

Sugimoto, I., & Hashimoto, E. (2006). Modulation of protein phosphorylation by M r 25,000 protein partially overlapping phosvitin and lipovitellin 2 in Xenopus laevis vitellogenin B1 protein. *The Protein Journal*, 25(2), 109-115.

Wang, J., Cao, Y., Li, Y., Liang, Z., & Li, G. (2011). Electrochemical strategy for detection of phosphorylation based on enzyme-linked electrocatalysis. *Journal of Electroanalytical Chemistry*, 656(1), 274-278.

Wang, Y., Zhang, L., Liang, R. P., Bai, J. M., & Qiu, J. D. (2013). Using graphene quantum dots as photoluminescent probes for protein kinase sensing. *Analytical Chemistry*, 85(19), 9148-9155.

Whaley, S. R., English, D. S., Hu, E. L., Barbara, P. F., & Belcher, A. M. (2000). Selection of peptides with semiconductor binding specificity for directed nanocrystal assembly. *Nature*, 405(6787), 665-668.

Wieckowska, A., Li, D., Gill, R., & Willner, I. (2008). Following protein kinase acivity by electrochemical means and contact angle measurements. *Chemical Communications*, (20), 2376-2378.

Wilner, O. I., Guidotti, C., Wieckowska, A., Gill, R., & Willner, I. (2008). Probing kinase activities by electrochemistry, contact-angle measurements, and molecular-force interactions. *Chemistry-A European Journal*, 14(26), 7774-7781.

Wong C. (2016). A study of multichannel open circuit potentiometry in biosensor applications (Doctoral dissertation, University of Bath).

Xu, J., Sun, L., Ghosh, I., & Xu, M. Q. (2004). Western blot analysis of Src kinase assays using peptide substrates ligated to a carrier protein. *BioTechniques*, 36, 976-981.

Xu, X., Li, Y., Zhou, J., Nie, Z., & Yao, S. (2012). Peptide inhibitor based QCM biosensor for rapidly detecting protein kinase activity. In *Sensors, 2012 IEEE,* 1-4.

Xu, X., Zhou, J., Liu, X., Nie, Z., Qing, M., Guo, M., & Yao, S. (2012). Aptameric peptide for one-step detection of protein kinase. *Analytical Chemistry*, 84(11), 4746-4753.

Yan, J. X., Packer, N. H., Gooley, A. A., & Williams, K. L. (1998). Protein phosphorylation: technologies for the identification of phosphoamino acids. *Journal of Chromatography A*, 808(1), 23-41.

Zhang, J., Yang, P. L., & Gray, N. S. (2009). Targeting cancer with small molecule kinase inhibitors. *Nature Reviews Cancer*, *9*(1), 28-39.

Chapter 6. Cellular and bacterial EIS detection by means of capacitive measurements

Part of the work presented in this Chapter has been partly submitted for publishing.

6.1 Introduction

In the previous Chapters, EIS detection was fostered by the Faradaic currents arising either from the redox markers in the measurement solution or from the redox probes specifically attached to the target. Conversely, in this Chapter pure non-Faradaic measurements are shown as a way to achieve detection of bigger molecules. A label-free EIS sensor based on glycosylated surfaces for bacteria detection will be presented. The bulky properties and the charge of the analyte produced significant alterations in the electrochemical double layer that allowed the changes in capacitance to be recorded. At the end of this Chapter, a preliminary study demonstrating the detection of prostatic tumour cells based on capacitive measurements is also introduced.

Non-Faradaic measurements have the advantage of not using redox probes. However, with respect to Faradaic measurements, further solutions could need optimisation when the experiments are set up. This consists for instance in optimising the ionic strength of the measurement solution and guaranteeing the formation of a well organised and insulating SAM.

6.2 Capacitive sensors

As introduced in Chapter 3, the binding of an analyte in affinity sensors causes changes in the properties of the biolayer that, in turn, can be associated to changes in the capacitance of the system. Therefore, capacitive biosensors rely on redistributions of the biolayer as well as of the solvent molecules at the electrode-solution interface. It is worth highlighting the lack of redox markers for the recording of the measurements. Albeit this can be regarded as an advantage, it must be remembered that redox probe are essentially used as an amplification strategy for enhancing the sensor response. Indeed, the reduction and oxidation events generated by the redox probes are responsible for the Faradaic currents which bring the sensor output to be spread to a wider range of values, therefore the sensitivity can be augmented. On the other hand, adopting a sensing solution where these "*signal facilitators"* are not used requires a careful optimisation of the measurement set up in order to produce signals that can allow biomarkers detection.

Nevertheless, advances made in the last 10-15 years provided a better understanding and development in the field of capacitive sensors. For instance, one of the aspects that must be respected in a reliable capacitive sensor is the formation of a good insulating SAM since this has been proved to enhance the reproducibility and sensitivity of the sensing (Berggren *et al.*, 2001). In case such condition is not respected, leaky capacitors can generate, with resulting losses in the sensitivity. To understand this phenomenon one can simply imagine a parallel plate capacitor with a degraded dielectric that causes small d.c. currents to flow. Therefore, in biosensing applications, when a capacitive sensors has a defective SAM that causes leakage currents, the binding of target molecules could produce a minor response.

Once a good SAM is formed, a probe element able to bind to the analyte must be immobilised. Here again, the insulating condition must be respected. Eventually, the binding event between the probe and the target causes changes of the thickness, geometry, charges and dielectric properties of system at the sensor-solution interface. For instance, biological layers are characterised by having permittivity, ε_r, between 2 and 5 while water and aqueous solutions such as PBS have an ε_r of about 78-80 (Daniels and Pourmand, 2007). This means that displacement of solvent molecules

operated by the binding of molecules causes variation in the capacitance due to the changes in ε_r. More generally, targets having either a big size or a considerably different charge or ε_r are able to produce a larger signal change. These are the principles on which the capacitive sensors – which are a subgroup of impedimetric sensors – are based. In the schematic of Figure 6.1 such principles are shown. It can be seen how the geometry and the charge of the analyte that binds the probe immobilised onto the electrode can change the equivalent capacitance. The amount of charge of the biolayer immobilised onto the sensor area is counterbalanced by the charge at the metallic electrode.

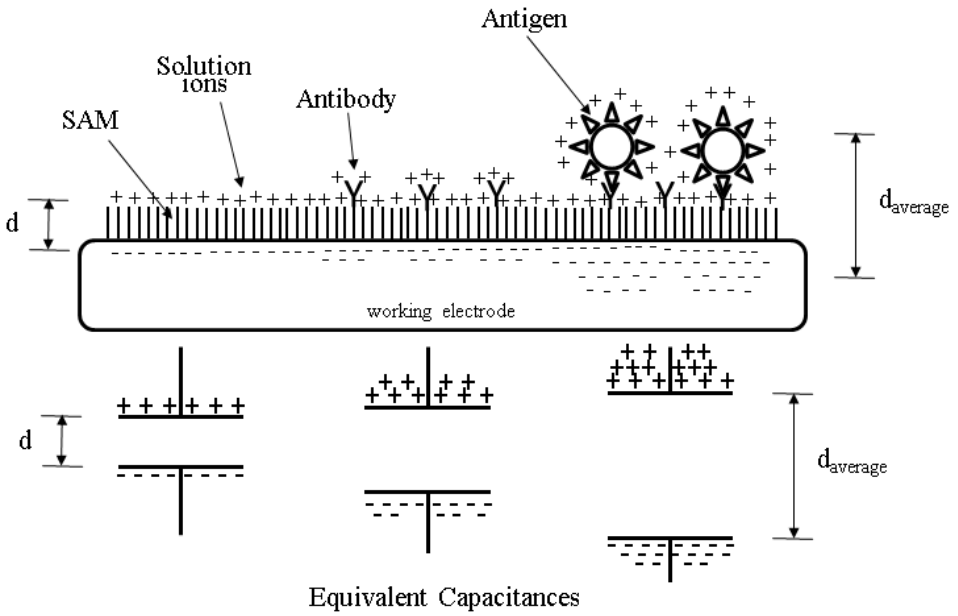

Figure 6.1 Models of equivalent capacitances for modified electrode surfaces in a measurement solution. As an example a generic complex antibody/antigen is used.

Based on the principle illustrated in Figure 6.1, if one compares the dimensions of proteins (< 10 nm) with those of bacteria (which in this study, can be approximated as cylindrically shaped having between 1 and 5 μm length × about 1 μm diameter of the base) it appears more evident that the latter could produce a larger capacitance change in biosensor applications.

6.3 Types of capacitive sensors for detection of cells and bacteria

Non-Faradaic-based EIS sensors are not widely reported in literature probably due to the scepticism of researchers in handling the impedance measurement, breaking it down and extrapolating the capacitance value.

Many capacitive sensors for bacterial and cellular detection exploits IDEs (Figure 6.2) as reported in section 3.2.4. In this type of sensors the electrode dimensions are comparable to the cells dimensions thus, large variations of the properties of the electrochemical double layer can be produced and detected. Drawbacks of such sensors are the complexity of fabrications and the fringing effect of the electric fields at the edges of the electrodes structures. On the other hand, electro-kinetic effects are associated with the fringing field and can be exploited for the fabrication of dielectrophoresis-based microfluidic devices. In this type of biosensors the non-uniformity of the electric field is used for the characterisation and manipulation of particles (Li *et al.*, 2014; Qian *et al.*, 2014; Wang *et al.*, 2009). Here, changes in the dielectric properties of the solution media or in the frequency and amplitude of the applied electric field enable contact-free manipulation of particles having nano- and micro-dimensions, irrespective of their charge. In particular, dielectrophoresis exploits the separation of the electric charges at the solid-liquid interface of the dielectric particles in solution due to their relative polarizability. As a result, the non-uniform electric field generates dielectrophoretic forces that push or attract the particles in the media towards regions of higher or weaker electric field gradients.

Examples of sensors for detection of cells and bacteria can be easily found in literature (Couniot *et al.*, 2015a; Couniot *et al.*, 2015b; Couniot *et al.*, 2015c; Haandbæk *et al.*, 2014; Li *et al.*, 2014; Braiek *et al.*, 2012; Varshney *et al.*, 2007; Varshney and Li, 2008).

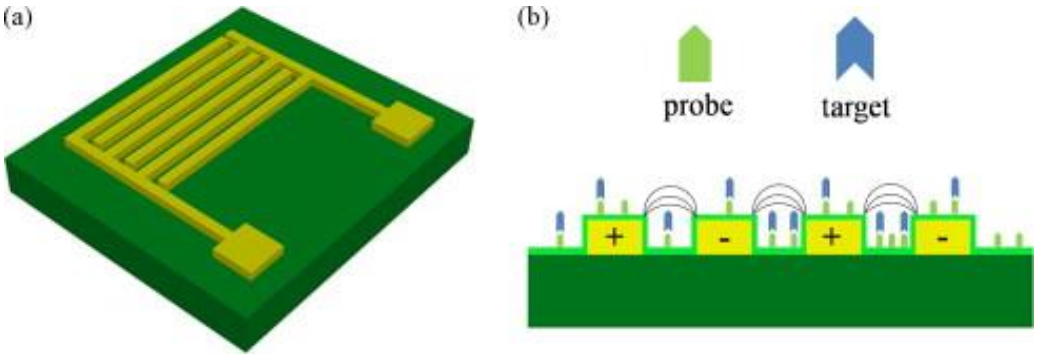

Figure 6.2 a) Example of an IDE biosensor with the classic combe-like structure of the electrodes. B) Cross view depicting the detection principle; the curved lines schematically represent the fringing effects. Reproduced from Tsouti et al. (2011).

Another type of sensor that performs capacitive measurements is based on the electrode-solution interface, as that presented in this work. The advantages of this strategy includes the simplicity of the set up and the lack of complex fabrication processes. The total capacitance is given by the series of the SAM capacitance, the recognition layer capacitance (given by the probe used to bind the target) and the diffuse layer capacitance (Berggren *et al.*, 2001). Example of electrode-solution interface-based capacitive sensors for bacterial and cellular detection can be found in the works of Adiguzel and Kulah (2012), Li *et al.* (2011), Ghafar-Zadeh *et al.* (2009), Prakash and Abshire (2008), Yang and Bashir (2008).

6.4 Glycosylated gold arrays as capacitive sensors for detection of bacteria

6.4.1 Introduction to pathogenic bacterial detection

Bacterial infection has a profound impact on global health (Coates *et al.*, 2002) and is believed to be responsible for more than 20% of the human tumours worldwide (Brachman and Abrutyn, 2009; Stein, 2011). The methods by which bacteria are currently detected in routine clinical microbiology has not significantly changed in recent decades. The process consists of an initial sample growth step where all the species in a sample are cultured in a rich medium in order to obtain a sufficient mass for subsequent analysis steps. The post-growth analysis allows isolation and

characterisation of a single species in a sample, usually by means of elaborate and expensive techniques such as staining, PCR, immunology and matrix-assisted laser desorption ionisation time-of-flight mass spectrometry MALDI-ToF (World Health Organisation, 2003). PCR and MALDI-ToF techniques can be more sensitive and specific than staining and immunological methods however, the cost of the assays is significantly higher and the risk of contamination in PCR tests play an important role. Although alternative, elegant at times, and effective studies on microorganisms detection have been reported (Mannoor *et al.*, 2012; Zourob *et al.*, 2008; Ma *et al.*, 2015), where also single bacteria sensing could be achieved (Kang *et al.*, 2014; Mohanty and Berry, 2008), the current 'gold standard' for clinicians is still represented by culturing methods, nucleic acid-based sensors, immunoassays and fluorescent-based techniques (Ahmed *et al.*, 2014). Limitations for adopting new solutions for diagnosis include the complexity of the fabrication process of new sensors, the complexity of assay implementation and sample processing and the prohibitive costs of introducing new equipment to perform bacterial detection. In order to overcome such boundaries while simultaneously introducing improvements in the current diagnostics, more simple and readily available devices must be provided.

Considering the current status of the national health systems worldwide and the continuous need for reducing costs of public healthcare, inexpensive and easily fabricated devices are required, perhaps able to perform clinical microbiology analysis in a rapid manner with parallel screening. The introduction of fast, simple and cheap sensors that could be easily employed in clinical laboratories would dramatically reduce both the times and the cost of the current bacterial diagnosis. For instance, a device able to provide an initial screening with adequately reliable outputs regarding the pathogenicity of the samples upon the initial growth step would radically avoid (or confirm the necessity) of performing more complex and expensive analysis.

6.4.2 Detection of type 1 fimbrial *Escherichia coli*

The study here reported shows bacterial detection using EIS signals as well as a metal–oxide–semiconductor field-effect transistor (MOSFET)-based strategy. The size and

charge of the bacteria were exploited to build an effective and reliable EIS sensor. Eventually, the MOSFET sensor provided a better sensitivity which, along with the reduced cost and ease of fabrication, can result in a very promising solution for initial screening of pathogenic bacteria. Bacterial detection has been demonstrated using a mannose-specific type 1 fimbrial *Escherichia coli* PKL1162 as a case study. Such results obtained with EIS and MOSFET sensors were compared to a well establish technique such as MALDI-ToF. EIS measurements were performed in a standard 3-electrode set up. The MOSFET sensor set up is instead represented in Figure 6.3.

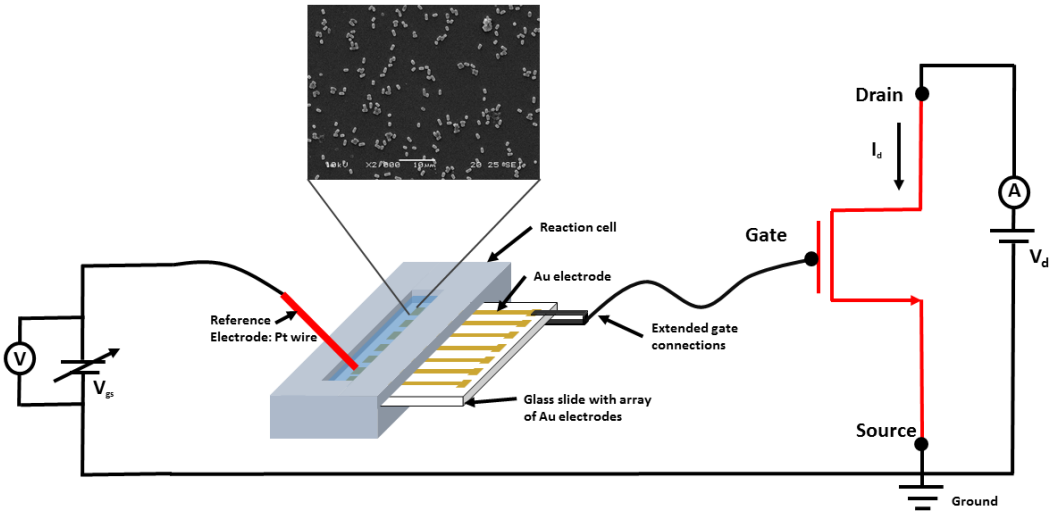

Figure 6.3 Working principle of the MOSFET sensor.

Amongst pathogenic bacteria, uropathogenic *Escherichia coli* (UPEC) is responsible for urinary tract infections. In order to colonise the cells of the urinary conducts and trigger a disease, UPEC can exploit hair-like protein structures expressed on their surface called fimbriae (Figure 6.4A), which allow bacteria to firmly adhere on the cells surface and not be washed away in the urinary flow. This attachment involves the hair-like proteins expressed on the bacteria surface and the glycosylated proteins of the cells surfaces. By glycosylation is meant the post-translational modification of the proteins through which they gain one or more carbohydrate chains (carbohydrates are also referred to as sugars) with a resulting changed affinity towards a number of possible targets (Lodish *et al.*, 2000). Lectin protein structures that constitute fimbriae, are expressed in at least 9 out of 10 UPEC strains (Oelschlaeger *et al.*, 2002). As the

specificity can vary towards different glycosylated surfaces, several carbohydrate-specific fimbriae have been found and, amongst them, mannose-specific type 1 fimbriae is classified as one of the most commonly expressed (Hartmann and Lindhorst, 2011). The recognition event interests the glycosylated cell of the urinary tract and the mannose-specific protein, called FimH, situated at the tip of the fimbrial rod of the pathogenic bacteria (Figure 6.4B).

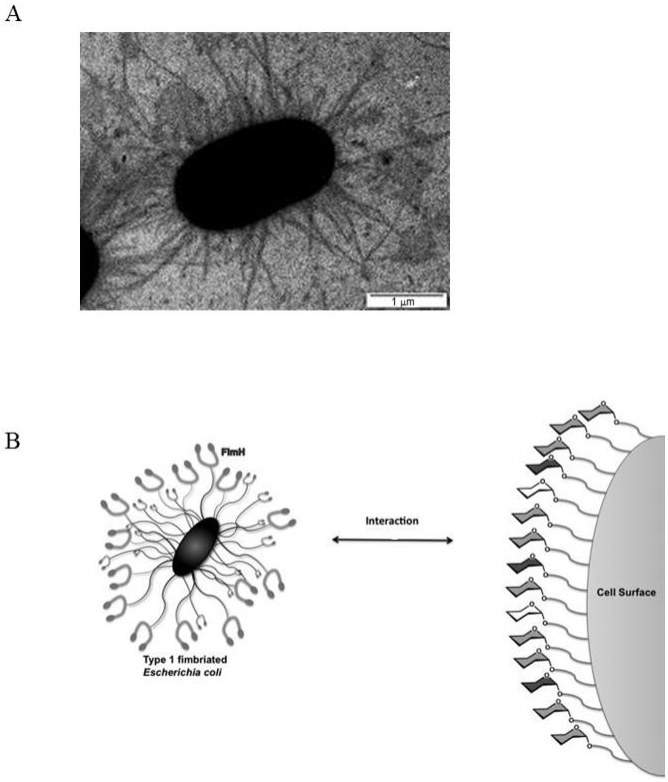

Figure 6.4 A) Transmission electron microscopy image of a type 1 fimbriated Escherichia coli showing the hair-like proteins expressed on its surface and B) schematic representation of the interaction between a type 1 fimbriated bacterium and a glycosylated cell surface. Reproduced from Hartmann and Lindhorst (2011).

The current regulations about the clinical limit of *Escherichia coli* in samples can vary from country to country. Typically, no *Escherichia coli* must be found in drinkable water although a cut-off level up to 500 colony-forming unit per ml (CFU/ml) is acceptable in some countries. On the other hand, it is worth reminding that the current protocols for the detection of pathogenic bacteria comprises a compulsory initial growth step in order to produce a sufficient mass to be analysed. In this context, a very inexpensive and fast biosensor that allows initial screening of pathogens would be

highly recommendable in order to save time and costs for further analysis. For such reasons, a very low LOD does not represent a strict target to achieve since the fabrication of an inexpensive biosensor for initial screening aims to simply verify the pathogenicity of samples.

In this study, in-house fabricated arrays of gold electrodes having 2 mm diameter and 100 nm thickness (deposited on glass substrates by means of thermal evaporation) are used as glycosylated surfaces for *Escherichia coli* PKL1162 recognition. The separation between each active area of the electrodes of the array was 5 mm and the electrodes were manually connected one at a time to the gate of the MOSFET by means of a metallic clip. The glycosylation of the gold surfaces happens by immobilizing aminoethyl-functionalised glycosides onto a mixed SAM made of HS-$(CH_2)_{17}$-$(OC_2H_4)_3$-OH and HS-$(CH_2)_{17}$-$(OC_2H_4)_6$-OCH_2COOH in a ratio of 1:4, following an already optimised protocol for MALDI-ToF (Both *et al.*, 2014; Noble *et al.*, 2012; Šardzík *et al.*, 2012; Zhi *et al.*, 2008). The modification occurs via EDC/sulfo-NHS chemistry and once the glycosides are immobilised, a blocking step of the non-reacted sites is performed using a 10 mM ethanolamine aqueous solution at pH 8.5. The affinity reaction involves a mannoside sugar which binds the uropathogenic *Escherichia coli* strain PKL1162 obtained by engineering the strain SAR18 with the plasmid pPKL174 (Reisner *et al.*, 2003). The bacteria were grown overnight under shaking in an incubator at 37 ºC in lysogeny broth growing media. The gold electrodes so modified were used not only for EIS measurements but also for MALDI-ToF, MOSFET readings and scanning electron microscopy (SEM) imaging. In the plots reporting data from measurements, error bars represent the standard deviation for three separate electrodes.

6.5 EIS detection of *Escherichia coli* on glycosylated gold arrays

6.5.1 Optimisation of the EIS sensor

The protocol for *Escherichia coli* detection was previously optimised for obtaining maximum MALDI-ToF signals (Šardzík *et al.*, 2011; Hartmann *et al.*, 2010; Zhi *et al.*, 2008). However, this implies a long SAM (> 3.0 nm) that could reduce or even impede

the amplitude of non-Faradaic EIS measurements since the binding event happens far from the electrode surface. If one represents the system with equivalent capacitors (see section 2.2.1), the electrochemical double layer can be modelled as a series of two capacitors where the equivalent capacitance is given by (2.4). If the recognition layer (in this case the glycosides) is separately modelled from the target layer (the bacteria), C_H can be decomposed in two terms: C_P and C_T indicating the probe capacitance and the target capacitance, respectively. As a result, the system can be represented as a series of 3 capacitors now: C_P, C_T and C_D. In a series of capacitances, the smallest dominates. Nevertheless the aim of a capacitor sensor is to maximise the capacitance change measurements caused by the binding of the target. As a result if either C_P or C_D are much smaller than C_T, the sensor could be not able to detect changes in the electrochemical double layer due to the recognition of the target.

However, in order to exploit the anti-fouling properties of PEG as well as the ability of long SAMs to form compact, well organised and insulting structures, it was decided to vary the measurement solution conditions rather than adopting different SAMs solutions. Moreover, shorter SAMs, as already demonstrated in the course of this dissertation, lead to irreproducibility of the EIS measurements over time, which is a "far-from-ideal" condition for a practical biosensor. The choice of such a compromise is not new in capacitive sensors studies. It was already reported that a low reproducibility induced by shorter SAMs could be rewarded by a larger signals and vice versa (Berggren *et al.*, 2001). However, here the reproducibility of the experiments was preferred over a possible lack of sensitivity since one of the most important conditions to be respected for a real biosensor is the reliability. Afterwards this choice resulted successful as a detectable signal was produced using a long SAM.

The imaginary and real part of the complex capacitance (C' and C'' respectively) were calculated using (3.10) from the complex impedance, which is given by the relation $C^* = C' + jC'' = \frac{1}{j\omega Z}$. The percentage change of the capacitance from step to step were then calculated considering only the real part of the capacitance, C', at the frequency where the absolute value of the imaginary part, C'', has its relative

minimum. The measurements were performed applying 10 mV a.c. voltage superimposed to the OCP scanning the frequency between 100 KHz and 0.1 Hz.

Initial EIS measurements were performed in PBS 10 mM with addition of 2.7 mM KCl and 137 mM NaCl (which results in a total ionic strength of 162 mM). The imaginary value of capacitances throughout the experiments (both upon glycosylation and bacteria binding) showed a relative minimum at the frequency of 126 Hz. A concentration of 4.2×10^9 CFU/ml of *Escherichia coli* PKL1162 could be detected even though the percentage capacitance change was of small entity: 3.5 ± 0.5 % (Figure 6.5). Upon glycosylation the absolute capacitance value corresponded to 189 ± 30 nF while after bacteria binding it increased to 195 ± 31 nF.

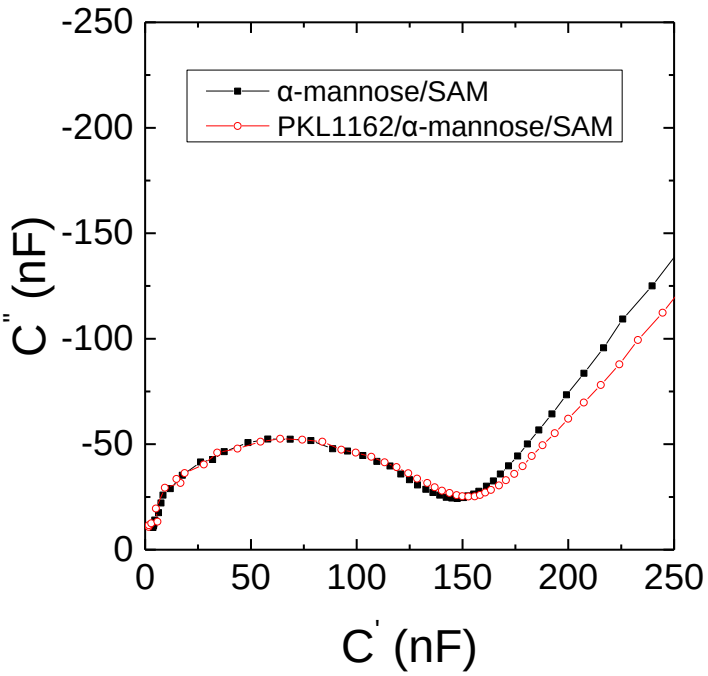

Figure 6.5 Complex capacitance plot for an electrode before (solid symbols) and after (open symbols) 4.2×10^9 CFU/ml Escherichia coli PKL1162 binding. Measurements performed in PBS 10 mM with addition of 2.7 mM KCl and 137 mM NaCl (which results in a total ionic strength of 162 mM).

Diluting the measurement solution 100 times instead, produced lower absolute values of capacitance. Here the point at which C'' showed its relative minimum was recorded at the frequency of 10 Hz throughout the experiments. The capacitance values ranged

from 118 to 132 nF for electrodes functionalised with α-D-mannose. Initial studies to test the effect of the buffer on the binding of bacteria showed a significantly larger change in the capacitance signal: a concentration of bacteria equal to 4.2×10^9 CFU/ml produced an increase in the capacitance of 18.6 ± 1.7%.

The use of a diluted measurement solution (PBS 1:100) reduced the ionic strength from 162 to 1.62 mM, which in turn, increased the Debye length from about 7.6 Å to 76 Å and improved the EIS detection. A further 10-time dilution of the measurement solution would only enlarge the Debye length by a $\sqrt{10}$ factor, according to (2.11). However, it was reported that cell damages could arise using a PBS diluted 1000 times because of the osmotic pressure induced by the high difference of salt contents between the inner and outer bacterial membrane (Couniot *et al.*, 2015; Peterson *et al.*, 2012). Moreover, a further dilution of the measurement solution can produce a larger variation of the EIS readings as proved in the prostate cancer cell detection carried out in this study (see section 6.10.3).

6.5.2 Increase of the absolute capacitance upon bacteria binding

By definition, the capacitance indicates the capacity of a material to store charge and is given by the expression $C = \frac{Q}{V}$, which, for a parallel plate capacitor, can be rewritten as $C = \frac{\varepsilon_o \varepsilon_r A}{d}$, where ε_o is the permittivity of the free space, ε_r is the relative permittivity that depends on the material between the two plates having surface area A and distant d from each other. The literature on capacitive sensors reports both on positive (Carrara *et al.*, 2009; Varshney and Li, 2008; Couniot *et al.*, 2015a; Couniot *et al.*, 2015b) and negative changes in capacitance measurements (Webster *et al.*, 2009; Li *et al.*, 2011) upon the target binding. However, the behaviour of the sensor is dependent on the electrode type, immobilisation strategies, SAM properties and type of molecules detected. Ethylene-glycol terminated SAMs have hydrophilic properties (Ostuni *et al.*, 1999; Carrara *et al.*, 2009) that lead to the entrapment of water molecules within the SAM chains. For our sensor this phenomenon prevents the displacement of the ions in solution that form the Helmholtz plane upon bacteria

binding. As a result, the bacterial and the underlying layers cannot be modelled simply by a series of capacitors (Figure 6.6) or as a single capacitor characterised by an increased distance separation *d* between the plates.

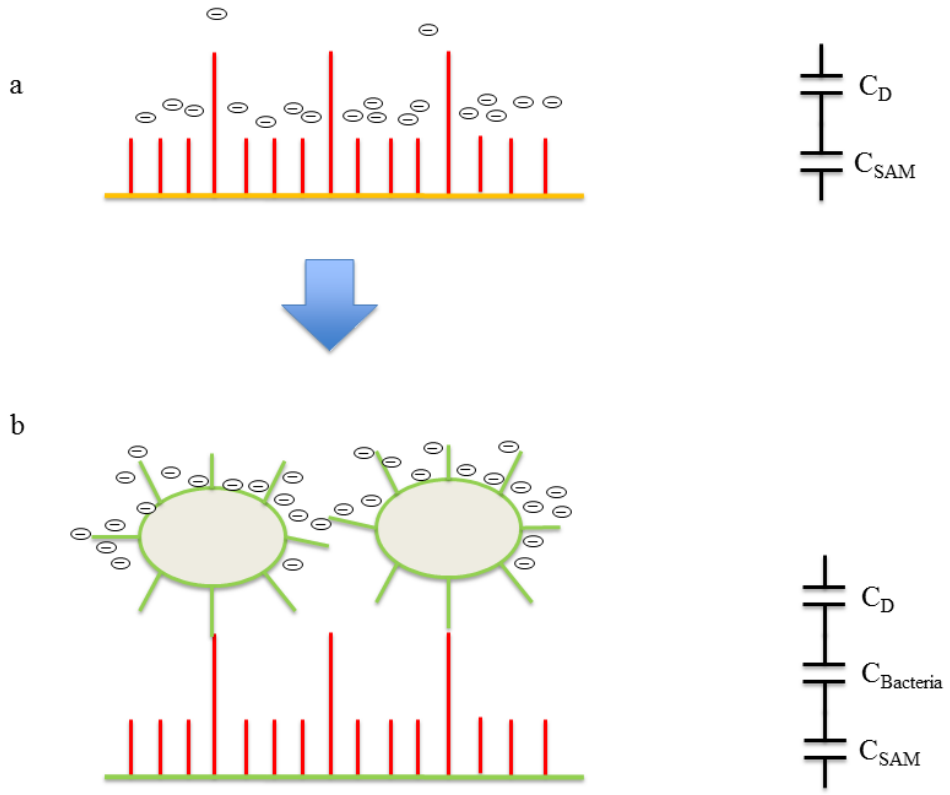

Figure 6.6 Equivalent circuit associated to an electrode functionalised with a SAM not having PEG terminations: a) before bacteria binding and b) after bacteria binding. Upon attachment of bacteria there is a displacement of solvent molecules from the SAM interface due to the hydrophobic properties of the SAM.

Rather, the binding event will augment the surface exposed and surrounded by the solvent molecules forming the Helmholtz plane. Therefore, this can be modelled as two capacitors in parallel where the first is fixed and the value of the second is characterised by larger numbers of both *d* and ε_r (Asami *et al.*, 1980) and its extent varies with the amount of bacteria bound onto the sugars (Figure 6.7). The combination of such factors following the bacterial adhesion produces eventually a positive shift in the total capacitance because the capacitance of the parallel branch will increase with increasing binding of the analyte.

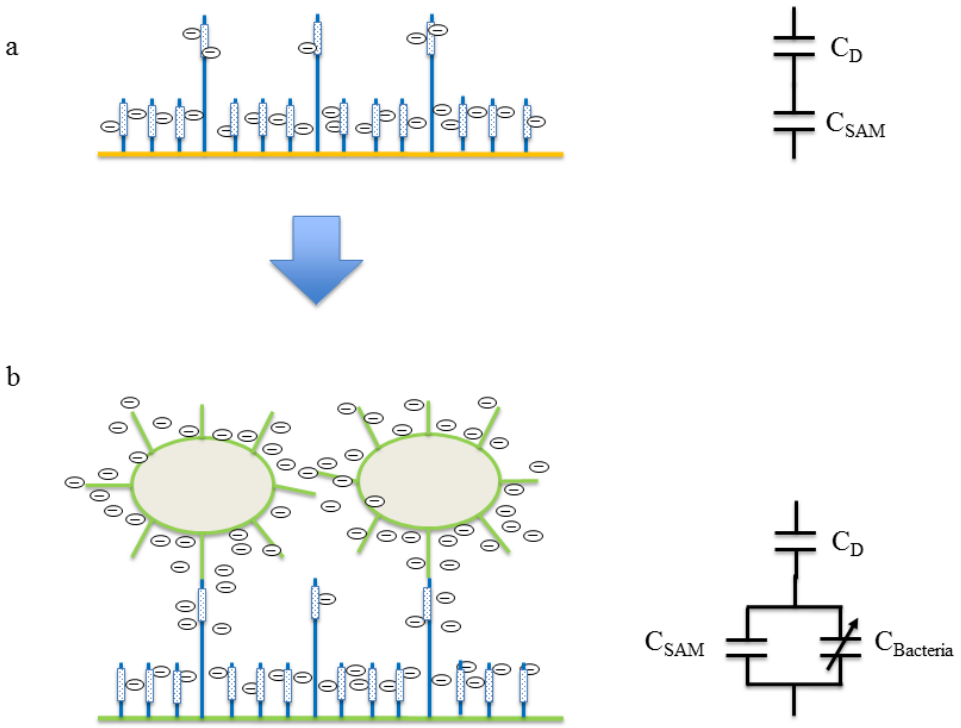

Figure 6.7 Equivalent circuit associated to an electrode functionalised with a PEG-terminated SAM: a) before bacteria binding and b) after bacteria binding. Upon attachment of bacteria there is still an entrapment of solvent molecules in the PEG molecules due to the hydrophilic properties of this type of SAM.

In a study carried out by Keighley *et al.* (2008), Faradaic measurements were performed on peptide nucleic acid (PNA) (which are neutrally charged synthesised oligonucleotidic strands) modified gold surfaces for DNA detection. Also in Keighley's system an increase in capacitance was recorded upon DNA binding in contradiction to what initially expected. Although the sensor for bacteria detection here reported can be considered different, an analogy can be made by describing both systems through Figure 6.7. Indeed, also the discrete charges added by the DNA strands can be modelled by an addition of a capacitors in parallel rather than in series. Moreover, considering that also in Keighley's study spacer molecules are used between the PNA probes, the hybridisation of DNA strands to PNA do not form a compact and continuous layer (in contrast to what happens instead for the SAM formation). In conclusion, the increase in capacitance upon DNA binding can be used for analogy to explain the increase in capacitance here reported for bacteria detection which can be in contrast to what demonstrated in previous studies.

6.5.3 EIS dose response to bacteria binding

The biosensor dose response was obtained by performing capacitance measurements varying the bacterial concentration between 4.2×10^6 and 4.2×10^9 CFU/ml of *Escherichia coli* PKL1162. The sensor response is plotted in Figure 6.8. For a concentration of *Escherichia coli* PKL1162 equal to 4.2×10^9 CFU/ml an increase in the capacitance of $18.6 \pm 1.7\%$ was recorded. The EIS capacitance change decreased to $4.1 \pm 1.3\%$ when a concentration down to 4.2×10^6 CFU/ml of *Escherichia coli* PKL1162 was used as a target on α-D-mannose. Beyond this limit, the signal overlaps the values of capacitance shift given by the negative control reactions, namely in presence of negative sugar probe (bacteria PKL1162 on 4-O-β-D-galactopyranosyl-D-glucopyranose (GalNAc) sugar), which produces a capacitance shift of $6.4 \pm 2.6\%$ and in presence of negative bacteria (K12 on α-D-mannose), which gives a capacitance change of $2.5 \pm 1.7\%$. Absolute values of capacitance range from 118 to 132 nF for electrodes functionalised with α-D-mannoside and from 123 to 155 nF upon bacterial adhesion. Similarly to other EIS studies reported in this dissertation, plotting the values of $\Delta C'$ *vs.* the concentration of *Escherichia coli* PKL1162 in linear scale, a very good fitting could be achieved using the Hill type response ($y = y_0 + (y_{max} - y_0)\, c^n/(k^n + c^n)$, where c is the concentration and k the dissociation constant) with a value of R^2 equal to 0.998.

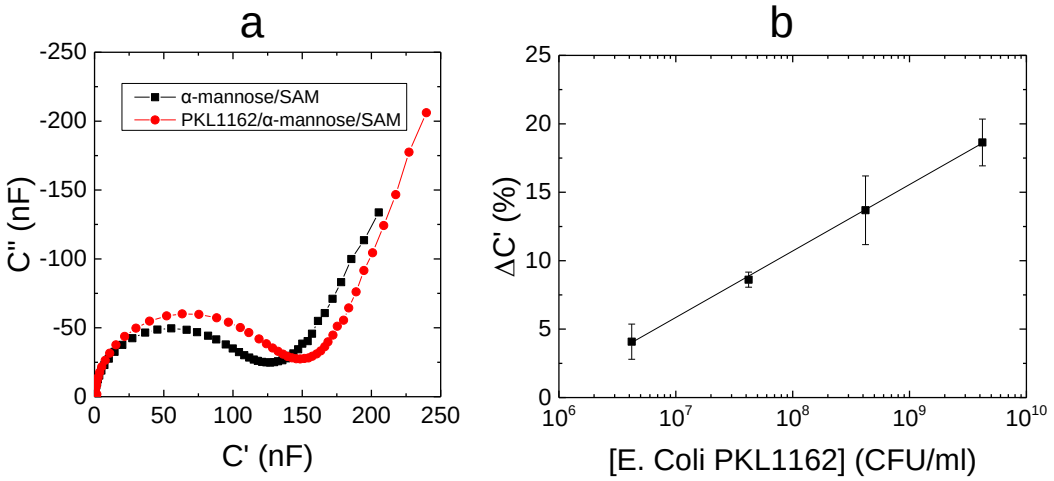

Figure 6.8 . a) Complex capacitance plots for an electrode before (black line) and after (red line) Escherichia coli PKL1162 binding. b) Changes of the real part of the complex capacitance vs. bacterial concentration. The curve exhibits a Hill type response ($R^2 = 0.998$) if plotted on a linear scale.

6.6 Capacitive measurements using a parallel-plate capacitor sensor

To confirm the data on the increase in capacitance obtained by EIS, which can be in contrast with what was previously reported in some works (Webster *et al.*, 2009; Li *et al.*, 2011), capacitance measurements were performed using a sensor developed by Hammond *et al.* (2014). The sensor consists of a gold parallel-plate capacitor characterised with dimensions of about 5 mm × 100 μm (width × depth) and 10 μm gap between the plates. The bacteria affinity assay was performed maintaining exactly the same conditions. The capacitance values were measured connecting the plates to an Agilent B1500A HR CMU Semiconductor Device Analyser. An a.c. potential of 10 mV superimposed to 0 V d.c. potential was applied sweeping the full dynamic frequency range available for the instrument, namely between 1 kHz and 1 MHz. The results are shown in Figure 6.9. It can be observed how the analyte response is recorded at frequencies smaller than 200 kHz where the components of the biolayer immobilised onto the electrode can still respond to the relatively slow perturbations. Above 200 kHz the ionic and electronic responses are recorded, instead, since only small particles such as atoms or electrons can follow the rapid oscillations of the electric field. Moreover, at high frequencies, the capacitance response is equal for different steps of the assay showing that there is no effect of the immobilised layer on the measurement. Rather, the signal is mostly due to the measurement solution reaction. It is worth highlighting also the decrease in capacitance upon the SAM formation which shows a compact and insulating layer formation. The capacitance changes are in agreement with the models reported in Figure 6.7.

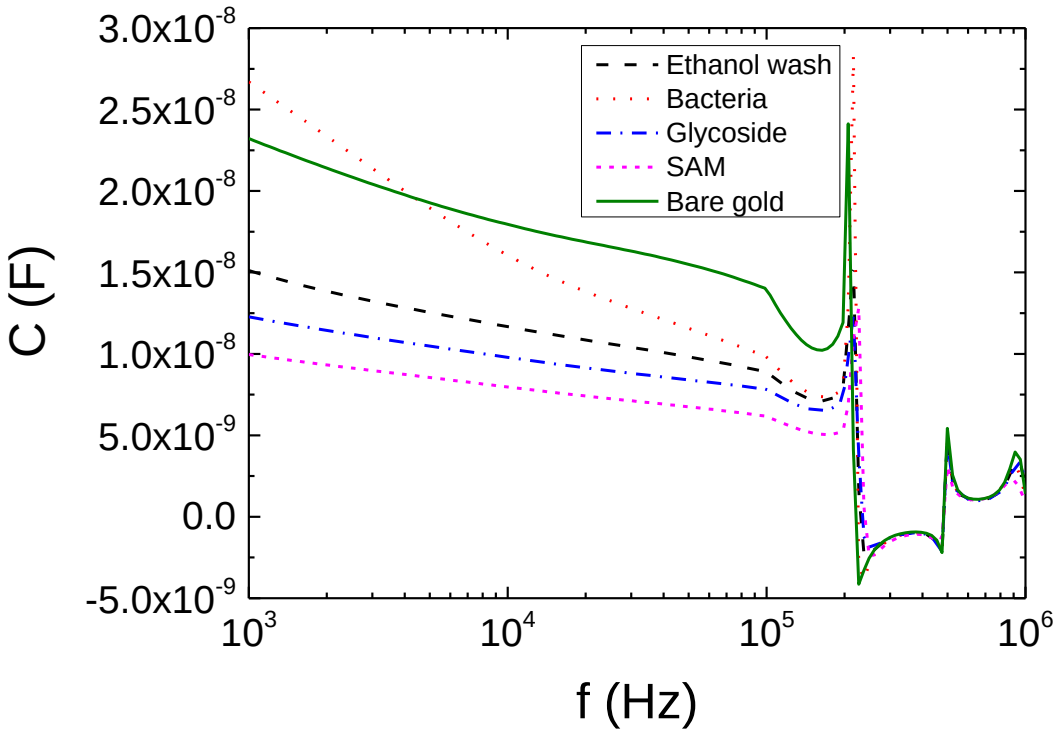

Figure 6.9 Capacitance measurements performed using a parallel-plates capacitor sensor designed by Hammond et al. (2014) that confirm the increase in capacitance upon bacteria binding.

In Figure 6.9 a significant decrease in capacitance, can be recorded upon SAM functionalisation. The surface glycosylation by means of α-mannosides produced a minor increase in capacitance (black curve). However, it is important to notice that it consists of a positive shift. The same trend is repeated upon bacteria binding using a concentration of 4.2×10^9 CFU/ml *Escherichia coli* PKL1162 but a significant larger signal is recorded (red curve). The last measurements was recorded upon washing the sensor with ethanol to verify the regeneration of the sensor induced by the disruption of the bacterial membrane and successive unbinding from the glycosylated surface. Nevertheless, a complete regeneration could not be achieved as can be seen by the capacitance signal not returning to the position obtained in first place after glycosylation (blue curve). This can be due to the partial retention of bacterial membrane fragments on the surface.

Although the capacitance response could not be recorded within the same frequency range used for the EIS measurements, it is worth noticing in Figure 6.9 that the largest

response is observed in the left part of the plot corresponding to the smallest frequencies used (and closer to the frequencies used in EIS). In particular, at 1000 Hz, the capacitance values were 23.2 nF for the bare gold electrodes, 9.96 nF after the formation of the SAM, 12.3 nF upon glycosylation, 26.7 nF upon binding of bacteria and 15.1 nF when the electrodes were rinsed with ethanol.

6.7 SEM microscopy of bacteria binding on glycosylated gold surfaces

Proof of bacterial binding and of good anti-fouling properties of the surface towards non-specific bacteria are confirmed by SEM images. The SEM images in Figure 6.10 (image *a* to *f*) show surface bacterial coverage at different concentrations of *Escherichia coli* PKL1162 (from 4.2×10^9 to 4.2×10^5 CFU/ml) on α-D-mannose as well as in the presence of negative controls. In particular, when the non-specific binding of high concentration (4.2×10^9 CFU/ml) of *Escherichia coli* strain K12 at the concentration of was tested on α-D-mannose (Figure 6.10g) only a small density of bacteria attachment was photographed. This confirmed both the very low specificity of the probe towards non-specific targets and the very good antifouling properties of the SAM. In general, the SEM pictures for the negative controls are congruent with both the EIS and MOSFET signals.

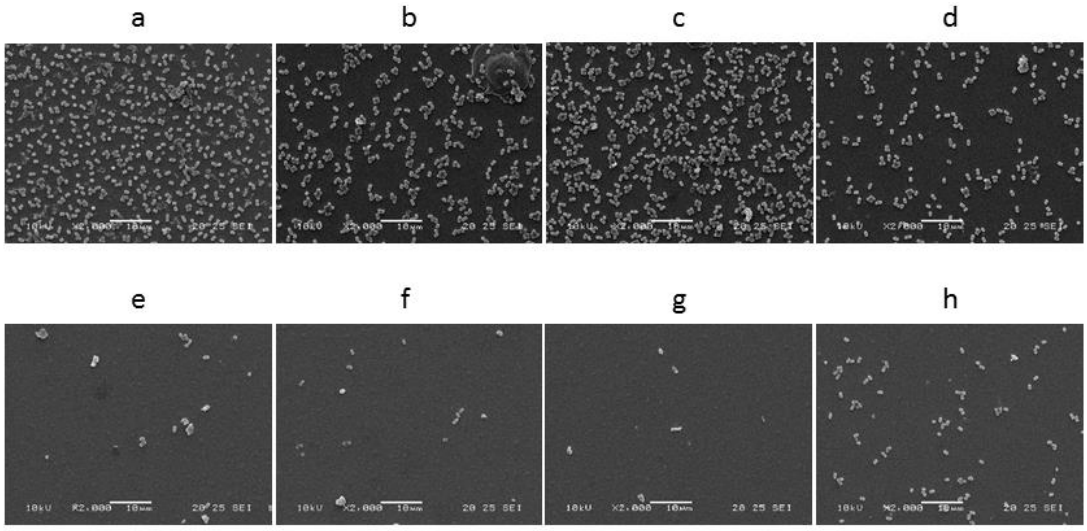

Figure 6.10 SEM microscopy pictures of Escherichia coli PKL1162 at the concentration of 4.2 × 10^9 (a), 4.2 × 10^8 (b), 4.2 × 10^7 (c), 4.2 × 10^6 (d), 4.2 × 10^5 (e), 4.2 × 10^4 (f), CFU/ml on α-D-mannose; Escherichia coli strain K12 at the concentration of 4.2 × 10^9 on α-D-mannose (g) and Escherichia coli strain PKL12 at the concentration of 4.2 × 10^9 on GalNAc (h).

6.8 Bacteria detection by means of MOSFET devices

The detection of bacteria by means of MOSFETs represents a very promising strategy for diagnosis of pathogens due to the large diffusion, simplicity and inexpensive cost of such devices. Therefore, the use of CMOS MOSFETs could dramatically cut down the costs of bacterial detection burden by serving as a reliable system for initial high throughput screening of pathogens in a rapid and inexpensive manner.

The bacteria binding assay was carried out in a reaction cell connecting the electrodes to the gate of an n-MOSFET via a metal wire as schematically shown in Figure 6.3. The n-MOSFETs were fabricated using AMS's 0.8 µm CMOS technology. The threshold voltage of the transistor was 0.82 V and transconductance was 69 µA/V. The length by width of the transistor was 10 µm × 2 µm. The terminals of the transistor were provided with diode protection circuitry. To operate the transistor for the measurements, a voltage of 50 mV was applied across the drain to source and the gate-source voltage (V_{gs}) was swept from 0 to 5 V. These settings limited the current to less than 75 µA to avoid any changes in the transistor due to heating. The V_{gs} values were sampled in the linear range of the I_D *vs.* V_{gs} characteristic.

Using MOSFETs, the limitation arising in EIS measurements from the contrasting combined effect of the variation of the relative permittivity, the electrode-Helmholtz plane distance upon bacterial binding and surface area coverage is not encountered. Using the electrodes as extended gates for MOSFETs, the sensor response is mostly due to the bacterial charge, thereby resulting in an LOQ improved by more than 2 orders of magnitude (Table 6.1). The use of a diluted measurement solution (PBS 1:100, having ionic strength equal to 1.62 mM, with a resulting Debye length of 76 Å) allowed us to maintain part of the bacterial layer within the charge screening region. In the case of molecular interactions at the gate of the transistor, such as negatively charged *Escherichia coli* (Silhavy *et al.*, 2010) captured by surface mannosides, the minimum V_{gs} required to bring the n-MOSFET in the *turn-on* state is increased and it can be measured as an evidence of the binding event. The negative charge of *Escherichia coli* (Silhavy *et al.*, 2010) produces a positive shift in the V_{gs} of n-type MOSFETs (Figure 6.11a). Figure 6.11b illustrated the values of ΔV_{gs} for different *Escherichia coli* PKL1162 concentrations. ΔV_{gs} increases from 31.0 ± 11.9 mV to 115.2 ± 12.9 mV when the bacterial concentration increases from 1.9×10^5 CFU/ml to 4.2×10^9 CFU/ml. The former value is still distinguishable from the signals obtained both in the presence of bacteria non-specific to the immobilised sugar (ΔV_{gs} = 8.7 ± 1.3 mV) and in the presence of a non-specific immobilised sugar (ΔV_{gs} = 16.2 ± 1.5 mV). MOSFET measurements have the additional advantage of being very fast: data can be recorded in less than a second.

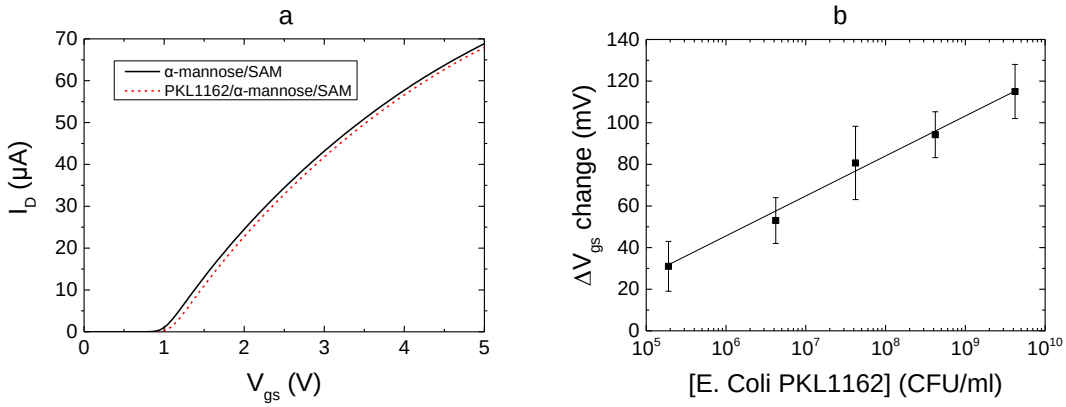

Figure 6.11 a) MOSFET I_D/V_{gs} characteristic for an electrode before (solid line) and after (dotted line) Escherichia coli PKL1162 binding. b) V_{gs} changes vs. bacterial concentration. The line represents only a visual guide for the eye.

6.9 MALDI-ToF measurements

Usual MALDI-ToF mass spectrometry (MS) is carried out on conducting gold supports (gold plates) rather than on non-conducting supports such as the glass slides when gold electrodes were evaporated as used here. As introduced in section 2.4.3, the conductive support guarantees the acceleration of the ionic cloud of ions produced by the UV beam light. Nonetheless, in order to perform both EIS, MOSFET and MS measurements keeping the same conditions, MALDI-ToF analysis was performed on evaporated gold by covering the back of the glass slide with silver paint or a strip of aluminium foil (Weissenborn *et al.*, 2012). This solution produced effective MALDI-ToF readings although the signal intensities were smaller. The measurements were then repeated also on gold plates by direct surface ionisation for confirming the glycan functionalisation of SAMs (Figure 6.12a) and the *Escherichia coli* PKL1162 binding on α-D-mannose (Figure 6.12b). Moreover, in order to compare the sensor responses, the spectra of MALDI-ToF performed on gold plates (exhibiting larger signals than those performed in glass supports) were used.

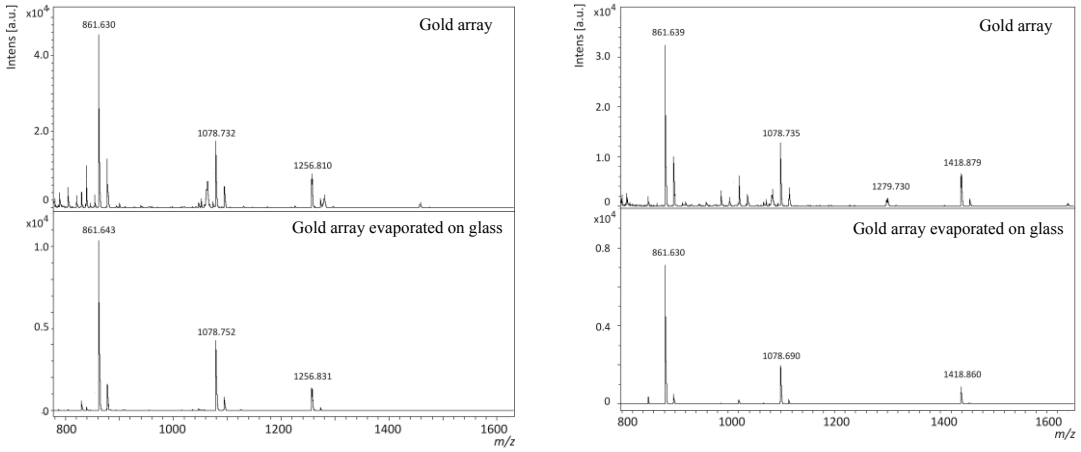

a b

Figure 6.12 Representative MALDI-ToF spectra of glycans covalently attached to SAMs on gold array and on evaporated gold array on glass slide; a) α-D-mannose (1256.829 m/z); b) 4-O-β-D-galactopyranosyl-D-glucopyranose (1418.86 m/z).

Specific peaks situated at 12000 and 16000 m/z corresponding to MS fingerprint of *Escherichia coli* PKL1162 can be observed by performing MS on bacterial sample spotted on bare gold without SAM functionalisation (Figure 6.13/Control). Such peaks were detected in the affinity reaction not only when performing the measurements on gold arrays but also on the gold arrays evaporated on glass as it can be seen in Figure 6.13.

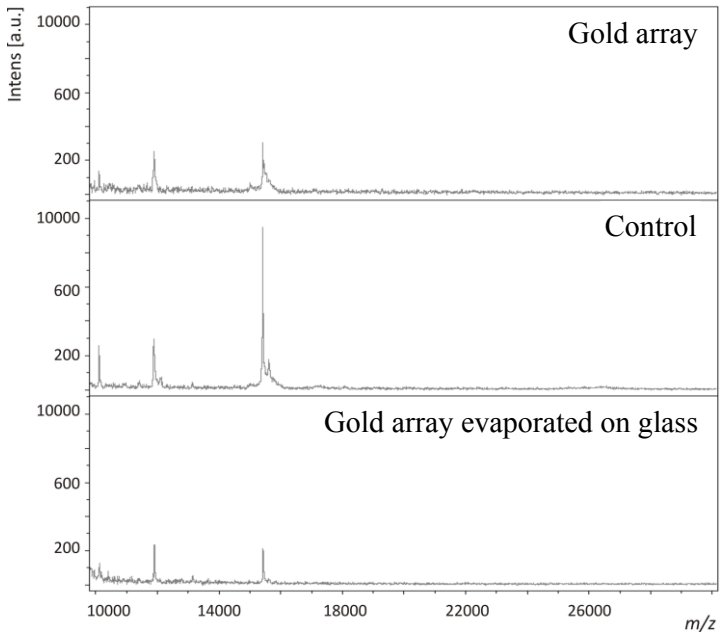

Figure 6.13 MALDI-ToF spectra of uropathogenic Escherichia coli PKL1162 after affinity capture on α-D-mannose covalently linked to gold electrodes evaporated on glass slides (top image), of Escherichia coli PKL1162 spotted on bare gold (middle plot) and Escherichia coli PKL1162 after affinity capture on α-D-mannose covalently linked to gold arrays (bottom image). The peaks at12000 and 16000 m/z are diagnostic for Escherichia coli PKL1162.

Moreover, the specificity of α-D-mannose towards *Escherichia coli* strain PKL1162 is shown in Figure 6.14: *Escherichia coli* PKL1162 peaks are only clearly visible after affinity capture and washing, when the gold electrodes are functionalised with α-D-mannose but not with other sugars.

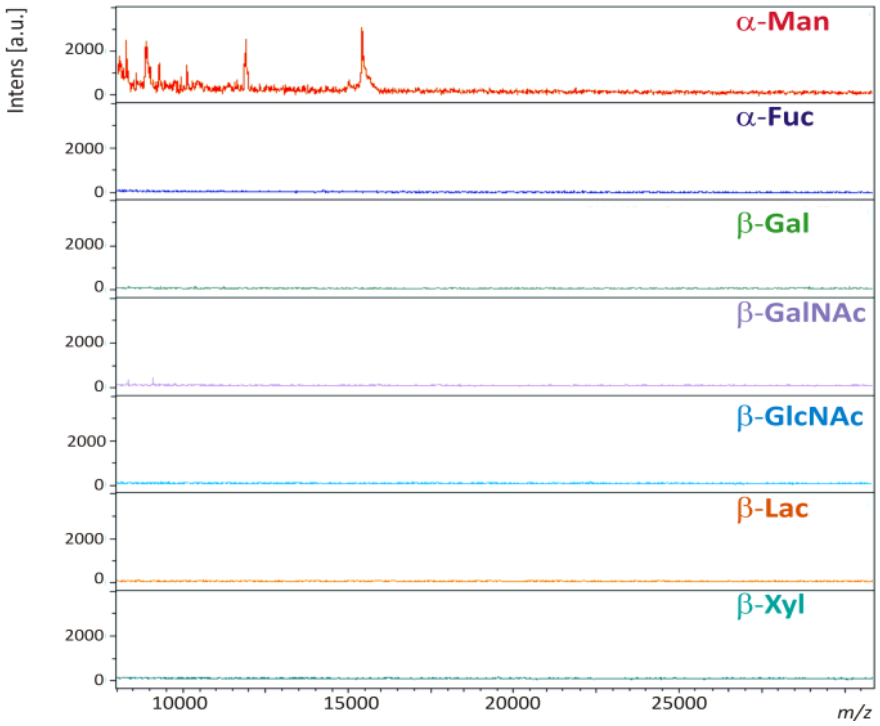

Figure 6.14 MALDI-ToF spectra of Escherichia coli PKL1162 affinity capture experiments on different glycan surfaces. Only the α-D-mannose-functionalised surface showed the characteristic peaks for PKL1162 at 12000 and 16000 m/z.

MALDI-ToF spectra also showed absence of any significant non-specific attachment of *Escherichia coli* K12 on α-D-mannose as well as on other sugars (Figure 6.15, bottom image).

Although SEM microscopy shows significant bacterial adhesion using samples of PKL1162 diluted up to 4.2×10^6 CFU/ml (Figure 6.10d), in terms of limit of quantitation by using MALDI-ToF a minimum concentration of 2.7×10^9 CFU/ml was required to produce observable peaks on gold plate (Figure 6.15).

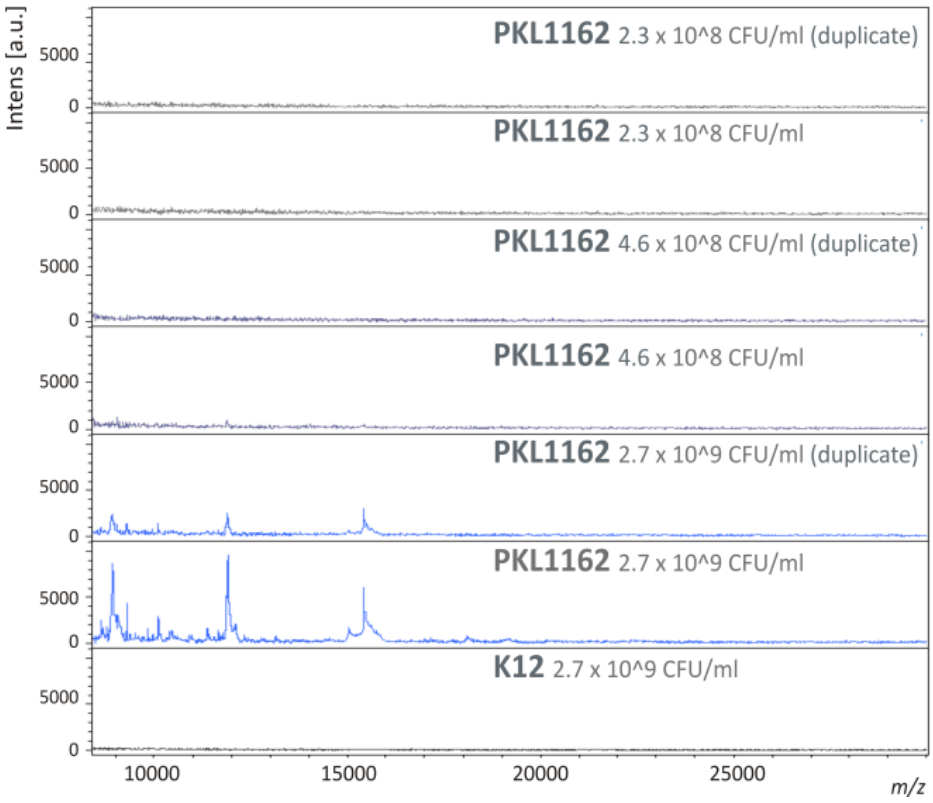

Figure 6.15 MALDI-ToF spectra of Escherichia coli PKL1162 affinity capture experiments on different glycan surfaces. b) MALDI-ToF spectra responses for different concentrations of Escherichia coli PKL1162 on α-D-mannose. The analysis was performed on SAM-functionalised gold plates, Escherichia coli K12 was used as negative control and showed no peaks upon MS analysis.

6.10 A preliminary study on a peptide-based capacitive sensor for prostate cancer cells detection

Preliminary data are here reported for the detection of a prostatic cancer cell line using a peptide as a recognition element in order to demonstrate that an approach similar to that used for bacteria detection can be successfully employed for other systems. The study has not been thoroughly optimised due to time constraints but promising positive results have been obtained performing capacitive measurements as it is shown in the next sections.

6.10.1 Bombesin peptide and the role in prostatic cancer cell lines

Bombesin (BBN) is a 14 amino-acid peptide whose receptors have been found overexpressed on the membrane of several cancer cell lines such as in those from lung,

pancreatic, breast and prostate tumours (Prasanphanich *et al.*, 2007). The amount of gastrin-releasing peptide (GRP) receptor expression, which recognize BBN, is correlated to the severity of the prostate cancer type (Markwalder and Reubi, 1999). One way to evaluate the malignancy of a cancer is based on its capability to reject the hormonal stimulus that are intended to repair the cells. Tumours that have this ability are called androgen receptor (AR) insensitive tumours and are characterised by having a worse prognosis with respect to the AR sensitive types. A characteristic of AR insensitive tumours is the high density of GRP receptor expression on their cellular surface.

The metastatic cancer cell line PC-3 derives from the prostatic small cell neuroendocrine carcinoma (SNCN) and is an example of AR insensitive tumour. It is therefore characterised by having high expression of GRP receptors which, in turn, provides a higher probability for BBN to bind to the cellular membrane. The high selectivity and affinity between BBN and GRP receptors encouraged researchers to exploit their strong interaction for radiolabelling techniques and chemotherapy. Indeed, labelled-BBN can be used for both imaging of prostate cancer cells (Prasanphanich *et al.*, 2007) and for therapy by targeting cancer cells with a better accuracy (Hoffman *et al.*, 2003). In addition, the affinity of BBN for the GRP receptors opens opportunities for detecting cancerous circulating cells in the blood (de Bono *et al.*, 2008; Allard *et al.*, 2004; Racila *et al.*, 1998).

To date the only electrochemical biosensor for PC-3 cells detection exploits an aptamer-based EIS method (Min *et al.*, 2010). In this work a reduced sequence of BBN (7-13) NH_2: Gln-Trp-Ala-Val-Gly-His-Leu-NH_2, having molecular weight equal to 809 Da has been used. This BBN analogue sequence has already been employed to design tumour-specific radiotracers for early diagnosis or systemic radiotherapy of the GRP-R positive tumours (Yang, 2004; Safavy *et al.*, 1997).

Combining the need to develop a label-free electrochemical system for PC-3 cells detection with the capability of the BBN-GRP receptor interaction, the basis for an EIS sensor for PC-3 cells detection have been studied. Since previous investigations based on BBN-GRP receptors interaction involved *in vitro* and *in vivo* experiments

performed in solution, no data were available for on-surface-based assays. The study here reported, however, was only partially optimised due to time and budged constraints.

6.10.2 Experimental set up

PC-3 cells have been grown in the Department of Pharmacy and Pharmacology of the University of Bath and BBN was purchased from EZBiolab (USA). Gold macroelectrodes were used for the measurements following the cleaning procedures explained in Chapter 3. For the SAM formation, an amine-terminated linker molecule, namely 11-amino-1-undecanethiol hydrochloride (AUT), was used instead of the usual carboxyl-terminated alkanethiols. This strategy allowed the immobilisation of the peptide in the orientation that guarantees the cellular recognition i.e. the carboxyl termination of the peptide (C-terminus) binds the SAM while the amine-side termination (N-terminus) is left free for the recognition of the cellular membrane (Figure 6.16).

Therefore, the electrodes were incubated overnight in a solution of AUT/MCH in a ratio 1:200 followed by a further 1 hour backfilling step using a solution of 1 mM MCH. In order to confer better antifouling properties to the SAM, poly(ethylene glycol) 2-aminoethyl ether acetic acid (amine-PEG-carboxylic acid) was also used as an intermediate compound between the formed structure and the BBN. An incubation step using a mixture of amine-PEG-carboxylic acid and sulfo-EDC elongated the SAM by *n*-chains of PEG molecules keeping the amine termination exposed for further immobilisation steps. By using this strategy the carboxylic acid of amine-PEG-carboxylic acid is involved in binding the amine termination of AUT whilst the final structure still presents a free amine termination for successive immobilisation steps. The inability to bind the cells when BBN was immobilised on the SAM in the opposite orientation (hence using a carboxyl-terminated SAM) was confirmed by EIS experiments that showed a signal change lower than 0.5 % for a concentration of 3×10^5 PC-3 cells/ml. Moreover, fluorescence studies previously reported in literature (Yang, 2004; Safavy *et al.*, 1997) also employed the Gln terminus of the peptide

(where the carboxyl group is exposed) for the fluorescent labelling and the Leu terminus for the cell recognition. A schematic of the binding principle of BBN on the SAM is shown in Figure 6.16.

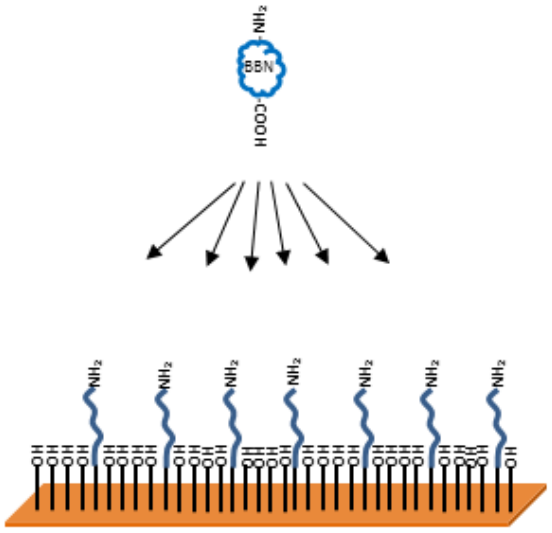

Figure 6.16 Schematic of the BBN binding principle. The amine-terminated SAM binds to the carboxyl-terminated side of the BBN leaving the amine termination of the peptide free for the GRP recognition.

On the other hand, by using sulfo-EDC chemistry for the PEG-ylation of the SAM, the exact amount of amine-PEG-carboxylic acid molecules that will bind, hence its length, cannot be controlled. In order to prevent an excessive PEG-ylation a short incubation time (10 minutes) was used, followed by stabilisation in measurement solution. An ideal condition consists in having a certain *n*-number of PEGs that ensure BBN to be internalised by the GRP receptors of the cells and, at the same time, ensure that the binding does not happen too far from the electrode surface.

The BBN immobilisation was successively performed incubating the electrodes with a mixture of 35 µM BBN and 80 mM sulfo-EDC in aqueous solution for 20 minutes. The electrodes were then rinsed and left in measurement solution for 1 hour before the first set of EIS measurements.

The cells used for the binding assay were suspended in PBS 0.1 mM with addition of 0.05 % of Tween20 that helped to reduce the non-specific interaction with the modified electrode surface.

6.10.3 Non-Faradaic EIS measurements for the detection of cells

For testing the affinity reaction, three cell lines were used: PC-3, LNCaP and FEK-4. The first two cell lines derive from bone metastasis of a prostate cancer but the metastatic potential of PC-3 cells is demonstrated to be higher than LNCaP (Pulukuri *et al.*, 2005). The PC-3 line is considered to be a later stage of prostate cancer (Dozmorov *et al.*, 2009) as well as more aggressive than LNCaP due to its AR insensitive nature (Lash *et al.*, 2015). As a result the GRP expression density on the cellular surface, as demonstrated in previous studies (Lee *et al.*, 2001) is much higher in PC-3 compared to LNCaP cells. In addition, a confirmation of the non-specific binding nature of LNCaP to BBN was demonstrated by a fluorescence study performed by Reile *et al.* (1994). Therefore, the use of PC-3 aimed to produce significant signal shift while LNCaP and FEK-4 cells (non-cancerous cells from normal human dermal fibroblasts tissues) were used as negative controls.

The EIS response was studied for concentration of cells between 30 and 3×10^5 cells/ml. Non-Faradaic EIS measurements were performed both in PBS 10 mM diluted 100 times (ionic strength equal to 1.62 mM) and 1000 times (ionic strength equal to 0.162 mM) to study the effect of the buffer. The signal response obtained for the PC-3 cell line is illustrated in Figure 6.17 and shows that the highest dilution of PBS results in an average higher signal change. On the other hand, using a more diluted measurement solution also increases the standard deviation, thus a lower reproducibility of the measurements. Taking into account the lower reproducibility and the probability of cell damage using a very dilutes measurement solution, for the reasons explained in section 6.5.1, a dilution of 100 times was chosen as best.

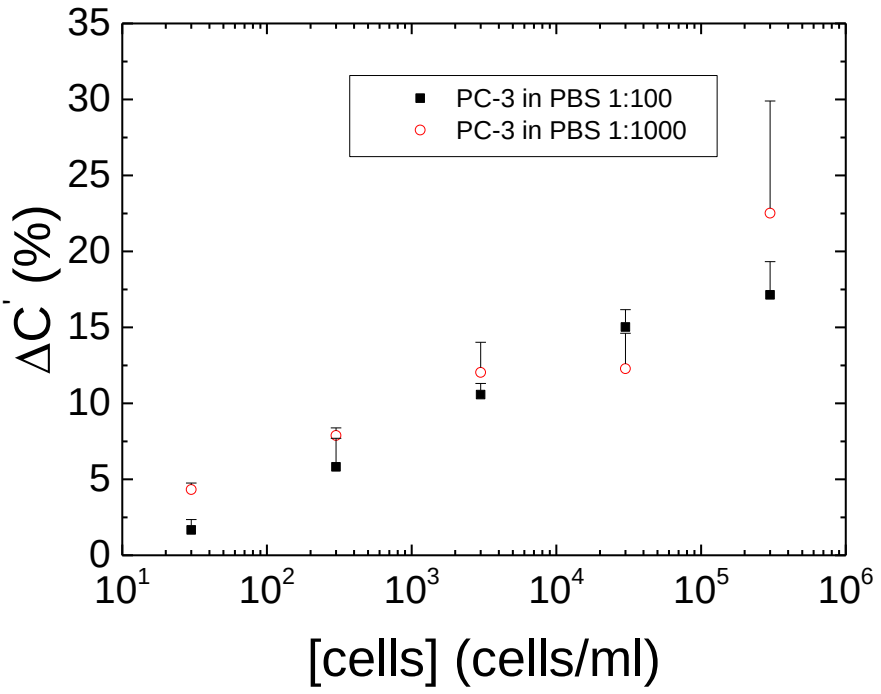

Figure 6.17 Comparison of the sensor response using PBS 10 mM diluted 100 times (ionic strength equal to 1.62 mM) and 1000 times (ionic strength equal to 0.162 mM) as a measurement solution. Standard deviations are only reported on one side for clarity.

As already showed for the bacteria detection, also the cells recognition produced a positive shift in capacitive measurements.

The dose response obtained for the three cell lines is shown in Figure 6.18. The inset of Figure 6.18 illustrates the capacitance response in the linear scale with a data fitting that follows with a good approximation the Hill equation. The R^2 values were 0.999, 0.990 and 0.963 while the K_d values were 1207, 11363 and 4271 cells/ml for PC-3, LNCaP and FEK-4, respectively.

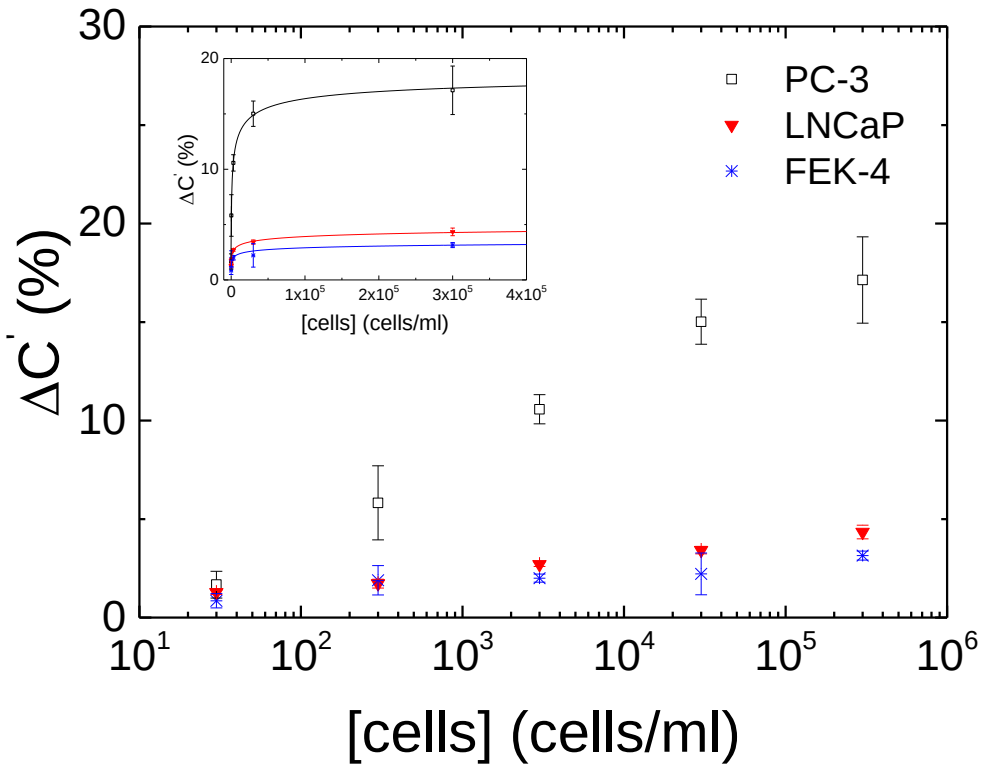

Figure 6.18 Dose response for PC-3, LNCaP and FEK-4 cell lines. In the inset the capacitance change is plotted vs. the linear scale of the concentration where the lines, which serve as guides to the eye, are fits of the data to a Hill dose response.

The sensor demonstrated the capability of discriminating cells having a high density of GRP receptors expressed on the cell membrane. A full characterisation and optimisation of the sensor is still required to ensure that the SAM formation is reproducible from experiment to experiment. In particular, the way the SAM is currently immobilised does not allow to know the exact amount of amine-PEG-carboxylic acid molecules binding onto AUT. Therefore, a further optimisation of the sensor, which includes the development of a strategy to control the reproducibility of the SAM formation, is needed.

6.11 Conclusions

By performing non-Faradaic EIS measurements a simple and inexpensive sensor could be set up for detecting uropathogenic bacteria on glycosylated surfaces exploiting the size and the charge of the analyte.

The binding of *Escherichia coli* PKL1162 as well as the negative control reactions were confirmed by SEM images on gold electrodes. The use of a long PEG-terminated SAM not only proved effective in gathering capacitive changes upon the affinity reaction but also helped in obtaining a reproducible EIS signal and successfully prevent the interactions with non-specific bacteria. Contrary to what was initially expected, the bacteria binding produced an increase in capacitance rather than a decrease. Nevertheless, these results were confirmed by performing the affinity assay with a parallel-plate capacitive sensor connected to an Agilent B1500A HR CMU Semiconductor Device Analyser. A possible model that describes the behaviour of the system has been given in terms of equivalent capacitances. Such a model can be applied to similar systems, especially where PEG-terminated SAMs are used.

Using gold evaporated electrodes on glass slides, measurements could be performed not only by means of EIS but also using MALDI-ToF and a MOSFET sensor. The electrodes were used as extended gate arrays for MOSFET measurements. The signals were then compared with EIS and MALDI-ToF MS exploiting the same surface immobilisation. The EIS measurements showed a better LOQ than a well established technique such as MALDI-TOF. However, the MOSFET sensor revealed to be even faster, more sensitive as well as being more inexpensive than EIS. The results showed MOSFET detection up to 1.9×10^5 CFU/ml *vs.* 4.2×10^7 and 2.7×10^9 CFU/ml obtained with EIS and MALDI-ToF, respectively. Moreover, MOSFET measurements are extremely fast (measurements last less than 2 seconds) and the mass production of such devices allows fabrication of inexpensive arrays of sensors. In Table 6.1 the time of measurements and the limit of quantitation (LOQ) of the MOSFET and EIS sensors are compared to MALDI-ToF.

Table 6.1 MOSFET, MALDI-ToF MS and EIS are compared in terms of LOQ and time for carrying out the measurements. The comparison is obtained considering that the three techniques employ the same electrodes. Therefore, immobilisation times of the electrodes as well as the bacterial growth are not considered as they are equal for all the assays here reported.

Technique	LOQ (CFU/ml)	Time required for the measurement
MOSFET	1.9×10^5	~ 2 s
MALDI-ToF MS	2.7×10^9	~ 20 min
EIS	4.2×10^7	~ 5 min

Such fabricated sensor can be used to support current clinical microbiology analysis by providing high-throughput screening of pathogenic bacterial samples. This technology can be easily implemented and performed after the enrichment step and before further advanced investigations so that additional time and costs can be saved in the traditional bacterial detection. Current limitations at this stage is the development of molecular probes to differentiate pathogens that can be used for multiplexed screening.

Finally, non-Faradaic EIS measurements also demonstrated to be successful for the detection of cancerous cells using a similar approach. Although a full characterisation and optimisation is needed for this system, promising results on the effectiveness of employing non-Faradaic processes have been confirmed.

References

Adiguzel, Y., & Kulah, H. (2012). CMOS cell sensors for point-of-care diagnostics. *Sensors*, 12(8), 10042-10066.

Ahmed, A., Rushworth, J. V., Hirst, N. A., & Millner, P. A. (2014). Biosensors for whole-cell bacterial detection. *Clinical Microbiology Reviews*, 27(3), 631-646.

Allard, W. J., Matera, J., Miller, M. C., Repollet, M., Connelly, M. C., Rao, C., Tibbe, A. G. J., Uhr, J. W., & Terstappen, L. W. (2004). Tumor cells circulate in the peripheral blood of all major carcinomas but not in healthy subjects or patients with nonmalignant diseases. *Clinical Cancer Research*, 10(20), 6897-6904.

Asami, K., Hanai, T., & Koizumi, N. (1980). Dielectric analysis of Escherichia coli suspensions in the light of the theory of interfacial polarisation. *Biophysical Journal*, 31(2), 215.

Berggren, C., Bjarnason, B., & Johansson, G. (2001). Capacitive biosensors. *Electroanalysis*, 13(3), 173-180.

Both, P., Green, A. P., Gray, C. J., Šardzík, R., Voglmeir, J., Fontana, C., Austeri, M., Rejzek, M., Richardson, D., Field, R. A., Widmalm, G., Flitsch, S. L., & Eyers, C. E. (2014). Discrimination of epimeric glycans and glycopeptides using IM-MS and its potential for carbohydrate sequencing. *Nature Chemistry*, 6(1), 65-74.

Braiek, M., Rokbani, K. B., Chrouda, A., Mrabet, B., Bakhrouf, A., Maaref, A., & Jaffrezic-Renault, N. (2012). An electrochemical immunosensor for detection of Staphylococcus aureus bacteria based on immobilisation of antibodies on self-assembled monolayers-functionalized gold electrode. *Biosensors*, 2(4), 417-426.

Brachman, P. S., & Abrutyn, E. (Eds.). (2009). *Bacterial Infections of Humans: Epidemiology and Contro*l. Springer Science+ Business Media, 95-107

Braga, P. A. C., Tata, A., dos Santos, V. G., Barreiro, J. R., Schwab, N. V., dos Santos, M. V., Barreiro, J. R., Schwab, V., dos Santos, M. V., Erbelina, M. N., & Ferreira, C. R. (2013). Bacterial identification: from the agar plate to the mass spectrometer. *RSC Advances*, 3(4), 994-1008.

Carrara, S., Bhalla, V., Stagni, C., Benini, L., Ferretti, A., Valle, F., Gallotta, A., Riccò, B. & Samorì, B. (2009). Label-free cancer markers detection by capacitance biochip. *Sensors and Actuators B: Chemical*, 136(1), 163-172.

Coates, A., Hu, Y., Bax, R., & Page, C. (2002). The future challenges facing the development of new antimicrobial drugs. *Nature Reviews Drug Discovery*, 1(11), 895-910.

Couniot, N., Vanzieleghem, T., Rasson, J., Van Overstraeten-Schlögel, N., Poncelet, O., Mahillon, J., Francis, L. A., & Flandre, D. (2015a). Lytic enzymes as selectivity means for label-free, microfluidic and impedimetric detection of whole-cell bacteria using ALD-Al_2O_3 passivated microelectrodes. *Biosensors and Bioelectronics*, 67, 154-161.

Couniot, N., Afzalian, A., Van Overstraeten-Schlögel, N., Francis, L. A., & Flandre, D. (2015b). Capacitive biosensing of bacterial cells: Analytical model and numerical simulations. *Sensors and Actuators B: Chemical*, 211, 428-438.

Couniot, N., Francis, L. A., & Flandre, D. (2015c). A 16 ×16 CMOS capacitive biosensor array towards detection of single bacterial cell. *IEEE Transactions on Biomedical Circuits and Systems*, 99, 1-11.

de Bono, J. S., Scher, H. I., Montgomery, R. B., Parker, C., Miller, M. C., Tissing, H., Doyle, G. V., Terstappen, L. W. W. M., Pienta, K. J., & Raghavan, D. (2008). Circulating tumor cells predict survival benefit from treatment in metastatic castration-resistant prostate cancer. *Clinical Cancer Research*, 14(19), 6302-6309.

Didelot, X., Bowden, R., Wilson, D. J., Peto, T. E., & Crook, D. W. (2012). Transforming clinical microbiology with bacterial genome sequencing. *Nature Reviews Genetics*, 13(9), 601-612.

Dozmorov, M. G., Hurst, R. E., Culkin, D. J., Kropp, B. P., Frank, M. B., Osban, J., Penning, T. M., & Lin, H. K. (2009). Unique patterns of molecular profiling between human prostate cancer LNCaP and PC-3 cells. *The Prostate*, 69(10), 1077.

Fournier, P. E., Dubourg, G., & Raoult, D. (2014). Clinical detection and characterisation of bacterial pathogens in the genomics era. *Genome Medicine*, 6(11), 114.

Ghafar-Zadeh, E., Sawan, M., & Therriault, D. (2009). CMOS based capacitive sensor laboratory-on-chip: a multidisciplinary approach. *Analog Integrated Circuits and Signal Processing*, *59*(1), 1-12.

Haandbæk, N., Bürgel, S. C., Heer, F., & Hierlemann, A. (2014). Resonance-enhanced microfluidic impedance cytometer for detection of single bacteria. *Lab on a Chip*, 14(17), 3313-3324.

Hammond, J. L., Gross, A. J., Estrela, P., Iniesta, J., Green, S. J., Winlove, C. P., Winyard, P. G., Benjamin, N., & Marken, F. (2014). Cysteine-cystine redox cycling in a gold–gold dual-plate generator-collector microtrench sensor. *Analytical Chemistry*, 86(14), 6748-6752.

Hartmann, M., & Lindhorst, T. K. (2011). The bacterial lectin FimH, a target for drug discovery–carbohydrate inhibitors of type 1 fimbriae-mediated bacterial adhesion. *European Journal of Organic Chemistry*, 2011(20-21), 3583-3609.

Hartmann, M., Horst, A. K., Klemm, P., & Lindhorst, T. K. (2010). A kit for the investigation of live Escherichia coli cell adhesion to glycosylated surfaces. *Chemical Communications*, 46(2), 330-332.

Hoffman, T. J., Gali, H., Smith, C. J., Sieckman, G. L., Hayes, D. L., Owen, N. K., & Volkert, W. A. (2003). Novel series of 111In-labeled bombesin analogs as potential radiopharmaceuticals for specific targeting of gastrin-releasing peptide receptors expressed on human prostate cancer cells. *Journal of Nuclear Medicine*, 44(5), 823-831.

Hrabák, J., Chudáčková, E., & Walková, R. (2013). Matrix-assisted laser desorption ionisation–time of flight (MALDI-TOF) mass spectrometry for detection of antibiotic resistance mechanisms: from research to routine diagnosis. *Clinical Microbiology Reviews*, 26(1), 103-114.

Kang, D. K., Ali, M. M., Zhang, K., Huang, S. S., Peterson, E., Digman, M. A., Gratton, E., & Zhao, W. (2014). Rapid detection of single bacteria in unprocessed blood using integrated comprehensive droplet digital detection. *Nature Communications*, 5, 5427.

Lash, L., Putt, D., & Jankovich, A. (2014). Glutathione levels and susceptibility to chemically induced injury in human prostate cancer cell lines. *The FASEB Journal*, 28(1), 663.11.

Lee, L. F., Guan, J., Qiu, Y., & Kung, H. J. (2001). Neuropeptide-induced androgen independence in prostate cancer cells: roles of nonreceptor tyrosine kinases Etk/Bmx, Src, and focal adhesion kinase. *Molecular and Cellular Biology*, 21(24), 8385-8397.

Li, M., Li, W. H., Zhang, J., Alici, G., & Wen, W. (2014). A review of microfabrication techniques and dielectrophoretic microdevices for particle manipulation and separation. *Journal of Physics D: Applied Physics*, *47*(6), 1-29.

Li, D., Feng, Y., Zhou, L., Ye, Z., Wang, J., Ying, Y., Ruan, C., Wang, R, & Li, Y. (2011). Label-free capacitive immunosensor based on quartz crystal Au electrode for rapid and sensitive detection of Escherichia coli O157: H7. *Analytica Chimica Acta*, 687(1), 89-96.

Lodish, H., Berk, A., Zipursky, S. L., Matsudaira, P., Baltimore, D., & Darnell, J. (2000). Protein glycosylation in the ER and Golgi complex. *Molecular Cell Biology. 4th edition*, 711-722.

Ma, F., Rehman, A., Liu, H., Zhang, J., Zhu, S., & Zeng, X. (2015). Glycosylation of quinone-fused polythiophene for reagentless and label-free detection of E. coli. *Analytical Chemistry*, 87(3), 1560-1568.

Mannoor, M. S., Tao, H., Clayton, J. D., Sengupta, A., Kaplan, D. L., Naik, R. R., Verma, N., Omenetto, F. G., & McAlpine, M. C. (2012). Graphene-based wireless bacteria detection on tooth enamel. *Nature Communications*, 3, 763.

Markwalder, R., & Reubi, J. C. (1999). Gastrin-releasing peptide receptors in the human prostate relation to neoplastic transformation. *Cancer Research*, 59(5), 1152-1159.

Min, K., Song, K. M., Cho, M., Chun, Y. S., Shim, Y. B., Ku, J. K., & Ban, C. (2010). Simultaneous electrochemical detection of both PSMA (+) and PSMA (−) prostate cancer cells using an RNA/peptide dual-aptamer probe. *Chemical Communications*, 46(30), 5566-5568.

Mohanty, N., & Berry, V. (2008). Graphene-based single-bacterium resolution biodevice and DNA transistor: interfacing graphene derivatives with nanoscale and microscale biocomponents. *Nano Letters*, 8(12), 4469-4476.

Nicolaou, N., Xu, Y., & Goodacre, R. (2012). Detection and quantification of bacterial spoilage in milk and pork meat using MALDI-TOF-MS and multivariate analysis. *Analytical Chemistry*, 84(14), 5951-5958.

Noble, G. T., Craven, F. L., Voglmeir, J., Šardzík, R., Flitsch, S. L., & Webb, S. J. (2012). Accelerated enzymatic galactosylation of N-acetylglucosaminolipids in lipid microdomains. *Journal of the American Chemical Society*, 134(31), 13010-13017.

Oelschlaeger, T. A., Dobrindt, U., & Hacker, J. (2002). Virulence factors of uropathogens. *Current Opinion in Urology*, 12(1), 33-38.

Ostuni, E., Yan, L., & Whitesides, G. M. (1999). The interaction of proteins and cells with self-assembled monolayers of alkanethiolates on gold and silver. *Colloids and Surfaces B*, 15(1), 3-30.

Peterson, B. W., Sharma, P. K., van der Mei, H. C., & Busscher, H. J. (2012). Bacterial cell surface damage due to centrifugal compaction. *Applied and Environmental Microbiology*, 78(1), 120-125.

Prakash, S. B., & Abshire, P. (2008). Tracking cancer cell proliferation on a CMOS capacitance sensor chip. *Biosensors and Bioelectronics*, 23(10), 1449-1457.

Prasanphanich, A. F., Nanda, P. K., Rold, T. L., Ma, L., Lewis, M. R., Garrison, J. C., Hoffman, T. J., Sieckman, G. L., Figueroa, S. D., & Smith, C. J. (2007). [64Cu-

NOTA-8-Aoc-BBN (7-14) NH2] targeting vector for positron-emission tomography imaging of gastrin-releasing peptide receptor-expressing tissues. *Proceedings of the National Academy of Sciences*, 104(30), 12462-12467.

Pulukuri, S. M., Gondi, C. S., Lakka, S. S., Jutla, A., Estes, N., Gujrati, M., & Rao, J. S. (2005). RNA interference-directed knockdown of urokinase plasminogen activator and urokinase plasminogen activator receptor inhibits prostate cancer cell invasion, survival, and tumorigenicity in vivo. *Journal of Biological Chemistry*, 280(43), 36529-36540.

Qian, C., Huang, H., Chen, L., Li, X., Ge, Z., Chen, T., Yang, Z., & Sun, L. (2014). Dielectrophoresis for bioparticle manipulation. *International journal of molecular sciences*, *15*(10), 18281-18309.

Racila, E., Euhus, D., Weiss, A. J., Rao, C., McConnell, J., Terstappen, L. W., & Uhr, J. W. (1998). Detection and characterisation of carcinoma cells in the blood. *Proceedings of the National Academy of Sciences*, 95(8), 4589-4594.

Reile, H., Armatis, P. E., & Schally, A. V. (1994). Characterisation of high-affinity receptors for bombesin/gastrin releasing peptide on the human prostate cancer cell lines PC-3 and DU-145: internalisation of receptor bound 125I-(Tyr4) bombesin by tumor cells. *The Prostate*, 25(1), 29-38.

Reisner, A., Haagensen, J. A., Schembri, M. A., Zechner, E. L., & Molin, S. (2003). Development and maturation of Escherichia coli K-12 biofilms. *Molecular Microbiology*, 48(4), 933-946.

Safavy, A., Khazaeli, M. B., Qin, H., & Buchsbaum, D. J. (1997). Synthesis of bombesin analogues for radiolabeling with rhenium-188. *Cancer*, 80(S12), 2354-2359.

Šardzík, R., Green, A. P., Laurent, N., Both, P., Fontana, C., Voglmeir, J., Weissenborn, M. J., Haddoub, R., Grassi, P., Haslam, S. M., Widmalm, G., & Flitsch, S. L. (2012). Chemoenzymatic synthesis of O-mannosylpeptides in solution and on solid phase. *Journal of the American Chemical Society*, 134(10), 4521-4524.

Šardzík, R., Sharma, R., Kaloo, S., Voglmeir, J., Crocker, P. R., & Flitsch, S. L. (2011). Chemoenzymatic synthesis of sialooligosaccharides on arrays for studies of cell surface adhesion. *Chemical Communications*, 47(19), 5425-5427.

Silhavy, T. J., Kahne, D., & Walker, S. (2010). The bacterial cell envelope. *Cold Spring Harbor Perspectives in Biology*, 2(5), a000414.

Stein, R. A. (2011). Super-spreaders in infectious diseases. *International Journal of Infectious Diseases*, 15(8), e510-e513.

Tsouti, V., Boutopoulos, C., Zergioti, I., & Chatzandroulis, S. (2011). Capacitive microsystems for biological sensing. *Biosensors and Bioelectronics*, 27(1), 1-11.

Varshney, M., & Li, Y. (2008). Double interdigitated array microelectrode-based impedance biosensor for detection of viable Escherichia coli O157: H7 in growth medium. *Talanta*, 74(4), 518-525.

Varshney, M., Li, Y., Srinivasan, B., & Tung, S. (2007). A label-free, microfluidics and interdigitated array microelectrode-based impedance biosensor in combination with nanoparticles immunoseparation for detection of Escherichia coli O157: H7 in food samples. *Sensors and Actuators B: Chemical*, 128(1), 99-107.

Wang, L., Lu, J., Marchenko, S. A., Monuki, E. S., Flanagan, L. A., & Lee, A. P. (2009). Dual frequency dielectrophoresis with interdigitated sidewall electrodes for microfluidic flow-through separation of beads and cells. *Electrophoresis*, *30*(5), 782-791.

Webster, M. S., Timoshkin, I. V., MacGregor, S. J., & Mattey, M. (2009). Computer aided modelling of an interdigitated microelectrode array impedance biosensor for the detection of bacteria. *IEEE Transactions on Dielectrics and Electrical Insulation*, 16(5), 1356-1363.

Weissenborn, M. J., Wehner, J. W., Gray, C. J., Šardzík, R., Eyers, C. E., Lindhorst, T. K., & Flitsch, S. L. (2012). Formation of carbohydrate-functionalised polystyrene and glass slides and their analysis by MALDI-TOF MS. *Beilstein Journal of Organic Chemistry*, 8(1), 753-762.

World Health Organisation. (2003). *Assessing Microbial Safety of Drinking Water Improving Approaches and Methods: Improving Approaches and Methods*. OECD Publishing.

Yang, D. J. (2004). Handbook of radiopharmaceuticals: radiochemistry and applications. *Journal of Nuclear Medicine*, 45(6), 1096-1097.

Yang, L., & Bashir, R. (2008). Electrical/electrochemical impedance for rapid detection of foodborne pathogenic bacteria. *Biotechnology Advances*, 26(2), 135-150.

Zhi, Z. L., Laurent, N., Powell, A. K., Karamanska, R., Fais, M., Voglmeir, J., Wright, A., Blackburn, J. M., Crocker, P. R., Russell, D. A., Flitsch, S., Fiels, R. A., & Turnbull, J. E. (2008). A versatile gold surface approach for fabrication and interrogation of glycoarrays. *ChemBioChem*, 9(10), 1568-1575.

Zourob, M., Elwary, S., & Turner, A. P. (2008). *Principles of Bacterial Detection: Biosensors, Recognition Receptors and Microsystems: Biosensors, Recognition Receptors, and Microsystems*. Springer Science & Business Media.

Chapter 7. Conclusions

Impedimetric sensors represent a modern, fascinating and challenging venue for the development of new biosensors. Features such as the possibility of implementing label-free assays using a relatively inexpensive equipment make EIS one of the most promising electrochemical techniques for future point-of-care low-cost devices. However, the process of commercialisation of such sensors is still in an early stage and further developments are required. With the aim of improving the knowledge in the field of EIS-based sensors, in this dissertation several systems of diagnostic interest have been analysed in order to both provide deeper insights and highlight some conditions that could be exploited for developing EIS sensors. Since the strategies to adopt can vary considerably according to the target to be detected, three types of system were taken into consideration. These consisted of: a DNA aptamer-based for PSA detection, a multimodal platform for protein phosphorylation detection and a glycan-based biosensor for uropathogenic bacterial detection.

In Faradaic experiments for instance, features such as the probe coverage density as well as the combined effect of the target charge and obstructing effect are important factors to be optimised, especially in oligonucleotide-based sensors. The fine balance between these factors have been studied in the context of optimising an aptamer-based EIS sensor for PSA detection. Interestingly, it was found that a maximum analyte binding does not always correspond to a maximum EIS signal change. The mass

response from QCM-D measurements indicated that the DNA aptamer/MCH ratio at which the maximum analyte binding could be obtained was 1:200. However, a different ratio such as 1:100 resulted in a maximum R_{ct} signal change in Faradaic EIS measurements. Such a discrepancy is due to the opposing effect that the mass loading and the screening of the aptamer charge have on the EIS signals. It is true that between those two ratios, the least dense surface probe coverage (1:200) ensures a higher binding efficiency, nevertheless, the effect on the R_{ct} was found to be more reproducible and significant using a higher dense probe coverage (1:100). Moreover, a negative R_{ct} signal change was recorded upon the target binding indicating that the prevalent effect on the EIS signal is mostly due to the screening of the aptamer charge by bound PSA and not by the load of mass obstructing the redox probes. Therefore, the optimisation of the EIS sensor must be done compromising the surface conditions that provide the maximum target binding, i.e. using a ratio of 1:100 of DNA aptamer to MCH fraction.

To the best of the author's knowledge, this represents an important finding not explored by other researchers before and hence, that should be taken in consideration for the development of future oligonucleotide-based sensors. It can also be concluded that although aptamers have great potential towards the development of biosensors, aptasensors require a careful design in order to provide an acceptable binding efficiency. In the last decade, a big effort has been put into developing aptasensors, however, antibody-based sensors have not yet been replaced by newer technologies in real applications.

In the second system, EIS signals were aided by ferrocene-modified gold nanoparticles to greatly improve the sensitivity and specificity of the assay. An EIS study was therefore performed for detecting phosphorylation of protein, which is an important post-translational modification mechanism involved in many diseases if it is found to be altered. The effect of the mass and charge change upon phosphorylation yields weak signals in EIS. However, EIS signals can be enhanced by engineering of the surface biorecognition layer with the addition of signal probes. By using signal probes,

an indirect labelling strategy was implemented. In particular, this approach is based on the transition from non-Faradaic to Faradaic processes using ferrocene-modified gold nanoparticles that allows the generation of Faradaic current in a system that originally lacked redox molecules. The addition of signal probes allows the protein phosphorylation to be detected in a multimodal manner by means of supporting techniques such as LSPR and DPV. This is an important achievement that guarantees an improvement in determining false positives as well as an increase in the test confidence. The biosensor developed for the protein phosphorylation detection can be successfully used for screening inhibitors of kinases in a multiplexed way, which means that the system can be implemented for discovering new drugs in several pharmaceutical fields. This approach can be used to potentially assay activity of any kinase-protein pair in the presence of known/unknown inhibitors.

This strategy, which can still be classified as label-free, enabled an amplification of the signal for the detection of small and scattered phosphate groups that could not be achieved performing conventional EIS. As a support to the choice of adopting signal probes, it must be considered that the field of application in which the protein phosphorylation detection is performed, is the development of new drugs. Moreover, the discovery of new kinase inhibitors is one of the most studied investigation fields for developing cancer treatments. At the same time, only few kinases have been introduced on the market so far due to both the limitations in the biology advances and in the technologies in support of it. Therefore, the discovery of new drugs: firstly does not require the development of point-of-care devices but is limited to dedicated laboratory venues; secondly, it could generate enormous benefits where the cost of the sensing technique would be meaningless in comparison to the advantages (both in terms of patient's life-improvement and pharmaceutical companies profit) and the cost of the sensor does not represent the most important aspect to be optimised. The use of a multimodal approach that exploits signal probes is therefore justified.

In the last EIS case reported in this dissertation, a sensor for uropathogenic *Escherichia coli* was developed. Here, because of the size and charge of the analyte to

detect, a strategy based on non-Faradaic measurements was preferred. Indeed, non-Faradaic processes rely on the changes of the electrochemical double layer upon the molecular detection, which induces the redistribution of the solvent molecules and of the ions at the electrode interface. Although non-Faradaic processes are the least exploited in EIS sensors, probably because they are believed to be more complicated for the extraction of the signals of interest, they introduce a further simplicity to the assay because redox markers are not needed. Also in this system, a multimodal detection (which was also used to compare the sensors' performances) was demonstrated by validating the EIS signals with MALDI-ToF, SEM and MOSFET techniques. It was showed that non-Faradaic EIS detection of bacteria could be achieved by exploiting a long PEG-terminated SAM, which exhibits both antifouling properties and guarantees the formation of an insulating layer for reproducible EIS signals. In terms of results, EIS experiments provided a better sensitivity (two orders of magnitude) when the signals were compared with a more expensive and known technique such as MALDI-ToF. This revealed interesting premises for building a cheap and robust alternative to the current routine clinical microbiology. Additional interesting results came from the implementation of MOSFET readings on the same glycosylated electrode surfaces. The MOSFET set up also demonstrated a fast and sensitive detection of bacteria by measuring the cells charge. These features offer a tremendous potential for EIS and MOSFET sensors to support the current clinical microbiology analysis. Indeed, EIS and MOSFET measurements have been demonstrated to be performed on arrays of gold electrodes for providing high-throughput screening of pathogenic bacterial samples. By performing initial screenings of pathogenic samples, they can support in an inexpensive manner the decisional process of whether or not performing more complicated and longer analysis as it is currently required by the standard microbial diagnosis practice. Current limitations at this stage is represented by the development of molecular probes to differentiate pathogens that can be used for multiplexed screening.

As a preliminary study, detection of PC-3 cells was also demonstrated by performing non-Faradaic EIS measurements. Also in this application, a small probe (a 7 amino acid peptide) was used as a biological element to recognise a significant bigger

analyte. In both the bacteria and cells investigation, a positive increase in the capacitive signal was observed. This is explained as due to the formation of a well-packed and insulating SAM having hydrophilic properties. The binding of the analyte does not produce a complete displacement of solvent molecules, which can be modelled as an increase in the distance *d* between the plates of the equivalent capacitor but, conversely, adds a surface contribution that increases the capacitance value, as explained in Chapter 6.

Although a model for explaining the increase in the capacitance value was given with respect to the system object of study in this dissertation, it is worth noting that a more accurate and general study for obtaining a deeper insight into the correlation between the molecular phenomena and the EIS signal changes remains unaccomplished. Unfortunately, this represents the trend that can be observed in the majority of the published works where the authors' explanation of the impedance signals is confined to the single system object of study each time. On the other hand, it would be interesting and much useful, indeed, to find the correlation between the physico-chemical changes happening upon the analyte binding and the impedance signals in a much broader context. Although such an investigation could not be performed in the course of this dissertation because of time limitations, it would lead to a more efficient fabrication and optimisation of any EIS sensors since the mechanism to exploit would be known.

In conclusion, several EIS systems were analysed and successful practical applications have been demonstrated. By applying the optimisation and the strategies reported in this dissertation, effective and low-cost EIS-based sensors could be implemented and integrated in multimodal systems. These studies not only confirm the enormous potential of EIS as a label-free biosensing technique but also aim to be used for the optimisation of a wide range of EIS biosensors that exploit target/probe characteristics or surface modifications similar to those of the systems here reported.